Nano-Scale Scratching in Chemical-Mechanical Polishing

by

Thor Eusner

S.B., Mechanical Engineering
Massachusetts Institute of Technology, 2006

Submitted to the Department of Mechanical Engineering
in Partial Fulfillment of the Requirements for the Degree of

MASTER OF SCIENCE IN MECHANICAL ENGINEERING

at the

MASSACHUSETTS INSTITUTE OF TECHNOLOGY

February 2008

© 2008 Thor Eusner. All Rights Reserved.
The author hereby grants to MIT permission to reproduce
and to distribute publicly paper and electronic
copies of this thesis document in whole or in part
in any medium now known or hereafter created.

Signature of Author: ______________________
Department of Mechanical Engineering
December 19, 2007

Certified by: ______________________
Jung-Hoon Chun
Professor of Mechanical Engineering
Thesis Supervisor

Certified by: ______________________
Nannaji Saka
Research Affiliate, Department of Mechanical Engineering
Thesis Supervisor

Certified by: ______________________
Lallit Anand
Professor of Mechanical Engineering
Chairman, Department Committee on Graduate Students

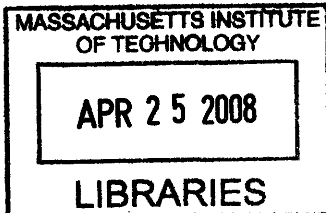

ARCHIVES

Nano-Scale Scratching in
Chemical-Mechanical Polishing

by

Thor Eusner

Submitted to the Department of Mechanical Engineering
on December 19, 2007 in partial fulfillment of the requirements for the Degree of
Master of Science in Mechanical Engineering

ABSTRACT

During the chemical-mechanical polishing (CMP) process, a critical step in the manufacture of ultra-large-scale integrated (ULSI) semiconductor devices, undesirable nano-scale scratches are formed on the surfaces being polished. As the width of the interconnect Cu lines continues to shrink to below 60 nm, and as the traditional SiO_2 dielectric is replaced by the compliant, low-dielectric-constant materials, scratching has emerged as a challenging problem.

This thesis presents a contact mechanics based approach for modeling nano-scale scratching by the hard abrasive particles in the slurry. Single-particle models that use elastic and plastic analyses to determine both the lower- and upper-bounds for the load per particle are introduced. These bounds are established for both homogenous and composite coatings. Multi-particle models are also presented. These models use contact mechanics at the pad-particle-coating interface to relate the global parameters of CMP, such as pressure, particle radius, slurry volume fraction and the material and geometrical properties of the pad and coating, to the widths and depths of scratches in the coatings. A lower- and upper-limit for the scratch width and depth in CMP is defined. Controlled indentation and scratching experiments have been conducted using a Hysitron TriboIndenter to validate the single-particle models. Based on these experiments, the upper-bound load per particle is used to predict the widths and depths of scratches in coatings. Furthermore, polishing experiments have been conducted using a CMP tool to validate the limits. The upper-limit for the semi-width of a scratch is equal to the product of the particle radius and the square root of the ratio of pad hardness to coating hardness. For a typical CMP pad and Cu coating, this upper-limit is one-fifth of the particle radius. Based on the models and the experiments, practical solutions for mitigating scratching in CMP, especially Cu CMP, are suggested.

Thesis Supervisor: Dr. Jung-Hoon Chun
Title: Professor of Mechanical Engineering

Thesis Supervisor: Dr. Nannaji Saka
Title: Research Affiliate, Department of Mechanical Engineering

Acknowledgments

There are a number of people who have helped, supported and guided me throughout my time at MIT. I would like to thank each of them for their continued support.

First, I would like to thank Professor Jung-Hoon Chun, my advisor, for his help, advice, suggestions and guidance during the past three years. Whenever I have needed anything in my academic or personal life, he has always been there to assist me and make my life easier. His methodologies for tackling problems, acquiring the resources necessary for the project to succeed and communicating with sponsors are the skills that I will carry with me for the rest of my professional life.

Second, I wish to thank Dr. Nannaji Saka, my advisor, for all of his time and dedication in helping me become a better thinker. He has spent a vast amount of energy and detailed thought on my research, for which I am very grateful. My time spent in lab with him discussing problems and issues have surely made me a better scholar. In addition, my time spent with him away from the project in social settings has made my time at MIT all the more enjoyable.

I would also like to thank my friend and lab mate Catherine Mau. She has always been there to help me with last minute problems that have occurred in my research and in my personal life. I also wish to thank all of the people who currently sit in room 35-135, the LMP Graduate Student Office. During my time in graduate school, I have developed many strong friendships that I know will last for many years.

I would also like to thank the LMP machine shop staff who have helped me build and machine various parts over the years: Gerald Wentworth, David Dow and Patrick McAtamney. I would also like to thank Dr. Alan Schwartzman in the NanoLab for helping me run experiments on the Hysitron TriboIndenter, Libby Shaw in the Center for Materials Science and Engineering for helping me use the AFM, and Patrick Boisvert and Dr. Yong Zhang in the Center for Materials Science and Engineering for helping me use the SEM.

I would like to thank the National Science Foundation (NSF) Graduate Research Fellowship Program for providing financial support for me to conduct this research and obtain my Master of Science degree. I would also like to thank the Semiconductor Research Corporation (SRC) for partially funding my research, specifically the Intel Corporation's custom-funding program. I would like to thank Dr. Paul Fischer of Intel Corporation for providing materials for my research and valuable industrial advice.

I wish to thank my best friends and roommates, Ben Cownie and Chris Ruggiero.

Finally, I thank my parents and my grandparents who have always believed in me and made my time at MIT possible. For my entire life, they have always sacrificed to make every opportunity available to me and for that I will be eternally grateful.

Table of Contents

Title Page 1
Abstract 2
Acknowledgments 3
Table of Contents 4
List of Figures 6
List of Tables 10

CHAPTER 1 INTRODUCTION **11**
1.1 Background 11
1.2 Copper/Low-k Dielectric Interconnects and CMP 15
1.3 Thesis Organization 19
Nomenclature 22

CHAPTER 2 SINGLE-PARTICLE CONTACT MECHANICS **23**
2.1 Introduction 23
2.2 Elastic Contact of Two Smooth Spheres 23
2.3 Elastic Analysis of a Homogenous Coating 25
2.4 Fully-Plastic Analysis of a Homogenous Coating 31
2.5 Elastic Analysis of a Composite Coating 34
2.6 Fully-Plastic Analysis of a Composite Coating 37
2.7 Coefficient of Friction 39
2.8 Preston Constant 41
2.9 Summary 43
Nomenclature 44

CHAPTER 3 MULTI-PARTICLE CONTACT MECHANICS **46**
3.1 Introduction 46
3.2 Particle Spacing and Density 46
3.3 Smooth, Rigid Pad 50
3.3.1 Load per Particle 50
3.3.2 Particle-Coating Contact 50
3.4 Smooth, Elastic Pad 55
3.4.1 Load per Particle 55
3.4.2 Particle-Pad Contact 57
3.4.3 Particle-Coating Contact 62

3.5 Rough Pad – Hemi-Spherical Asperities 64
3.5.1 Load per Particle 64
3.5.2 Elastic Analysis of an Asperity 68
3.5.3 Particle-Pad Contact: Elastic Contact 70
3.5.4 Particle-Coating Contact: Plastic Contact 72
3.5.5 Plastic Analysis of Pad Asperities 73
3.6 A Criterion for Scratching 75
3.7 Summary 85
Nomenclature 86

CHAPTER 4 EXPERIMENTAL VALIDATION OF THE SCRATCHING MODELS 87
4.1 Introduction 87
4.2 Apparatus 87
4.3 Indentation Experiments 89
4.4 Single-Particle Contact Models: Scratching Experiments 95
4.5 Multi-Particle Contact Models: Polishing Experiments 107
4.6 Summary 112

CHAPTER 5 CONCLUSIONS 114
5.1 Summary 114
5.2 Suggestions for Future Work 115

APPENDIX A ROUGH PAD – SINUSOIDAL ASPERITIES 117
Nomenclature 121

APPENDIX B PAD INDENTATION DATA 122

REFERENCES 125

List of Figures

Figure 1.1	Graph of the number of components per integrated circuit over time [Moore, 1965].	12
Figure 1.2	Graph of the number of components per chip over time [Chang and Sze, 1996].	12
Figure 1.3	Cross-section of a device with 12 metal interconnect layers (IBM).	13
Figure 1.4	Schematic of (a)-(c) inter-level dielectric CMP and (d)-(f) metal CMP [Noh, 2005].	14
Figure 1.5	Schematic of Cu interconnects embedded in the SiO_2 dielectric.	16
Figure 1.6	Schematic of the CMP process [Noh, 2005].	18
Figure 1.7	An example of nano-scale scratching in CMP from Intel.	20
Figure 2.1	Schematic of two spheres in elastic contact.	24
Figure 2.2	Schematic of contact pressure distribution.	26
Figure 2.3	Schematic of the geometry of a hard particle in elastic contact with a smooth, homogenous coating.	26
Figure 2.4	Schematic of a hard particle in contact with a homogenous coating at the onset of yielding.	29
Figure 2.5	Schematic of a hard particle scratching a soft, homogenous coating.	32
Figure 2.6	Schematic of a rigid particle in elastic contact with a composite coating.	35
Figure 2.7	Effective Young's modulus of the composite coating versus the Cu area fraction.	35
Figure 2.8	Schematic of a hard particle scratching a composite coating.	38
Figure 2.9	Geometry of a particle scratching a homogenous coating.	40
Figure 3.1	Idealized pad-particle-coating mechanical interactions in CMP.	47
Figure 3.2	Schematic showing particle size and spacing for R = 100 nm, v_f = 0.05, asperity radius, R_a = 6 μm, asperity spacing, λ_a = 100 μm, and asperity contact area radius, a_a = 1 μm.	49
Figure 3.3	Schematic of a smooth, rigid pad in contact with multiple particles.	51
Figure 3.4	Schematic of a hard particle in plastic contact with a soft coating.	51

Figure 3.5 Schematic of a smooth, elastic pad in contact with particles and a coating in: (a) Regime 1 where the pad does not touch the coating (b) the transition point where the pad just touches the coating (c) Regime 2 where the pad makes contact with the particles and the coating. 56

Figure 3.6 Schematic of a smooth pad in contact with particles, which are in contact with the coating (Regime 1). 58

Figure 3.7 Schematic of a hard particle in contact with a smooth, elastic pad. 58

Figure 3.8 Schematic of a rough pad in contact with particles. 65

Figure 3.9 A magnified schematic of an asperity deforming (a) elastically and (b) plastically. 65

Figure 3.10 Schematic of particle-asperity spacing: (a) Regime 1, where $\lambda_p < \lambda_a$ and there is at least one particle under each asperity (b) Regime 2, where $\lambda_p > \lambda_a$ and it is not guaranteed that there is at least one particle under each asperity. 66

Figure 3.11 3D image of a Rohm and Haas IC1000 pad obtained with an Olympus LEXT Confocal Microscope. 67

Figure 3.12 Image of a Rohm and Haas IC1000 pad and profile of section A-A obtained with an Olympus LEXT Confocal Microscope. 67

Figure 3.13 Schematic of the pad asperity and the coating deforming plastically: (a) $a_p < R$, (b) $a_p = R$ and (c) asperity collapse after $a_p = R$. 76

Figure 3.14 Normalized particle penetration into a plastic pad and Cu coating. $H_c = 1.22$ GPa. 80

Figure 3.15 Normalized particle penetration into a coating and pad. The shaded region represents elastic-plastic transition. The four regions represent different combinations of the pad or coating deforming elastically or plastically. 81

Figure 3.16 A plastic pad in contact with rigid particles, which in turn are in contact with four different coatings: low-k dielectrics A and B, SiO_2 and Cu. The solid lines represent the coatings deforming plastically and the dotted, red lines represent the transition from elastic to plastic deformation in the coatings and pad. 83

Figure 4.1 Hysitron TriboIndenter (Source: Hysitron Inc.). 88

Figure 4.2 Interior view of the Hysitron TriboIndenter. The three heads from left to right are: the AFM imaging tool, the scratching/indenting instrument, and the optical head. A sample is located on the magnetic stage directly 88

underneath the AFM imaging head.

Figure 4.3 Three different samples used in the Hysitron TriboIndenter. From left to right: low-k dielectric B, Cu and composite Cu/low-k dielectric B. 90

Figure 4.4 (a) Berkovich tip and (b) Cono-spherical tip (Source: Hysitron Inc.). 90

Figure 4.5 Indentation data for a Cu coating. 92

Figure 4.6 Indentation data for a low-k dielectric A coating. 93

Figure 4.7 Normal load and normal displacement during a scratch test on Cu. 97

Figure 4.8 SEM micrographs of scratches made on a Cu coating at (a) $P = 392$ μN (top row) and $P = 277$ μN (bottom row), and $v = 0.33$ μm/s, (b) $P = 277$ μN and $v = 0.33$ μm/s (magnified). 98

Figure 4.9 AFM image of a scratch made on a Cu coating at $P = 277$ μN and $v = 0.33$ μm/s. 98

Figure 4.10 SEM micrographs of scratches made on a composite Cu/low-k dielectric A coating at $P = 180$ μN and $v = 0.33$ μm/s. 99

Figure 4.11 AFM image of a scratch made on a composite Cu/low-k dielectric B coating at $P = 43$ μN and $v = 0.33$ μm/s. 99

Figure 4.12 Comparison of the upper-bound load, P_{UB}, with the experimentally measured normal load, P. 103

Figure 4.13 Comparison of the normalized upper-bound load with the normalized experimentally measured normal load. 104

Figure 4.14 Coefficient of friction (tip radius 800 nm). 106

Figure 4.15 The face-up CMP tool. 108

Figure 4.16 (a) An overview of the polishing head and (b) a close up of a Cu sample during a test. 108

Figure 4.17 Scratches formed during a CMP experiment, using particles 3 μm in size, on: (a) a Cu coating and (b) a low-k dielectric B coating. 109

Figure 4.18 Micrographs following a CMP experiment, using particles 90 nm in size, on: (a) Cu, (b) low-k dielectric B and (c) SiO_2. 111

Figure 4.19 Agglomerated particles, nominally 3 μm in size, on the surface of the low-k dielectric B coating. 113

Figure A.1 Topography of a Rohm and Haas IC1000 pad. Image taken with an Olympus LEXT Confocal Microscope. $R_q = 25.3$ μm. 118

Figure A.2 Schematic of a rough pad with sinusoidal asperities. 118

Figure B.1 Variation of pad modulus for a Rohm and Haas IC1000 pad (dry). 123

Figure B.2 Variation of pad hardness for a Rohm and Haas IC1000 pad (dry). 124

List of Tables

Table 1.1	Dielectric constant and material properties of SiO2, low-k dielectric A, low-k dielectric B and Cu.	18
Table 1.2	Average and root-mean-square roughness of coatings after CMP.	20
Table 2.1	Young's modulus and hardness of typical CMP materials.	32
Table 3.1	Widths and depths of particle penetration into a Cu coating for a rigid pad. R = 100 nm, v_f = 0.05, H_c = 1.22 GPa.	53
Table 3.2	Widths and depths of particle penetration into a smooth, elastic pad. R = 100 nm, v_f = 0.05, E_p = 0.5 GPa.	60
Table 3.3	Widths and depths of particle penetration into a Cu coating. R = 100 nm, v_f = 0.05, H_c = 1.22 GPa.	63
Table 3.4	Widths and depths of particle penetration into a rough, elastic pad. R = 100 nm, v_f = 0.05, E_p = 0.5 GPa, R_a = 5 µm, λ_a = 100 µm.	71
Table 3.5	Widths and depths of particle penetration into a Cu coating using a rough, elastic pad. R = 100 nm, v_f = 0.05, H_c = 1.22 GPa, E_p = 0.5 GPa, R_a = 5 µm, λ_a = 100 µm.	74
Table 3.6	Summary of rough pad equations for a pad with hemi-spherical asperities.	78
Table 4.1	Young's modulus and hardness of coatings and pad materials.	94
Table 4.2	Data from TriboIndenter scratch experiments on six different coatings: Cu, low-k dielectric A, low-k dielectric B, SiO_2, composite Cu/low-k dielectric A and composite Cu/low-k dielectric B. E = elastic and P = plastic deformation.	100
Table 4.3	Theoretical and experimental values of the Preston constant of Cu, low-k dielectric A and low-k dielectric B.	106
Table A.1	Summary of rough pad equations for a pad with sinusoidal asperities.	120
Table B.1	Modulus and hardness of a dry Rohm and Haas IC 1000 pad.	122

CHAPTER 1

INTRODUCTION

1.1 Background

In 1965, Dr. Gordon E. Moore, a pioneer of integrated circuit (IC) technology, had observed that the number of components per integrated circuit approximately double every year, the so-called "Moore's Law." Figure 1.1 is a graph from Moore's 1965 paper [Moore, 1965]. Since 1965, "Moore's Law" has remained roughly accurate. Figure 1.2 shows, however, that the historical data match more closely with a doubling of components every two years, rather than every year. As of 2006, the ICs have approximately 1.7 billion transistors per chip. In order for this trend to have persisted for over four decades, the semiconductor manufacturing industry has had to innovate enabling technologies to meet the demands of ultra-large-scale-integrated (ULSI) electronics.

One such enabling technology is the chemical-mechanical planarization (CMP) process. As more and more transistors are crammed at the device level of an IC, ever increasing levels of interconnects are required above that level. As of 2005, the number of interconnect levels above the device level was 11 [ITRS Roadmap]. Figure 1.3 shows a cross-section of a semiconductor device with 12 metal layers.

Chemical-mechanical planarization is both a surface planarization and a polishing process. Two different types of CMP are used in IC manufacturing: inter-level dielectric CMP and metal CMP [Kaufman *et al.*, 1991; Lai *et al.*, 2002; Yi, 2005]. In inter-level dielectric CMP, Al strips are created by lithography and then a uniform layer of SiO_2 is deposited over the Al interconnects. Then, CMP is used to planarize the remaining SiO_2. This process is shown schematically in Figure 1.4(a)-1.4(c). In metal CMP, the dual-damascene process is employed. First, a uniform layer of SiO_2 is deposited over a planar surface. Then, photolithography is used to create narrow trenches (on the order of 100 nm wide) and vertical vias in the surface of the SiO_2 followed by the deposition of a uniform layer of metal (in most cases Cu) over the SiO_2. Finally, metal CMP is used to planarize the remaining metal, as shown in Figure 1.4(d)-1.4(f).

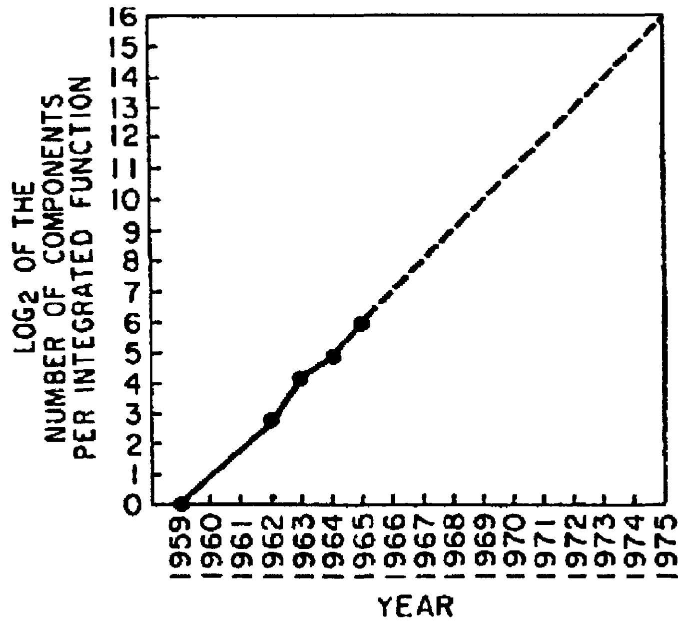

Figure 1.1: Graph of the number of components per integrated circuit over time [Moore, 1965].

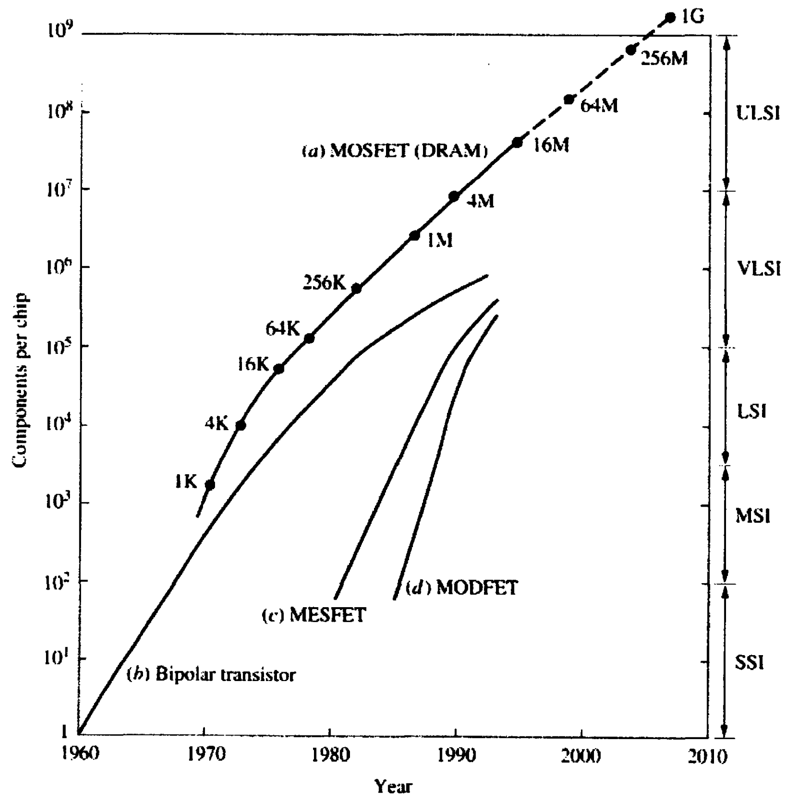

Figure 1.2: Graph of the number of components per chip over time [Chang and Sze, 1996].

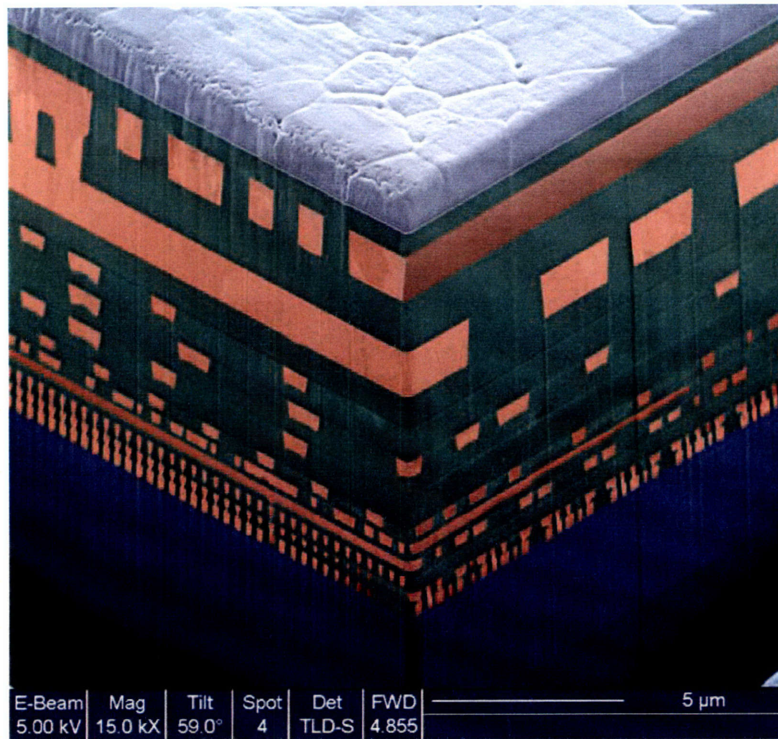

Figure 1.3: Cross-section of a device with 12 metal interconnect layers (IBM).

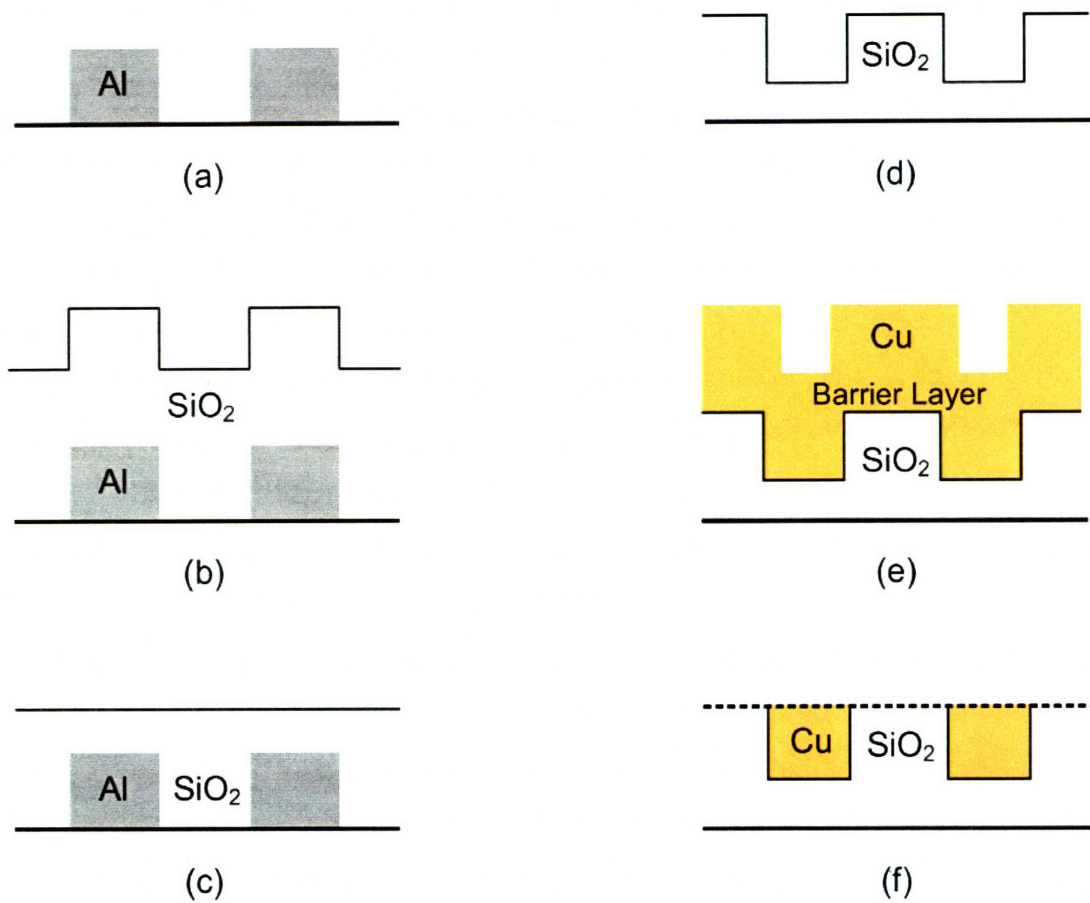

Figure 1.4: Schematic of (a)-(c) inter-level dielectric CMP and (d)-(f) metal CMP [Noh, 2005].

Due to its low electrical resistivity, recently Cu has emerged as the preferred interconnect material, and the dual-damascene process utilizing Cu is the industrial standard. Therefore, in this thesis, only Cu CMP will be addressed and the term CMP generally refers to copper chemical-mechanical planarization.

1.2 Copper/Low-k Dielectric Interconnects and CMP

As the number of transistors at the device level of an IC has increased, so too have the number of metal interconnect layers. But the widths of the metal interconnects on the first metal layer must continuously shrink, for the first metal layer interconnects make local, transistor-to-transistor connections. Recently, the width of interconnects on the first metal layer has shrunk to below 60 nm. Due to the small width between the insulating materials, the RC delay in the interconnects has greatly increased. RC time delay is the most common measure of the interconnect delay and is the time taken for the voltage at one end of an interconnect to reach 63% of a step-voltage imposed at the other end. Figure 1.5 shows a schematic of Cu/SiO_2 interconnects.

The resistance, R, of the interconnect is given by:

$$R = \rho \frac{l}{wh} \tag{1.1}$$

where ρ is the electrical resistivity, w is the width, h is the height and l is the length of the interconnect. The capacitance, C, is given by:

$$C = k\varepsilon_0 \frac{lh}{\lambda - w} \tag{1.2}$$

where k is the dielectric constant of the insulating material, ε_0 is the permittivity of free space (a constant) and λ is the pitch of the metal interconnects. Therefore, the RC time delay is given by:

$$RC = \rho k\varepsilon_0 \frac{l^2}{w(\lambda - w)} \tag{1.3}$$

Thus, as the width of the metal interconnects, w, and the width of the insulating material, $\lambda - w$, continue to shrink, the RC time delay increases [Steigerwald *et al.*, 1997]. There are only two methods of reversing the increase in the RC delay: decrease the resistivity of the metal interconnects, and/or decrease the dielectric constant of the insulating material [Ma *et al.*, 1998;

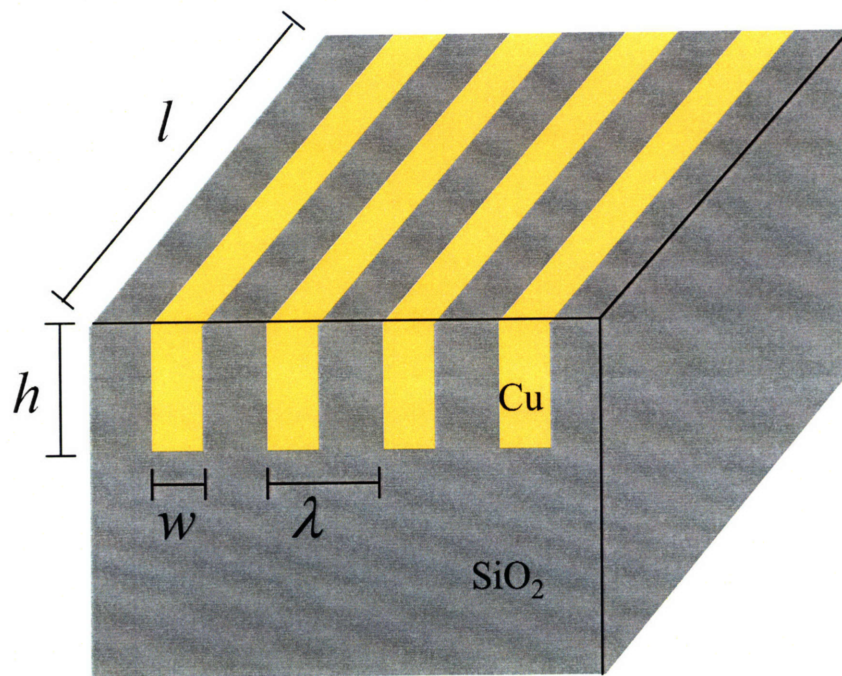

Figure 1.5: Schematic of Cu interconnects embedded in the SiO_2 dielectric.

Chen *et al.*, 1999; Martin *et al.*, 2000; Wrschka *et al.*, 2000; Maier, 2001; Maex *et al.*, 2003]. The semiconductor industry has already changed the electrical resistivity of the interconnects by replacing Al with Cu. The only metal with an electrical resistivity less than that of Cu is Ag, but the difference is negligibly small. Therefore, the semiconductor industry is now attempting to replace SiO_2, which has a dielectric constant of about 3.9, with low-k dielectrics [Morgen *et al.*, 2000]. Low-k dielectrics are insulators that have dielectric constants less than that of SiO_2. Current low-k dielectrics are variations of doped SiO_2 with porosity on the order of 30%. The dielectric constants of these materials are in the range 3.05-2.50, a significant reduction. However, despite their superior electrical properties, the low-k dielectrics have poor mechanical properties [Neirynck *et al.*, 1996; Borst *et al.*, 2002]. This is the current problem hindering the IC manufacturing industry from completely replacing SiO_2 with ultra-low-k dielectrics ($k < 2.5$). Table 1.1 shows the relevant electrical and mechanical properties of Cu, SiO_2, and two low-k dielectrics.

As can be seen in the table, the new low-k dielectrics have a Young's modulus an order of magnitude smaller than that of SiO_2. In addition, the hardness of the new low-k dielectrics is also an order of magnitude less than that of SiO_2. Furthermore, the new low-k dielectrics have hardnesses that are very similar to that of Cu. As a result of replacing the traditional insulator, SiO_2, with the compliant, soft low-k dielectrics, scratching during CMP has emerged as a challenging problem. The ITRS roadmap from 2000 shows that in 1999, the effective dielectric constant of interlevel dielectrics was 3.5-4.0, which essentially means that in 1999 SiO_2 was still predominant. The 2000 ITRS roadmap also predicted that by 2005 the effective dielectric constant of interlevel insulators would be 1.6-2.2. Thus, it was expected that by 2005, ultra-low-k dielectrics would be commonplace. However, according to the 2005 ITRS roadmap, the effective dielectric constant of interlevel insulators in 2005 was in fact 3.1-3.4. This means that the introduction of low-k dielectrics into IC manufacturing has been significantly delayed. One of the primary reasons for this delay given by the ITRS roadmap is that the new low-k dielectrics are not yet compatible with current processes, including CMP. Nano-scale scratching of low-k dielectrics during CMP is one such compatibility issue [Zhong *et al.*, 1999; Ring *et al.*, 2007].

During CMP, a wafer is pushed against a polishing pad at some pressure, typically in the range 6.9 – 69 kPa (1-10 psi). Both the pad and the wafer are rotated at a given rotational velocity [Runnels and Eyman, 1994]. A schematic of this is shown in Figure 1.6. The wafer and

Table 1.1: Dielectric constant and material properties of SiO_2, low-k dielectric A, low-k dielectric B and Cu.

Material	k	E (GPa)	H (GPa)
SiO_2	3.90	92.00	15.00
low-k A	3.05	11.10	2.09
low-k B	2.50	8.00	1.37
Cu	-	128.00	1.22

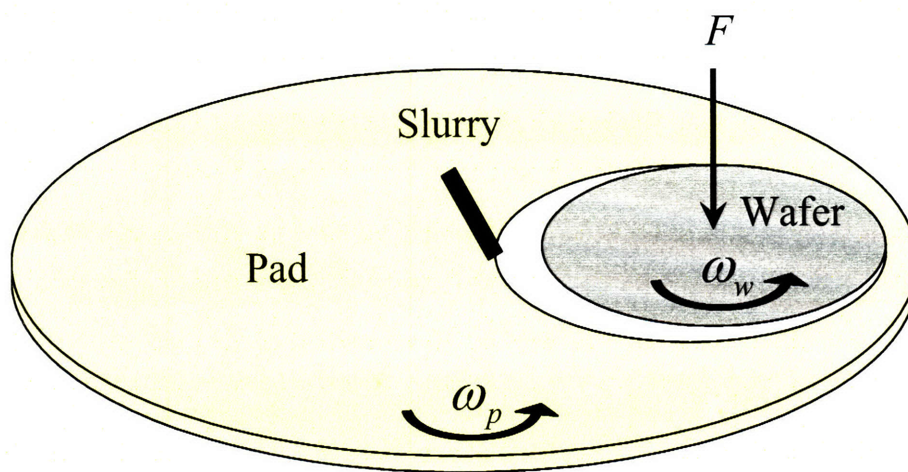

Figure 1.6: Schematic of the CMP process.

the pad are usually positioned such that their centers are off-axis, thereby ensuring the linear velocity to be constant at all points on the wafer [DeJule, 1998]. In addition, an abrasive slurry is pumped into the interface of the wafer and the pad [Cook, 1990; Gutmann *et al.*, 1995; Qin *et al.*, 2003; Teo *et al.*, 2004]. A typical slurry consists of approximately 95% H_2O, 3% H_2O_2 and 2% Al_2O_3 particles by volume. The chemical component of CMP is the reaction of the wafer surface with the slurry chemicals to form a soft layer [Che *et. al*, 2003]. The mechanical component is the removal of the softened surface by hard abrasives in the slurry [Steigerwald *et al.*, 1995; Singh and Bajaj, 2002]. The material removal rate of the excess Cu is governed by the Preston equation [Preston, 1927]:

$$\frac{dh_{Cu}}{dt} = k_p p v_r \tag{1.4}$$

where k_p is the Preston constant, p is the pressure applied to the wafer during polishing, v_r is the relative velocity of any point on the wafer surface, h_{Cu} is the thickness of the Cu coating removed and t is time.

Table 1.2 shows the average and root-mean-square roughness of three homogenous coatings after being polished by CMP at Intel. These measurements were made using a Tencor P10 Profilometer. Note that the roughness measurements are about 1 nm. Therefore, CMP is more than capable of meeting the planarization needs of the semiconductor manufacturing industry.

However, polishing nano-scale structures comprising of low-k dielectrics poses a great challenge. Since low-k dielectrics are both soft and compliant compared with SiO_2, scratching is now a dominant problem in nano-scale CMP. An example of nano-scale scratching in CMP is shown in Figure 1.7.

1.3 Thesis Organization

The overall goal of the thesis is to model scratching by hard abrasives in CMP and to propose practical solutions to mitigate scratching. Chapter 1 describes the background and organization of the thesis. In Chapter 2, single-particle models based on the contact mechanics of a rigid, spherical particle with smooth, planar coatings are introduced. The models relate the load per particle to the width and depth of a scratch based on the elastic and plastic analyses. From this, lower- and upper-bound limits for the load per particle are introduced. The models consider both

Table 1.2: Average and root-mean-square roughness of coatings after CMP.

Material	R_a (nm)	R_q (nm)
low-k A	0.24	0.29
low-k B	0.29	0.36
Cu	2.14	2.67

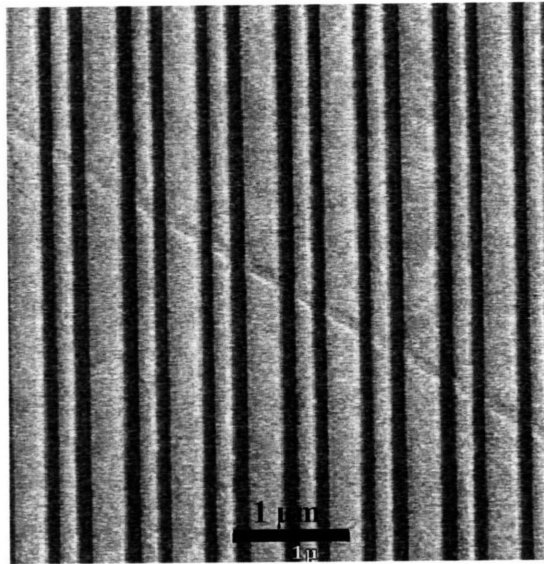

Figure 1.7: An example of nano-scale scratching in CMP from Intel.

homogenous and composite coatings. In Chapter 3, multi-particle models based on the contact mechanics of the pad-particle-coating interfaces are introduced. These models comprise again elastic and plastic analyses to relate the global, controllable parameters in CMP (pressure, particle radius, slurry volume fraction and the material and geometrical properties of the pad and coating) to the scratch width and depth. In Chapter 4, the models are validated by scratching experiments on a Hysitron TriboIndenter and by polishing experiments on a CMP tool. Finally, conclusions of the thesis and suggestions for future research on scratching in CMP are presented in Chapter 5.

Nomenclature

C = capacitance (F)

E = Young's modulus (N/m^2)

H = hardness (N/m^2)

h = thickness of metal interconnect (m)

h_{Cu} = thickness of Cu coating to be removed (m)

k = dielectric constant

k_p = Preston constant (m^2/N)

l = length of interconnect (m)

p = pressure (N/m^2)

R = resistance (Ω)

R_a = average roughness (m)

R_q = root-mean-square roughness (m)

t = time (s)

v_r = relative velocity (m/s)

w = width of Cu interconnect (m)

ε_0 = permittivity of free space (F/m)

λ = pitch of Cu interconnects (m)

ρ = electrical resistivity of the metal interconnect (Ωm)

CHAPTER 2

SINGLE-PARTICLE CONTACT MECHANICS

2.1 Introduction

This chapter introduces the contact mechanics models of a single particle interacting with a planar, smooth coating. It is assumed that the particle is spherical, and rigid compared with the coating. Hertzian analysis is used to determine a lower-bound on the load per particle for scratching on the coating surface to initiate. Fully-plastic analysis is used to define an upper-bound on the load per particle. The goal of this chapter is to relate the load per particle to the width and depth of a scratch in the coating.

2.2 Elastic Contact of Two Smooth Spheres

Figure 2.1 is a schematic of two spheres in elastic contact. For the Hertzian analysis to be valid, it is assumed that: (a) the dimensions of the contact area of the two spheres are smaller than the radii of the spheres, (b) the surfaces of the two spheres are assumed to be frictionless so that only a normal force exists between the two spheres, (c) the strains are small, and (d) the materials of the two spheres are homogeneous and isotropic. With these assumptions, each sphere can be treated as an elastic half-space which is loaded over a small region of its "planar" surface and the Hertz equations can then be used [Johnson, 1985]. The equivalent radius, R^*, of two smooth spheres is defined as:

$$\frac{1}{R^*} = \frac{1}{R_1} + \frac{1}{R_2} \tag{2.1}$$

where R_1 and R_2 are the radii of the spheres. The equivalent Young's modulus, E^*, is given by:

$$\frac{1}{E^*} = \frac{1-\nu_1^2}{E_1} + \frac{1-\nu_2^2}{E_2} \tag{2.2}$$

where E_1 and E_2 are the Young's moduli and ν_1 and ν_2 are the Poisson's ratios.

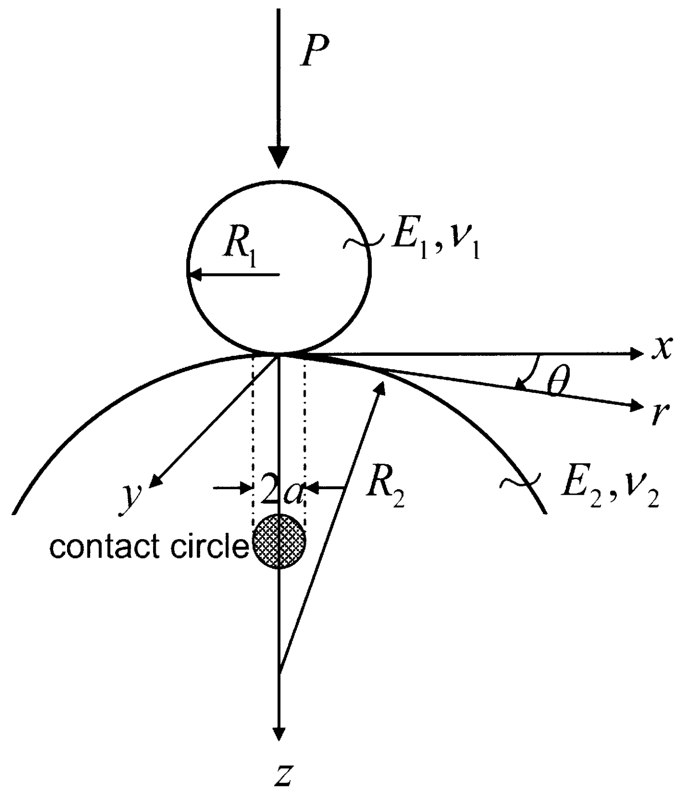

Figure 2.1: Schematic of two spheres in elastic contact.

The radius of the contact circle, a, is given by:

$$a = \left[\frac{3}{4}\frac{PR^*}{E^*}\right]^{1/3} \tag{2.3}$$

where P is the applied load. The approach of distant points, δ, is given by:

$$\delta = \frac{a^2}{R^*} = \left[\frac{9}{16}\frac{P^2}{R^* E^{*2}}\right]^{1/3} \tag{2.4}$$

The contact pressure distribution, p, is a function of the radius, r:

$$\left(\frac{p}{p_o}\right)^2 + \left(\frac{r}{a}\right)^2 = 1 \tag{2.5}$$

where p_o is the pressure at $r = 0,\ z = 0$ and is given by:

$$p_o = \frac{3}{2}\frac{P}{\pi a^2} = \left[\frac{6}{\pi^3}\frac{PE^{*2}}{R^{*2}}\right]^{1/3} \tag{2.6}$$

A diagram showing the coordinates as well as the contact region is shown in Figure 2.2. The maximum contact pressure, p_o, occurs at $r = 0,\ z = 0$. The maximum shear stress, $\tau_{\max}$, is given by:

$$\tau_{\max} = 0.31 p_o \tag{2.7}$$

and occurs at $r = 0,\ z = 0.48a$. The maximum tensile stress, $\sigma_{r,\max}$, is given by:

$$\sigma_{r,\max} = \frac{1}{3}(1 - 2\nu) p_o \tag{2.8}$$

and occurs at $r = a,\ z = 0$.

2.3 Elastic Analysis of a Homogenous Coating

The Hertzian equations presented in Section 2.2 can be adapted to model a sphere in elastic contact with a homogenous, planar surface. A schematic showing the geometry of an Al_2O_3 sphere in elastic contact with a planar, homogeneous coating is shown in Figure 2.3. In this case, the equivalent radius is given by:

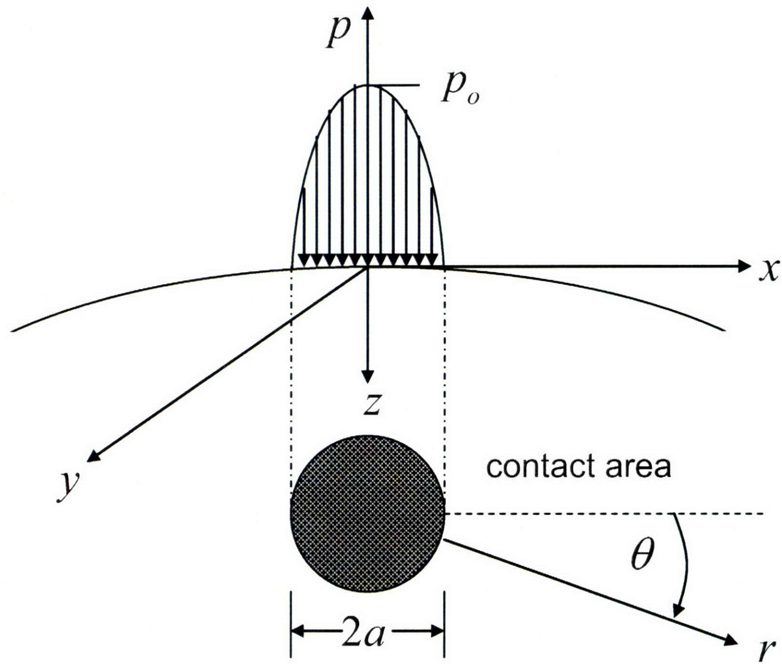

Figure 2.2: Schematic of contact pressure distribution.

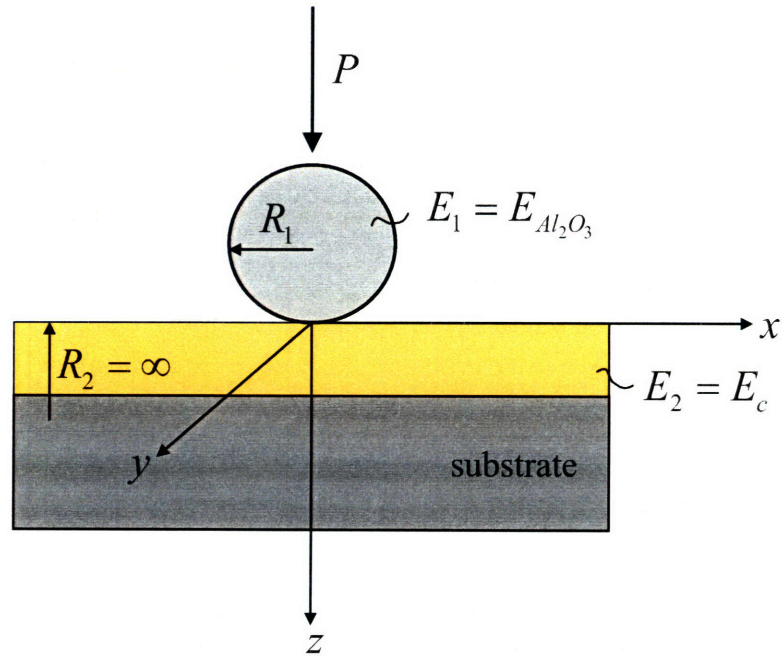

Figure 2.3: Schematic of the geometry of a hard particle in elastic contact with a smooth, homogenous coating.

$$\frac{1}{R^*} = \frac{1}{R_1} + \frac{1}{\infty} = \frac{1}{R_1} \quad (2.9)$$

where R_1 is the radius of the Al_2O_3 sphere and the radius of the smooth surface is taken to be infinity. Rearranging Eq. (2.9),

$$R^* = R_1 = R \quad (2.10)$$

where R now is equal to the radius of the Al_2O_3 sphere.

The equivalent Young's modulus is given by:

$$\frac{1}{E^*} = \frac{1 - \nu_{Al_2O_3}^2}{E_{Al_2O_3}} + \frac{1 - \nu_c^2}{E_c} \quad (2.11)$$

where $E_{Al_2O_3}$ and $\nu_{Al_2O_3}$ are the Young's modulus and Poisson's ratio, respectively, of the Al_2O_3 sphere and E_c and ν_c are the Young's modulus and Poisson's ratio, respectively, of the planar coating.

Eq. (2.11) can be simplified by the following approximations:

$$1 - \nu_{Al_2O_3}^2, 1 - \nu_c^2 \approx 1 \quad (2.12)$$

and

$$E_{Al_2O_3} > E_c \quad (2.13)$$

Eq. (2.11) then simplifies to:

$$E^* \approx E_c \quad (2.14)$$

In the elastic regime, the radius of the contact area circle between the particle and the coating, a_c, is calculated by substituting Eqs. (2.10) and (2.14) into Eq. (2.3):

$$a_c = \left[\frac{3}{4} \frac{PR}{E_c} \right]^{1/3} \quad (2.15)$$

The approach of distant points in the elastic regime, δ_c, is obtained by substituting Eqs. (2.10) and (2.14) into Eq. (2.4):

$$\delta_c = \frac{a_c^2}{R} = \left[\frac{9}{16} \frac{P^2}{RE_c^2} \right]^{1/3} \quad (2.16)$$

The maximum contact pressure, in the elastic regime, between the sphere and the coating is obtained by substituting Eqs. (2.10) and (2.14) into Eq. (2.6):

$$p_o = \frac{3}{2}\frac{P}{\pi a_c^2} = \left[\frac{6}{\pi^3}\frac{PE_c^2}{R^2}\right]^{1/3} \tag{2.17}$$

The above three equations are valid while the contact between the sphere and the coating remains in the elastic regime.

Figure 2.4 shows a schematic of a particle in contact with a homogenous coating at the yield point. At the onset of yield, the radius of the contact circle, a_Y, is calculated by:

$$a_{Y,c} = \left[\frac{3}{4}\frac{P_{Y,c}R}{E_c}\right]^{1/3} \tag{2.18}$$

where $P_{Y,c}$ is the yield load of the coating applied by the Al_2O_3 sphere. At yield, the approach of distant points, $\delta_{Y,c}$, is given by:

$$\delta_{Y,c} = \left[\frac{9}{16}\frac{P_{Y,c}^2}{RE_c^2}\right]^{1/3} \tag{2.19}$$

The maximum contact pressure at yield, $p_{o,Y}$, is given by:

$$p_{o,Y} = \left[\frac{6}{\pi^3}\frac{P_{Y,c}E_c^2}{R^2}\right]^{1/3} \tag{2.20}$$

The above three equations are valid at the onset of yielding and thus can be used in conjunction with different yield criteria in order to explicitly solve for the yield load of the coating, $P_{Y,c}$. Two common yield criteria in solid mechanics are the Mises criterion and the Tresca criterion [Johnson, 1985]. The Mises criterion is given by:

$$\frac{1}{6}\left\{(\sigma_1-\sigma_2)^2+(\sigma_2-\sigma_3)^2+(\sigma_3-\sigma_1)^2\right\} = k^2 = \frac{\sigma_Y^2}{3} \tag{2.21}$$

where σ_1, σ_2, σ_3 are the principal stresses, k is the yield strength in shear and σ_Y is the yield strength in tension or compression. The Tresca criterion is given by:

$$\max\left\{|\sigma_1-\sigma_2|,|\sigma_2-\sigma_3|,|\sigma_3-\sigma_1|\right\} = 2k = \sigma_Y \tag{2.22}$$

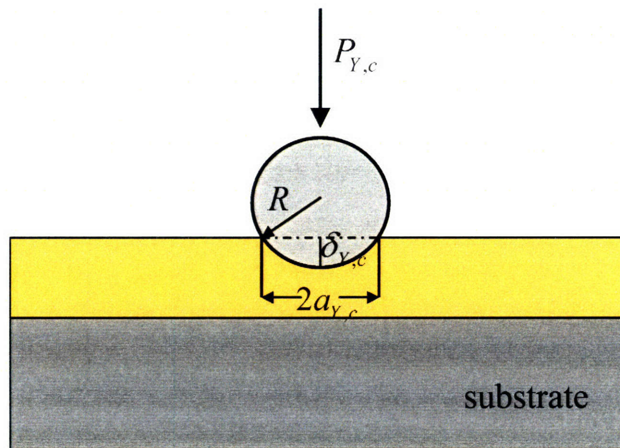

Figure 2.4: Schematic of a hard particle in contact with a homogenous coating at the onset of yielding.

or

$$\tau_{\max} = k = \frac{\sigma_Y}{2} \tag{2.23}$$

For simplicity, the Tresca criterion may be used for yielding. Therefore, by substituting Eq. (2.7) into the Tresca yield criterion (i.e., Eq. (2.23)), the maximum shear stress at yield, $\tau_{\max,Y}$, is given by:

$$\tau_{\max,Y} = 0.31 p_{o,Y} = k = \frac{\sigma_{Y,c}}{2} \tag{2.24}$$

where $\sigma_{Y,c}$ is the yield strength of the coating. Substituting Eq. (2.20) into Eq. (2.24) gives:

$$0.31\left[\frac{6}{\pi^3}\frac{P_{Y,c}E_c^{\,2}}{R^2}\right]^{1/3} = \frac{\sigma_{Y,c}}{2} \tag{2.25}$$

Eq. (2.25) can be rewritten as:

$$\sigma_{Y,c} = 0.62\left[\frac{6}{\pi^3}\frac{P_{Y,c}E_c^{\,2}}{R^2}\right]^{1/3} \tag{2.26}$$

By approximating 0.62 as $2/3$, Eq. (2.26) can be rewritten as:

$$\sigma_{Y,c} = \frac{2}{3}\left[\frac{6}{\pi^3}\frac{P_{Y,c}E_c^{\,2}}{R^2}\right]^{1/3} \tag{2.27}$$

Using Eq. (2.27), the yield load can be solved for:

$$P_{Y,c} = \frac{9\pi^3}{16}\frac{\sigma_{Y,c}^{\,3}}{E_c^{\,2}}R^2 \tag{2.28}$$

Therefore, for a given coating with a Young's modulus of E_c and yield strength of $\sigma_{Y,c}$ and a particle with a radius of R, the transition load between the elastic and plastic deformation regimes is given by $P_{Y,c}$ in Eq. (2.28). Because the hardness of the coating is approximated as

$$H_c = 3\sigma_{Y,c} \tag{2.29}$$

Eq. (2.28) can be rewritten as:

$$P_{Y,c} = \frac{\pi^3}{48}\frac{H_c^{\,3}}{E_c^{\,2}}R^2 \tag{2.30}$$

Table 2.1 shows a list of the modulus and hardness of typical CMP materials: Al_2O_3, SiO_2, Cu, and low-k dielectrics A and B. In commercial CMP processes, the particle size currently is of the order of 100 nm. For a 100-nm particle, the yield loads for SiO_2 and the low-k dielectrics are approximately 1 μN, whereas the yield load for Cu is three orders of magnitude smaller. Therefore, for a given particle size, it is comparably easier to initiate scratching on Cu than on the dielectrics.

Once the yield load has been explicitly solved for, the radius of the contact area at yield and the approach of distant points at yield can be expressed by substituting Eq. (2.30) into Eqs. (2.18) and (2.19), respectively, to give:

$$a_{Y,c} = \frac{\pi}{4}\frac{H_c}{E_c}R \tag{2.31}$$

and

$$\delta_{Y,c} = \frac{\pi^2}{16}\frac{H_c^2}{E_c^2}R \tag{2.32}$$

2.4 Fully-Plastic Analysis of a Homogenous Coating

For fully-plastic analysis, it assumes that (a) the coating does not undergo strain hardening (i.e., the coating will continue to strain at a constant stress) and (b) the coating does not exhibit any elastic deformation. The hardness of the coating is given by:

$$H_c = \frac{P_{UB}}{A_h} = \frac{P_{UB}}{\frac{\pi}{2}a_c^2} \tag{2.33}$$

where A_h is the horizontal projection of the contact area between the sphere and the coating due to the normal force, a_c is the semi-width of the scratch, and P_{UB} is the upper-bound normal load applied to the particle [Suh, 1986; Luo and Dornfeld, 2001]. A schematic of a particle scratching (i.e., plastically deforming) a homogenous coating is seen in Figure 2.5.

Eq. (2.33) can be rewritten to solve for the scratch semi-width:

$$a_c = \left[\frac{2P_{UB}}{\pi H_c}\right]^{1/2} \tag{2.34}$$

Table 2.1: Young's modulus and hardness of typical CMP materials.

Material	E_c (GPa)	H_c (GPa)
Diamond	1140.00	140.00
Al_2O_3	350.00	20.00
SiO_2	92.00	15.00
Cu	128.00	1.22
A	11.10	2.09
B	8.00	1.37
Rohm and Haas Pad (IC1000)	0.50	0.05
Thomas West Pad (TWI817)	0.30	0.06

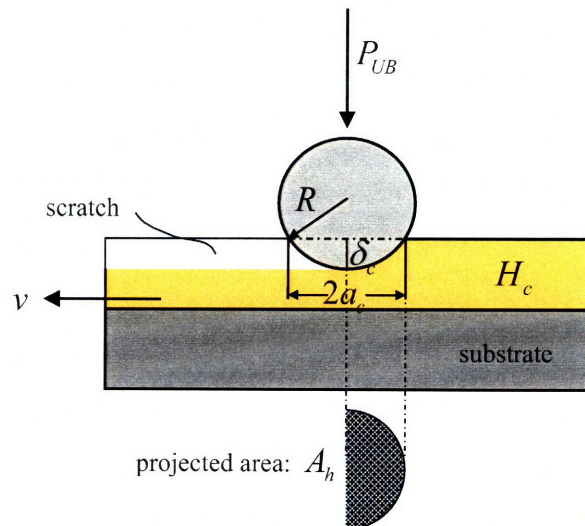

Figure 2.5: Schematic of a hard particle scratching a soft, homogenous coating.

Eq. (2.34) can be normalized by R to give:

$$\frac{a_c}{R} = \left[\frac{2P_{UB}}{\pi R^2 H_c}\right]^{1/2} \quad (2.35)$$

From the geometry of the indentation, the following expression is obtained using the Pythagorean theorem:

$$R^2 - (R - \delta_c)^2 = a_c^{\,2} \quad (2.36)$$

where δ_c is the depth of indentation of the sphere into the coating surface. Using the assumption that $\delta_c \ll R$, Eq. (2.36) can be rewritten as:

$$\frac{\delta_c}{a_c} = \frac{a_c}{2R} \quad (2.37)$$

Eq. (2.37) can alternatively be rewritten as:

$$\frac{\delta_c}{R} = \frac{a_c^{\,2}}{2R^2} = \frac{1}{2}\left(\frac{a_c}{R}\right)^2 \quad (2.38)$$

It may be noted the factor 1/2 appears in Eq. (2.38) whereas in the elastic analysis, the factor 1/2 is not present. Substituting Eq. (2.38) into Eq. (2.35) and rewriting to solve for the upper-bound load provides:

$$P_{UB} = \pi \delta_c R H_c \quad (2.39)$$

The upper-bound loads for Cu and the two low-k dielectrics A and B are very similar, whereas the upper-bound load for SiO_2 is an order of magnitude larger. This is a good indication of why scratching has recently emerged as a challenging problem in CMP. When SiO_2 was used as the insulating material, its large hardness required that the normal load be quite large for scratching to occur. Therefore, in the composite coatings consisting of Cu lines alternating with SiO_2 lines, the SiO_2 provides a certain degree of protection for the Cu interconnects against scratching. However, now that the semiconductor industry has changed the insulating material from SiO_2 to low-k dielectrics, which have hardnesses similar to that of Cu and thus similar upper-bound loads, the insulating material no longer provides protection in the composite coatings, and thus scratching takes place during CMP.

2.5 Elastic Analysis of a Composite Coating

The equivalent radius of the spherical particle and composite coating is given by Eqs. (2.9) and (2.10). The equivalent Young's modulus of the particle-composite contact is given by:

$$\frac{1}{E^*} = \frac{1-\nu_{Al_2O_3}{}^2}{E_{Al_2O_3}} + \frac{1-\nu_{eff}{}^2}{E_{eff}} \tag{2.40}$$

where E_{eff} and ν_{eff} is the Young's modulus and Poisson's ratio, respectively, of the composite coating. Figure 2.6 shows an aluminum oxide particle in elastic contact with a composite coating consisting of Cu and a low-k dielectric.

Using the following approximations:

$$1-\nu_{Al_2O_3}{}^2, 1-\nu_{eff}{}^2 \approx 1 \tag{2.41}$$

and

$$E_{Al_2O_3} > E_{eff} \tag{2.42}$$

Eq. (2.40) simplifies to:

$$E^* \approx E_{eff} \tag{2.43}$$

The Young's modulus of the composite surface, E_{eff}, can be calculated using two different assumptions: an upper-bound, parallel assumption and a lower-bound, perpendicular assumption. The upper-bound assumes that the Cu and low-k dielectric act like parallel springs. Therefore

$$E_{parallel} = E_{Cu}\left(\frac{w}{\lambda}\right) + E_d\left(\frac{\lambda - w}{\lambda}\right) \tag{2.44}$$

where E_{Cu} is the Young's modulus of Cu, E_d is the Young's modulus of the low-k dielectric, w is the linewidth of the Cu interconnect, and λ is the pitch of the patterned lines. The lower-bound assumes that the Cu and dielectric act like springs in series. Therefore

$$\frac{1}{E_{perpendicular}} = \frac{1}{E_{Cu}}\left(\frac{w}{\lambda}\right) + \frac{1}{E_d}\left(\frac{\lambda - w}{\lambda}\right) \tag{2.45}$$

Figure 2.7 shows a graph of the effective Young's modulus for a composite coating versus the area fraction of Cu, w/λ. Both the upper-bound (parallel springs) and lower-bound (series springs) have been plotted for composite coatings consisting of Cu with the two low-k dielectrics

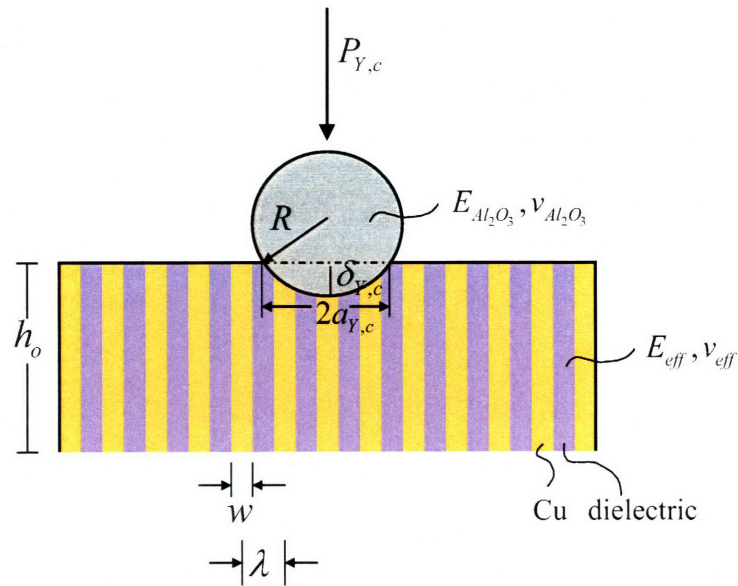

Figure 2.6: Schematic of a rigid particle in elastic contact with a composite coating.

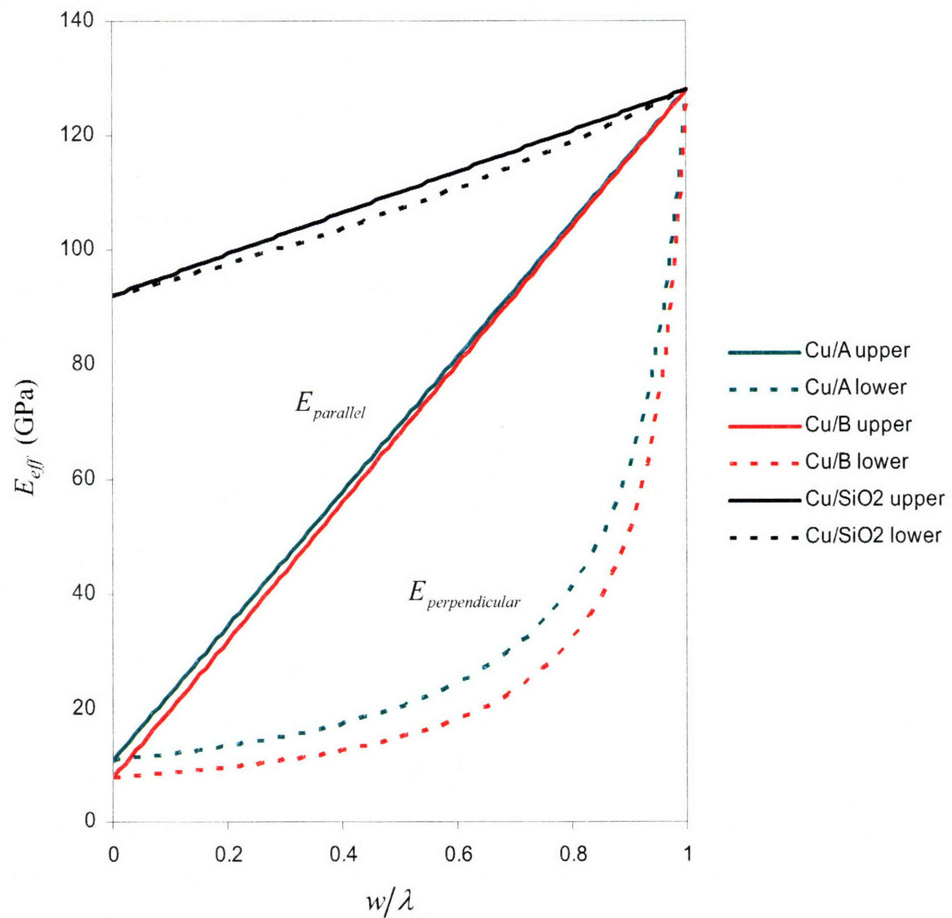

Figure 2.7: Effective Young's modulus of the composite coating versus the Cu area fraction.

as well as Cu with SiO_2.

For the Hertzian analysis used in this thesis, $E_{parallel}$ is more relevant. Therefore, the effective Young's modulus of the composite coating is given by:

$$E^* \approx E_{eff} = E_{parallel} = E_d + \frac{w}{\lambda}\left(E_{Cu} - E_d\right) \tag{2.46}$$

Eqs. (2.10) and (2.46) can be substituted into Eq. (2.3) so that the radius of contact in the elastic regime is given by:

$$a_c = \left[\frac{3}{4}\frac{PR}{E_d + \frac{w}{\lambda}\left(E_{Cu} - E_d\right)}\right]^{1/3} \tag{2.47}$$

The approach of distant points in the elastic regime is given by combining Eqs. (2.4), (2.10) and (2.46):

$$\delta_c = \left[\frac{9}{16}\frac{P^2}{R\left(E_d + \frac{w}{\lambda}\left(E_{Cu} - E_d\right)\right)^2}\right]^{1/3} \tag{2.48}$$

At the onset of yielding, the radius of the contact area is given by:

$$a_{Y,c} = \left[\frac{3}{4}\frac{P_{Y,c}R}{E_d + \frac{w}{\lambda}\left(E_{Cu} - E_d\right)}\right]^{1/3} \tag{2.49}$$

In addition, at the onset of yielding the approach of distant points is given by:

$$\delta_{Y,c} = \left[\frac{9}{16}\frac{P_{Y,c}^{\ 2}}{R\left(E_d + \frac{w}{\lambda}\left(E_{Cu} - E_d\right)\right)^2}\right]^{1/3} \tag{2.50}$$

The strain based criterion for yielding is given as:

$$\frac{\delta_{Y,c}}{h_o} = \varepsilon_Y = \frac{\sigma_{Y,Cu}}{E_{Cu}} = \frac{1}{3}\frac{H_{Cu}}{E_{Cu}} \tag{2.51}$$

where ε_Y is the yield strain and h_o is the thickness of the composite coating. A strain-based criterion for yielding is used for the composite coating because although the hardnesses, and thus

yield strengths, of Cu and the low-k dielectrics are similar, their Young's moduli are vastly different. When a Cu line yields under load, the low-k dielectrics are still in the elastic regime. Therefore, the yield strain for Cu is used as the criterion for the composite coating, as show in Eq. (2.51). Eq. (2.50) can be substituted into Eq. (2.51) to provide:

$$\varepsilon_Y = \frac{1}{3}\frac{H_{Cu}}{E_{Cu}} = \frac{1}{h_o}\left[\frac{9}{16}\frac{P_{Y,c}^{\;2}}{R\left(E_d + \frac{w}{\lambda}\left(E_{Cu} - E_d\right)\right)^2}\right]^{1/3} \tag{2.52}$$

By rewriting Eq. (2.52), the yield load can be solved for:

$$P_{Y,c} = \left[\frac{16}{9}\left(h_o \frac{1}{3}\frac{H_{Cu}}{E_{Cu}}\right)^3 R\left(E_d + \frac{w}{\lambda}\left(E_{Cu} - E_d\right)\right)^2\right]^{1/2} \tag{2.53}$$

Eq. (2.53) can be simplified to:

$$\frac{P_{Y,c}}{\sqrt{Rh_o^{\;3}}} = \frac{4}{9\sqrt{3}}\left(\frac{H_{Cu}}{E_{Cu}}\right)^{3/2}\left(E_d + \frac{w}{\lambda}\left(E_{Cu} - E_d\right)\right) \tag{2.54}$$

The yield load increases linearly as the area fraction of Cu increases, because as the area fraction increases the effective Young's modulus of the coating increases linearly and therefore more load is required to reach the yield point. In addition, as the particle size increases, the load increases as the one-half power. This is consistent with elastic, Hertzian analysis. It may be noted that for an area fraction of 0.5 and for a particle with a radius of 100 nm, the yield load is approximately 5 μN.

2.6 Fully-Plastic Analysis of a Composite Coating

The hardness of a homogenous coating is given by Eq. (2.33). However, because the coating consists of two different materials, Cu and a low-k dielectric, it is necessary to combine the hardnesses of the two materials into one effective hardness. This can be done approximately by weighting the hardness of each material by the area fraction of each material:

$$H_c = H_{eff} = H_{Cu}\left(\frac{w}{\lambda}\right) + H_d\left(\frac{\lambda - w}{\lambda}\right) \tag{2.55}$$

Figure 2.8 shows the geometry of a particle in plastic contact with a composite coating. Interestingly, the hardness of the low-k dielectrics now used is comparable to the hardness

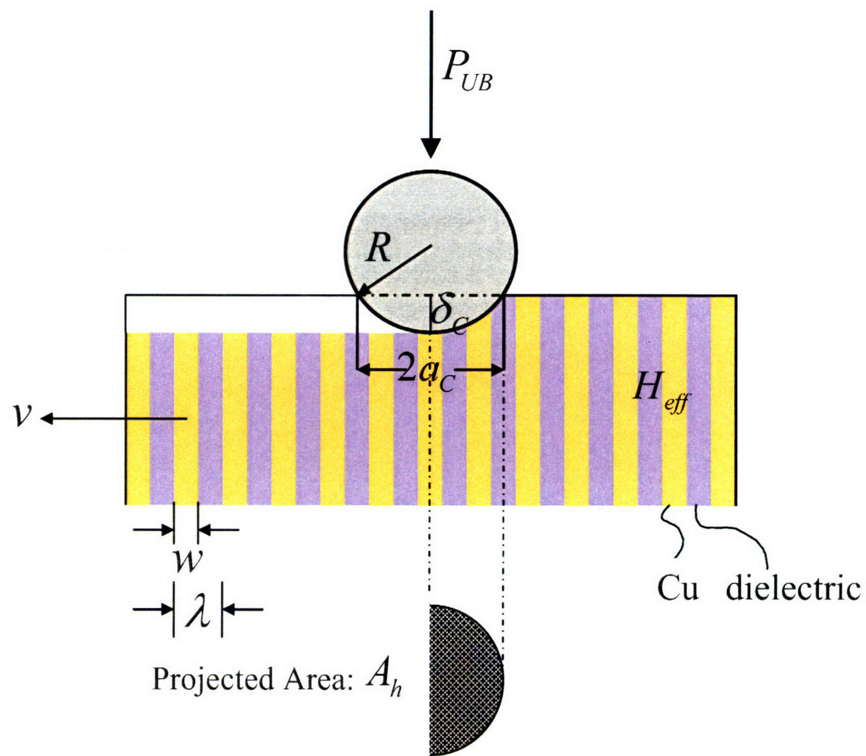

Figure 2.8: Schematic of a hard particle scratching a composite coating.

of Cu. Therefore, the weighting scheme used in Eq. (2.55) may not even be necessary. The hardness of Cu can be used as an approximate simplification for the hardness of the composite coating. This is not true in the case of composite coatings that consist of Cu and SiO_2. The hardness of SiO_2 is an order of magnitude larger than that of Cu, thus this is one of the reasons why scratching has emerged as a threatening problem now that the dielectrics have hardnesses equal to Cu. Eq. (2.55) can be substituted into the homogenous expression for an upper-bound load, Eq. (2.39), to provide:

$$P_{UB} = \pi\delta_c R\left[H_d + \frac{w}{\lambda}\left(H_{Cu} - H_d\right)\right] \tag{2.56}$$

2.7 Coefficient of Friction

The coefficient of friction, μ, is defined as:

$$\mu = \mu_p + \mu_{ad} = \frac{F}{P} \tag{2.57}$$

where F is the tangential force, μ_p is the coefficient of plowing friction and μ_{ad} is the coefficient of adhesion friction [Suh, 1986]. Using the upper-bound load definitions for the normal and tangential forces,

$$P = H_c A_h \tag{2.58}$$

and

$$F = H_c A_v \tag{2.59}$$

Eq. (2.57) can be rewritten approximately as:

$$\mu_p = \frac{A_v}{A_h} \tag{2.60}$$

where A_v is the vertical projection of the contact area due to the tangential force. Figure 2.9 shows the geometry of a particle scratching the surface of a homogenous coating.

During scratching, the horizontal projected area is given by:

$$A_h = \frac{\pi a_c^{\ 2}}{2} \tag{2.61}$$

It may be noted that the factor 1/2 appears here because it is assumed that the particle is sliding and hence is only supported by the front half of the particle. If it were a stationary, indentation test, the particle would be supported by the back half as well and the factor 1/2 would not be

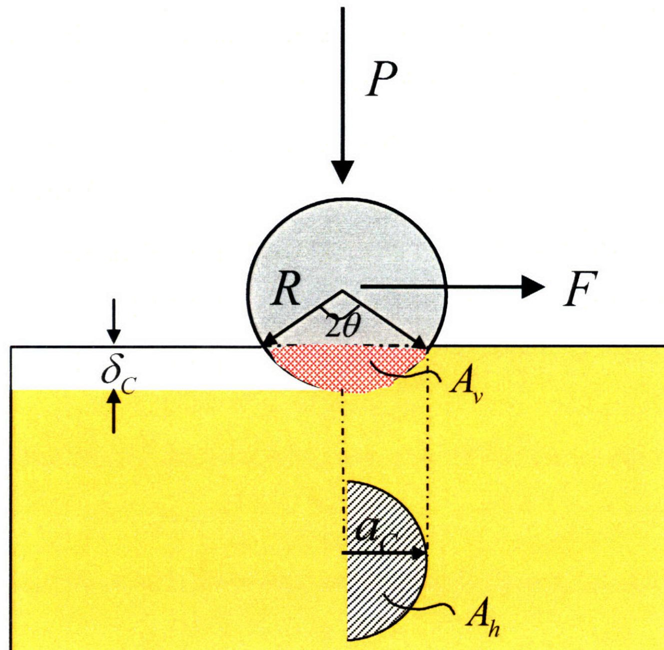

Figure 2.9: Geometry of a particle scratching a homogenous coating.

present. The vertical projected area is given by:

$$A_v = \frac{2\theta}{2\pi}\pi R^2 - a_c(R-\delta_c) \tag{2.62}$$

where θ is the angle of contact with respect to the z-axis. Using the assumption that $\delta \ll R$, Eq. (2.62) simplifies to:

$$A_v = \theta R^2 - a_c R \tag{2.63}$$

and from geometry:

$$\sin\theta = \frac{a_c}{R} \tag{2.64}$$

Therefore, Eq. (2.63) simplifies to:

$$A_v = R^2\left[\sin^{-1}\left(\frac{a_c}{R}\right) - \frac{a_c}{R}\right] \tag{2.65}$$

By combining Eqs. (2.60), (2.61) and (2.65), the coefficient of plowing friction is expressed as:

$$\mu_p = \frac{2}{\pi}\frac{R^2}{a_c^{\,2}}\left[\sin^{-1}\left(\frac{a_c}{R}\right) - \frac{a_c}{R}\right] \tag{2.66}$$

In order to calculate the coefficient of plowing friction using Eq. (2.66), it is necessary to know the size of the particle and the observed scratch width. Usually, the particle size will not be a known factor, but something that must be figured out from observable variables. Therefore, using Eq. (2.37), Eq. (2.66) can be written in terms of the observed scratch width and depth as:

$$\mu_p = \frac{\frac{2}{\pi}\left[\sin^{-1}\left(\frac{2\delta_c}{a_c}\right) - \frac{2\delta_c}{a_c}\right]}{\left(\frac{2\delta_c}{a_c}\right)^2} \tag{2.67}$$

2.8 Preston Constant

The wear coefficient, k_w, is defined as:

$$k_w = \frac{VH_c}{PS} \tag{2.68}$$

where V is the volume of material removed by the particle during scratching and S is the lateral distance traveled by the particle. The volume of material removed by the particle is equal to the product of the projected area in the vertical direction, A_v, and the distance traveled. In addition,

the upper-bound definition for the normal load, Eq. (2.58), can be substituted into Eq. (2.68) to provide:

$$k_w = \frac{A_v}{A_h} \tag{2.69}$$

The Preston equation is [Preston, 1927]:

$$\frac{dh}{dt} = k_p p v \tag{2.70}$$

where k_p is the Preston constant, p is the pressure applied to the coating by the particle, v is the velocity of the particle, h is the thickness of the coating removed and t is time. Eq. (2.70) can be simplified to:

$$\frac{dh}{dS} = k_p p \tag{2.71}$$

Eq. (2.71) can be further simplified by using the projected area in the horizontal direction:

$$\frac{V}{S} = k_p P \tag{2.72}$$

Therefore, the Preston constant may be defined as:

$$k_p = \frac{V}{PS} \tag{2.73}$$

By combining, Eqs. (2.68), (2.69) and (2.73), the following relation between the wear coefficient and the Preston constant is obtained:

$$k_p = \frac{k_w}{H_c} = \left(\frac{A_v}{A_h}\right)\frac{1}{H_c} \tag{2.74}$$

Finally, by combining Eqs. (2.60), (2.66) and (2.74), the Preston constant can be explicitly written as:

$$k_p = \frac{k_w}{H_c} = \frac{2}{\pi}\frac{R^2}{a_c^2}\left[\sin^{-1}\left(\frac{a_c}{R}\right) - \frac{a_c}{R}\right]\frac{1}{H_c} \tag{2.75}$$

2.9 Summary

In this chapter, single-particle contact models are developed. First, elastic contact between a rigid, spherical particle and a homogeneous coating is analyzed in order to determine the lower-bound, yield load. This load determines the transition from elastic to plastic deformation. The yield load is the minimum load per particle necessary for scratching to initiate on a coating. The elastic analysis is also used to determine the yield load for composite coatings. Second, fully-plastic analysis is used to determine the upper-bound load per particle for scratching. This model is used to relate the width and depth of a scratch to the normal load per particle. The analysis is conducted for both homogenous and composite coatings. Third, the theory for calculating the coefficient of friction for thin film coatings is developed. Finally, the theory for determining the Preston constant of material coatings is presented.

Nomenclature

A_v, A_h = vertical and horizontal projected area (m^2)
a = radius of elastic contact circle (m)
a_c = contact semi-width in a coating (m)
$a_{Y,c}$ = contact semi-width in a coating at yield (m)
E^* = effective Young's modulus (N/m^2)
E_1, E_2 = Young's modulus of spheres (N/m^2)
$E_{Al_2O_3}$ = Young's modulus of Al_2O_3 (N/m^2)
E_{Cu} = Young's modulus of Cu (N/m^2)
E_c = Young's modulus of a coating (N/m^2)
E_d = Young's modulus of low-k dielectric (N/m^2)
E_{eff} = effective Young's modulus of a composite structure (N/m^2)
$E_{parallel}$ = Young's modulus of a parallel composite structure (N/m^2)
$E_{perpendicular}$ = Young's modulus of a perpendicular composite structure (N/m^2)
F = tangential force on a particle (N)
H_{Cu} = hardness of Cu (N/m^2)
H_c = hardness of a coating (N/m^2)
H_d = hardness of a low-k dielectric (N/m^2)
H_{eff} = effective hardness of a composite structure (N/m^2)
h = thickness of coating to be removed (m)
h_o = height of composite structure (m)
k = yield strength in shear (N/m^2)
k_p = Preston constant (m^2/N)
k_w = wear coefficient
P = normal load per particle (N)
P_{UB} = upper-bound load per particle (N)
$P_{Y,c}$ = yield load per particle on a coating (N)
p = pressure (N/m^2)
p_o = maximum pressure (N/m^2)
$p_{o,Y}$ = maximum pressure at yield (N/m^2)
R = radius of a particle (m)

R^* = effective radius (m)

R_1, R_2 = radius of spheres (m)

S = lateral distance traveled by a particle (m)

t = time (s)

x, y, z = Cartesian coordinates

V = volume (m^3)

v = velocity of a particle (m/s)

w = Cu interconnect linewidth (m)

δ = approach of distant points in elastic contact (m)

δ_c = depth of indentation into a coating (m)

$\delta_{Y,c}$ = depth of indentation into a coating at yield (m)

ε_Y = yield strain

λ = pitch of Cu interconnect lines (m)

μ = coefficient of friction

μ_{ad} = adhesion component of the coefficient of friction

μ_p = plowing component of the coefficient of friction

ν_1, ν_2 = Poisson's ratios

$\nu_{Al_2O_3}$ = Poisson's ratio of Al_2O_3

ν_c = Poisson's ratio of a coating

ν_{eff} = effective Poisson's ratio

θ = angle of contact with respect to z-axis

$\sigma_1, \sigma_2, \sigma_3$ = principal stresses (N/m^2)

σ_Y = yield strength (N/m^2)

$\sigma_{r,\max}$ = maximum tensile strength (N/m^2)

$\tau_{\max}$ = maximum shear stress (N/m^2)

$\tau_{\max,Y}$ = maximum shear stress at yield (N/m^2)

CHAPTER 3

MULTI-PARTICLE CONTACT MECHANICS

3.1 Introduction

In Chapter 2, the lower- and upper-bounds for the load per particle in particle-coating interaction have been determined for both homogenous and composite coatings. The lower-bound load per particle denotes the transition from elastic (non-scratching) to plastic (scratching) behavior. The upper-bound load per particle is the appropriate load for analyzing scratches. The theory presented in Chapter 2, however, has some limitations. Specifically, the equations relate the observable width and depth of a scratch to the load per particle, P. Equations in this form are useful only if single-particle contact is of interest and the load per particle is known. In the CMP process, however, there are millions of particles in contact with the pad and the coating at any time and the individual load per particle is not known a priori. Therefore, it is necessary to relate the observable scratch widths and depths to global, controllable parameters in CMP: the nominal pressure applied to the back of the pad, p, and the volume fraction of abrasive particles in the slurry, v_f.

Figure 3.1 illustrates the different pad-particle-coating mechanical interactions modeled in this chapter. For all these models, the following key assumptions are made:

- The pad is semi-infinite, homogenous and isotropic.
- The coating is semi-infinite, homogeneous and isotropic.
- The particles are uniformly distributed, rigid, uniform in size and spherical [Miyoshi and Nakagawa, 2005].

3.2 Particle Spacing and Density

The particle spacing and density is determined based on the known volume fraction of solids in the slurry. It may be noted that the particle spacing is calculated before the pad-particle-coating interface is loaded. Therefore, it is assumed that the pad-coating contact neither disturbs

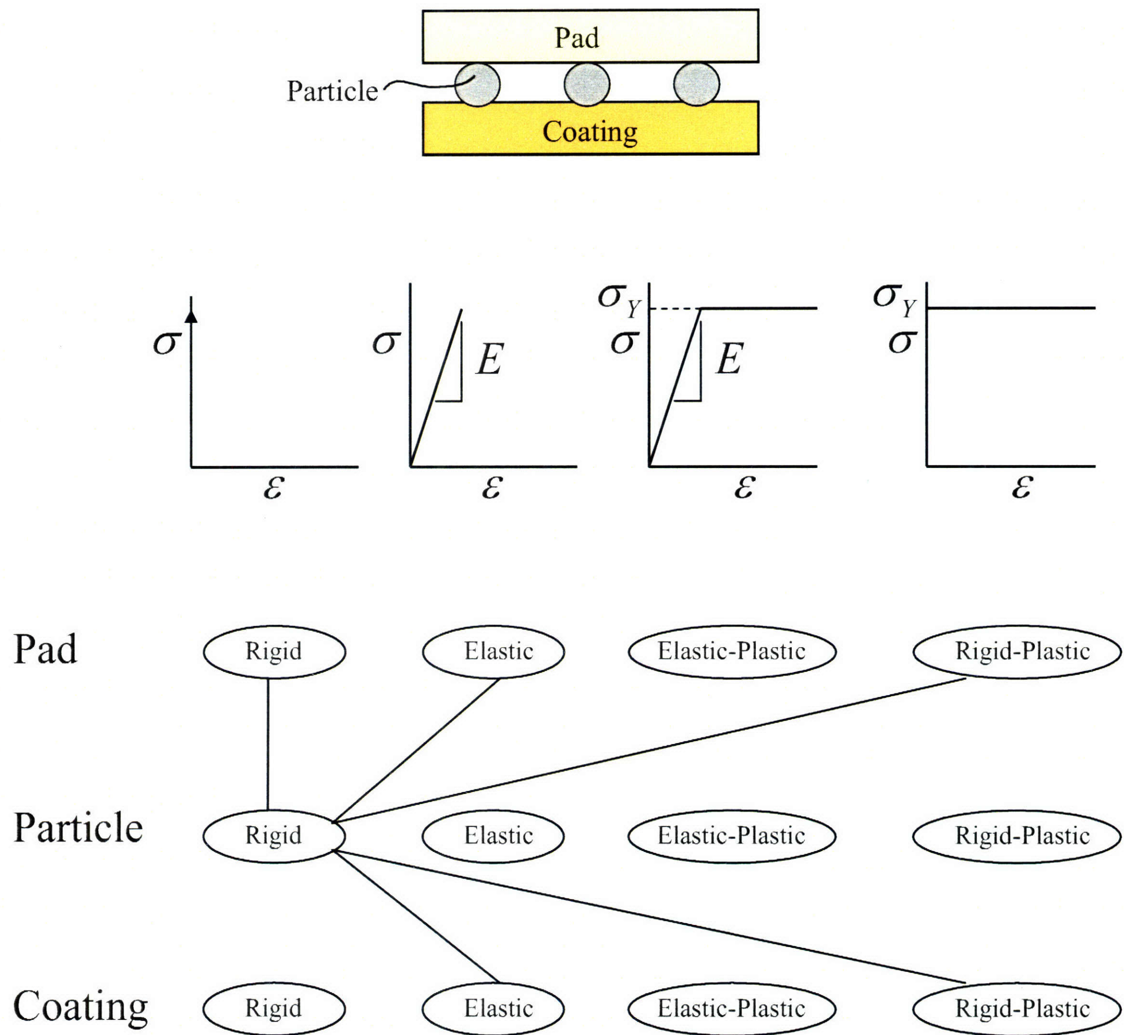

Figure 3.1: Idealized pad-particle-coating mechanical interactions in CMP.

nor interferes with the particle spacing. Wherever the pad contacts the wafer, it is assumed that the volume fraction in the contact region is exactly the same as the volume fraction in the slurry.

The volume fraction of solids in the contact region, v_f, is defined as:

$$v_f = \frac{\frac{4}{3}\pi R^3}{2R\lambda_P^{\ 2}} \tag{3.1}$$

where R is the radius of each particle and λ_P is the space between particles. The numerator represents the volume occupied by one particle and the denominator represents the volume of the unit cell around the particle occupied by liquid. As can be seen in Figure 3.2, the particle locations are assumed to fill up a square grid. In addition, it is assumed that all the particles are of uniform radius. Eq. (3.1) can be rewritten to solve for the inter-particle spacing as:

$$\lambda_P = \left[\frac{2\pi}{3v_f}\right]^{1/2} R \tag{3.2}$$

In dimensionless form:

$$\frac{\lambda_P}{R} = \left[\frac{2\pi}{3v_f}\right]^{1/2} \tag{3.3}$$

In this form, it is clear to see how far apart the particles are in relation to the radius of the particles. Another useful metric is the number of particles per unit contact area, N_A:

$$N_A = \frac{1}{\lambda_P^{\ 2}} = \frac{3v_f}{2\pi}\frac{1}{R^2} \tag{3.4}$$

A sample calculation assuming particle radius, R, of 100 nm and a volume fraction, v_f, of 0.05 shows that λ_P is 647 nm and there are 2.39 million particles per mm^2. Figure 3.2 shows schematically the case where R is 100 nm and v_f is 0.05. Typical asperity size, spacing and contact area have been added to give a sense of proportion.

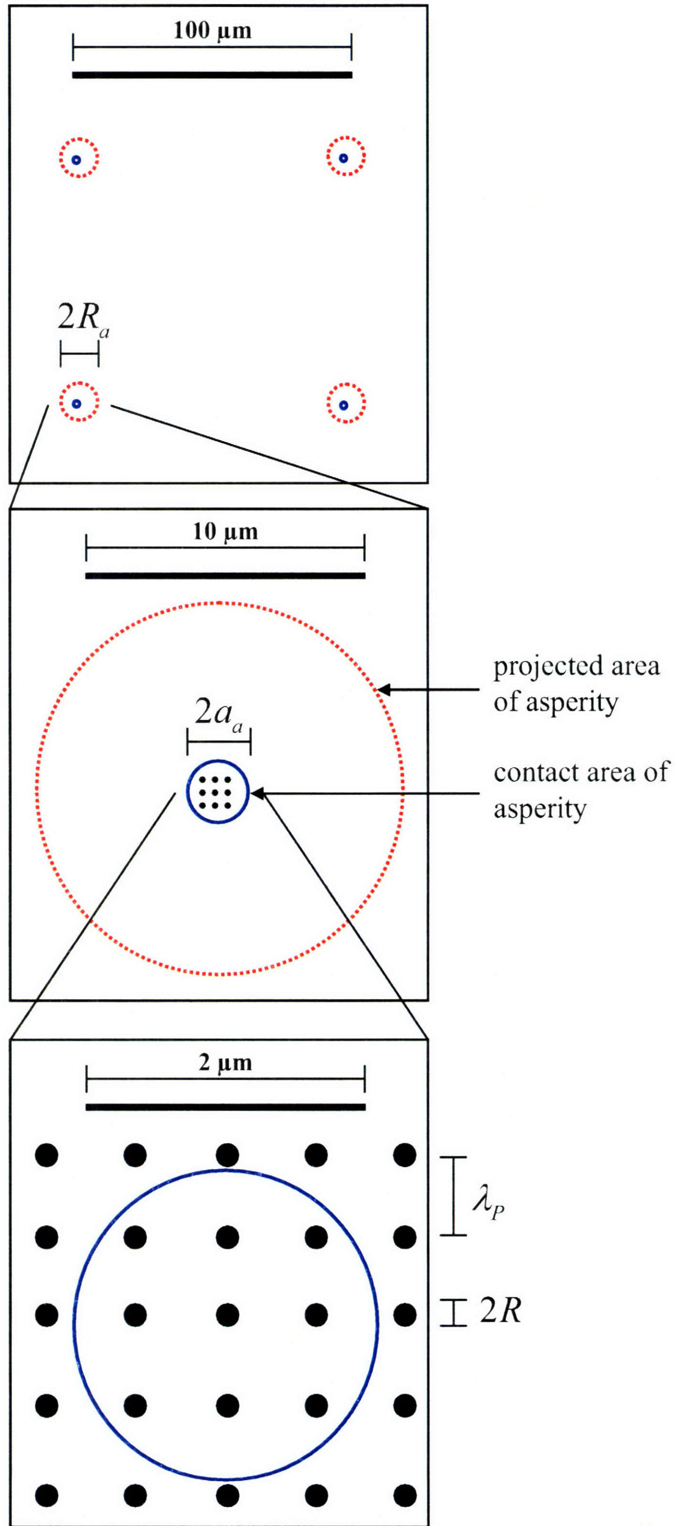

Figure 3.2: Schematic showing particle size and spacing for R = 100 nm, v_f = 0.05, asperity radius, R_a = 6 µm, asperity spacing, λ_a = 100 µm, and asperity contact area radius, a_a = 1 µm.

3.3 Smooth, Rigid Pad

The rigid, or very hard, pad analysis though unrealistic is an appropriate starting point because it considers the extreme case when pad deformation is negligibly small; all deformation takes place in the coating. In addition, it is assumed that the pad is smooth (i.e., there are no asperities present on the pad). Therefore, this is the closest case to the single-particle contact described in Chapter 2. The difference here is that multiple particles are present, as opposed to just one particle, and uniform pressure is applied to the back of the pad as opposed to applying a load directly on an individual particle. Figure 3.3 shows a schematic of a rigid pad in contact with particles which in turn are in contact with a coating.

3.3.1 Load per Particle

In this type of contact, the load per particle is given by:

$$P = p\lambda_P^2 \tag{3.5}$$

The load per particle is pressure times the square area that surrounds each particle. From Eq. (3.2) and Eq. (3.5):

$$P = \frac{2\pi}{3v_f} pR^2 \tag{3.6}$$

Thus the load per particle is a function of the particle size, volume fraction of solids in the slurry and the global pressure applied to the back of the pad. Neither the pad nor the coating material and geometric properties enter into consideration in determining the load per particle. The load per particle given in Eq. (3.6) represents the load applied to the particle from either the pad or the coating side.

3.3.2 Particle-Coating Contact

The coating on the wafer is assumed to exhibit rigid-plastic behavior. Therefore, the upper-bound analysis of Chapter 2 is used to model the widths and depths of particle scratches. Figure 3.4 shows a schematic of a particle in plastic contact with a coating. The semi-width of particle penetration into the coating, a_c, determined in Chapter 2, is given by:

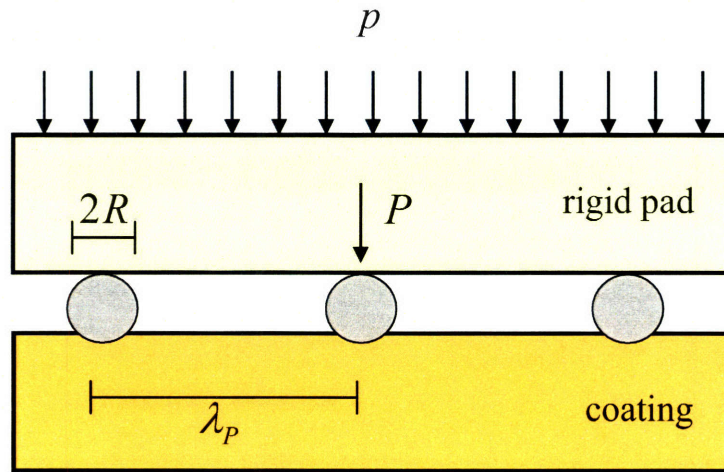

Figure 3.3: Schematic of a smooth, rigid pad in contact with multiple particles.

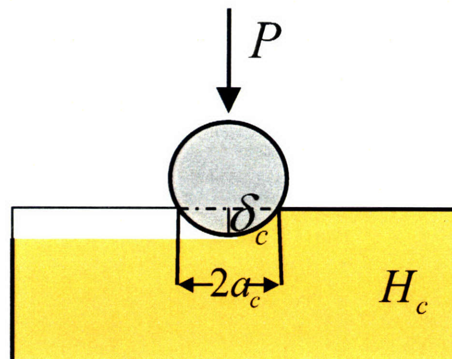

Figure 3.4: Schematic of a hard particle in plastic contact with a soft coating.

$$a_c = \left[\frac{2P}{\pi H_c}\right]^{1/2} \tag{3.7}$$

where H_c is the hardness of the coating. Note, the numerator has a factor of 2 because the particles are not simply being indented into the surface, but are translating and scratching the surface. Therefore, the horizontal projected area is: $\pi a_c^2/2$. From Eq. (3.6) and Eq. (3.7)

$$a_c = \left[\frac{4}{3v_f}\frac{p}{H_c}\right]^{1/2} R \tag{3.8}$$

which can be rewritten in dimensionless form as:

$$\frac{a_c}{R} = \left[\frac{4}{3v_f}\frac{p}{H_c}\right]^{1/2} \tag{3.9}$$

From the geometry, the width of the scratch can be related to the depth of particle penetration into the coating, δ_c, by:

$$\frac{\delta_c}{R} = \frac{1}{2}\left(\frac{a_c}{R}\right)^2 \tag{3.10}$$

Using Eqs. (3.9) and(3.10), the depth of the scratch is given by

$$\delta_c = \frac{2}{3v_f}\frac{p}{H_c}R \tag{3.11}$$

which can be cast in dimensionless form as:

$$\frac{\delta_c}{R} = \frac{2}{3v_f}\frac{p}{H_c} \tag{3.12}$$

It may be noted that Eqs. (3.8) and (3.11) are dependent on the pressure directly, not on the load per particle explicitly. In addition, Eqs. (3.9) and (3.12) provide useful metrics for identifying the presence of scratches. If $\delta_c/R, a_c/R \ll 1$, scratching will not be observed; if $\delta_c/R \sim 1$, scratching will be observed. Table 3.1 lists the results of a sample calculation for the widths and depths of scratches on a Cu coating.

As can be seen in Table 3.1, for R = 100 nm and v_f = 0.05, and for pressures in the range 6.9-69 kPa (1-10 psi), the semi-width of a scratch on a Cu coating is about 3 nm. Therefore, the scratches that would be created under the rigid pad model are not the type of scratches that are

Table 3.1: Widths and depths of particle penetration into a Cu coating for a rigid pad. R = 100 nm, v_f = 0.05, H_c = 1.22 GPa.

p (psi)	p (kPa)	P (nN)	a_c (nm)	δ_c (x10^{-3} nm)	a_c/R (x10^{-3})	δ_c/R (x10^{-6})	δ_c/λ_P (x10^{-6})
1	6.9	2.9	1.2	7.5	12	75	12
2	13.8	5.8	1.7	15.1	17	151	23
3	20.7	8.7	2.1	22.6	21	226	35
4	27.6	11.6	2.5	30.1	25	301	47
5	34.5	14.4	2.7	37.7	27	377	58
6	41.4	17.3	3.0	45.2	30	452	70
7	48.3	20.2	3.2	52.7	32	527	81
8	55.2	23.1	3.5	60.3	35	603	93
9	62.1	26.0	3.7	67.8	37	678	105
10	68.9	28.9	3.9	75.4	39	754	116

problems for the CMP industry. If a 100-nm particle creates a "scratch" that is approximately 6 nm wide, then that is not true "scratching." Furthermore, it may be noted that for R = 100 nm and v_f = 0.05, the pressure should be 6,000 psi for the particle to be embedded half-way into the coating (i.e., $a_c = R$). This is an unrealistically large pressure. However, it should also be noted that for R = 25 nm and v_f = 0.01, the pressure exerted on the pad would be only 207 kPa (30 psi) for the particle to be embedded half-way into the coating. This is still five times larger than the maximum practical pressure used in CMP. Therefore, in the rigid pad analysis, it is unrealistic that any scratch will be created such that $a_c = R$

An important check to make is that the coating is in fact in the plastic range. The yield load per particle for a homogenous coating is given by Eq. 2.30 in Chapter 2:

$$P_{Y,c} = \frac{\pi^3}{48} \frac{H_c^3}{E_c^2} R^2 \tag{3.13}$$

This can be related to the yield pressure for the coating, $p_{Y,c}$, by using Eq. (3.6):

$$p_{Y,c} = \frac{\pi^2}{32} \frac{H_c^3 v_f}{E_c^2} \tag{3.14}$$

If the applied pressure is greater than $p_{Y,c}$, the coating deforms plastically. For the sample calculation, where v_f = 0.05, H_c = 1.22 GPa and E_c = 128.0 GPa, the yield pressure for a Cu coating is 0.25 psi. Therefore, Table 3.1 is appropriate for the entire range of pressures listed (i.e., 1-10 psi), and the upper-bound analysis is justified. The scratch semi-width at yield can be obtained by substituting Eq. (3.14) into Eq. (3.9):

$$\frac{a_{Y,c}}{R} = \left[\frac{\pi^2}{24} \frac{H_c^2}{E_c^2} \right]^{1/2} \tag{3.15}$$

and $a_{Y,c}/R$ is 0.006. The depth at yield can be obtained by substituting Eq. (3.14) into Eq. (3.12):

$$\frac{\delta_{Y,c}}{R} = \frac{\pi^2}{48} \frac{H_c^2}{E_c^2} \tag{3.16}$$

and $\delta_{Y,c}/R$ is about 0.00002.

3.4 Smooth, Elastic Pad

For this analysis, the pad is assumed to be planar and very smooth, similar to the coating. In addition, it is assumed that the smooth pad deforms only elastically.

3.4.1 Load per Particle

The first approach to modeling the smooth pad-particle-coating contact is to divide the types of contact into two separate regimes. As shown in Figure 3.5 there are two distinct regimes of smooth pad-particle-coating contact.

In Regime 1, Figure 3.5(a), the pad makes contact only with the particles, which in turn make contact with the coating. At the transition from Regime 1 to Regime 2, Figure 3.5(b), the pressure on the back of the pad is so great that the pad deforms to the point where it not only makes contact with the particles, which in turn contact the coating, but the pad just touches the coating. Some published research has attempted to implement beam-bending theory to determine this transition point [Fu *et al.*, 2001]. In Regime 2, Figure 3.5(c), the pressure on the back of the pad is so great that the pad severely deforms around the particles and makes contact with both the particles and the coating directly. In order to study the worst case of particle scratching in CMP, Regime 1 is the appropriate regime to analyze, for in Regime 2, the load is shared by the particles and by the wafer. In this situation, the particles will not experience the greatest load per particle. Of course, in the extreme case where a very large pressure is applied to the back of the pad, it is possible for the load per particle in Regime 2 to exceed the load per particle in Regime 1. In that case, however, the pad will have completely engulfed the particle and therefore the scratch depths that will be capable of being produced are very small because most of the particle is embedded in the pad and hence will not be able to indent the coating.

In addition, Regime 2 will almost certainly occur once the pad has entered the plastic regime. In that case, the elastic analysis presented here is not valid. Therefore, as far as practically analyzing scratching for an elastic, smooth pad, the particle will experience the greatest load per particle at the transition from Regime 1 to Regime 2. In Regime 1, the load per particle is given by Eq. (3.6), which is equal to the load per particle in the smooth, rigid pad analysis. Elastic analysis of the pad-particle contact is not necessary. The reason for this is that in Regime 1, the

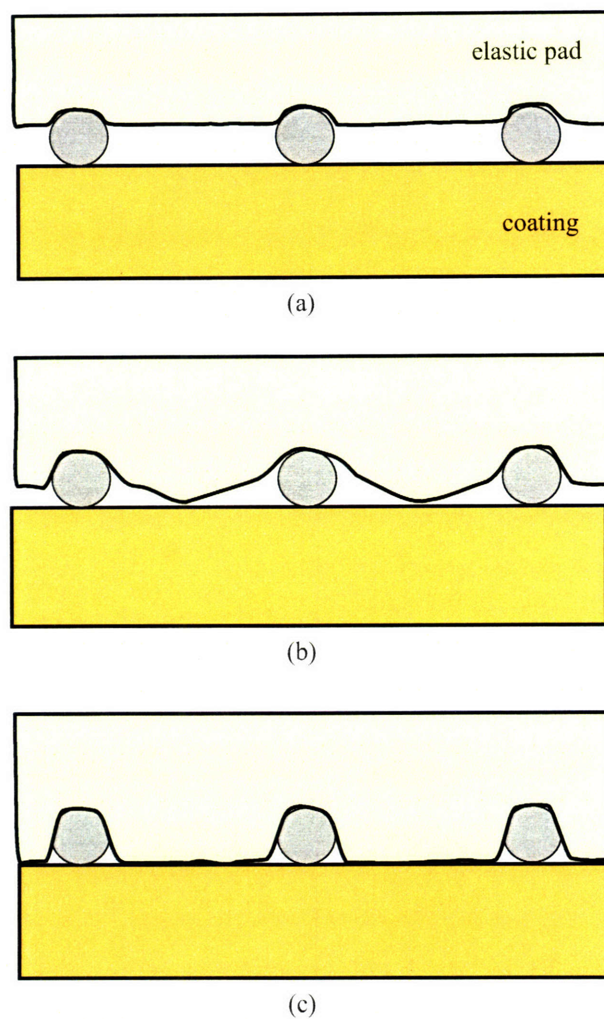

Figure 3.5: Schematic of a smooth, elastic pad in contact with particles and a coating in: (a) Regime 1 where the pad does not touch the coating (b) the transition point where the pad just touches the coating (c) Regime 2 where the pad makes contact with the particles and the coating.

pad is not touching the coating directly, so the load per particle is still equal to the pressure times the square cell area surrounding a particle. Figure 3.6 shows a schematic of this contact.

Once again, it is important to note that under the smooth, elastic pad assumption, the load per particle is still expressed as a function of the particle size, R, the given volume fraction in the slurry, v_f, and the global pressure applied to the back of the pad, p; neither the elastic nor geometric properties of the pad need to be taken into account to determine the load per particle.

3.4.2 Particle-Pad Contact

The load per particle given by Eq. (3.6) represents the load applied to the particle either from the pad or the coating side, due to the equilibrium condition. Figure 3.7 shows a schematic of a particle contacting the pad.

If the pad is assumed to exhibit elastic behavior, the Hertzian analysis can be used to model the width and depth of penetration of the particle into the pad. The radius of particle contact area with the pad, a_p, and depth of particle penetration into the pad, δ_p, is given by:

$$\frac{a_p^{\,2}}{R} = \delta_p = \left[\frac{9}{16}\frac{P^2}{RE_p^{\,2}}\right]^{1/3} \tag{3.17}$$

where E_p is the Young's modulus of the pad. Eq. (3.6) can be substituted into Eq. (3.17) to provide a simplified, dimensionless expression for the radius of the contact area in the pad:

$$\frac{a_p}{R} = \left(\frac{\pi}{2v_f}\right)^{1/3}\left(\frac{p}{E_p}\right)^{1/3} \tag{3.18}$$

Likewise, the depth of particle penetration into the pad:

$$\frac{\delta_p}{R} = \left(\frac{\pi}{2v_f}\right)^{2/3}\left(\frac{p}{E_p}\right)^{2/3} \tag{3.19}$$

Note that the load per particle is not explicitly present in Eqs. (3.18) and (3.19). Instead, the width and depth of particle penetration into the smooth, elastic pad is related directly to the global pressure. Eq. (3.19) provides an expression for a rough check to ensure that Regime 1 is indeed the appropriate choice. If $\delta_p/R \ll 1$, the pad does not make direct contact with the coating and thus Regime 1 was the appropriate choice. This however is only approximate because it is possible that the pad deforms in between two particles if they are widely apart. This

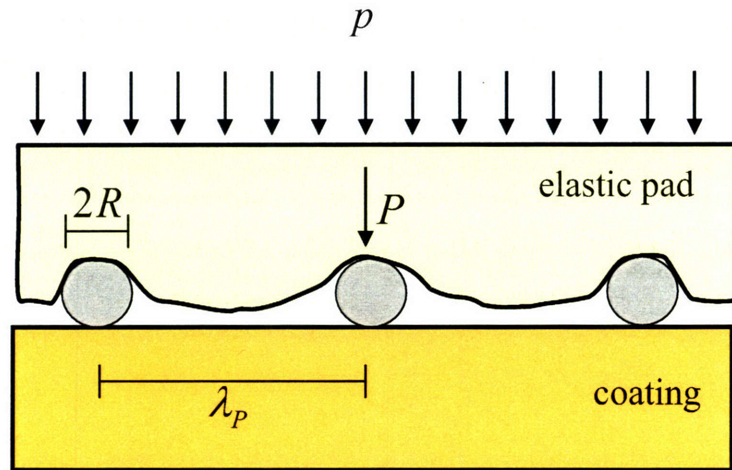

Figure 3.6: Schematic of a smooth pad in contact with particles, which are in contact with the coating (Regime 1).

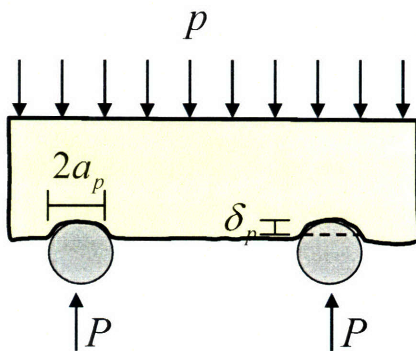

Figure 3.7: Schematic of a hard particle in contact with a smooth, elastic pad.

deformation is not captured by the Hertzian analysis, because this analysis only considers the local deformation near the point of contact between the pad and the particle. Nevertheless, it is an approximate check that can be used. Table 3.2 provides the values of a sample calculation for the depth and width of particle penetration into the pad.

As can be seen in Table 3.2, for R = 100 nm, a typical value used in standard CMP slurries, over the range of typical pressures, 6.9-69 kPa (1-10 psi), the depth of particle penetration into the pad, δ_p, is of the order of 1 nm. Therefore, the contact does in fact remain in Regime 1 because the pad does not come close to touching the coating.

An important check on the above calculations is to make sure that the deformation is still in the elastic regime. An expression for determining the yield load for the pad, $P_{Y,p}$, is very similar to Eq. 2.30 in Chapter 2 for the yield load of a homogenous coating. The only difference in this case is that the pad, as opposed to the coating, is yielding. Therefore the yield load is given as:

$$P_{Y,p} = \frac{\pi^3}{48} \frac{H_p^{\,3} R^2}{E_p^{\,2}} \tag{3.20}$$

where H_p is the hardness of the pad. Once the load per particle is greater than $P_{Y,p}$, the deformation is in the plastic regime and the elastic analysis is no longer valid. The ratio of Eq. (3.13) to Eq. (3.20) can be used to determine whether the coating or the pad will yield first:

$$\frac{P_{Y,c}}{P_{Y,p}} = \left(\frac{H_c}{H_p}\right)^3 \left(\frac{E_p}{E_c}\right)^2 \tag{3.21}$$

For typical values of a Cu coating and a Rohm and Haas IC1000 pad, E_c = 128.0 GPa, H_c = 1.22 GPa, E_p = 0.5 GPa, and H_p = 0.05 GPa, the ratio in Eq. (3.21) is 0.22. This implies that the coating yields before the pad. Therefore, while the pad deforms elastically, the coating will start to deform plastically.

The yield point of the pad can also be defined in terms of pressure, $p_{Y,p}$, by substituting Eq. (3.20) into Eq. (3.6):

$$p_{Y,p} = \frac{\pi^2}{32} \frac{H_p^{\,3} v_f}{E_p^{\,2}} \tag{3.22}$$

Table 3.2: Widths and depths of particle penetration into a smooth, elastic pad. R = 100 nm, $\nu_f = 0.05$, $E_p = 0.5$ GPa.

p (psi)	p (kPa)	P (nN)	a_p (nm)	δ_p (nm)	a_p/R	δ_p/R (x10^{-3})	δ_p/λ_P (x10^{-3})
1	6.9	2.9	7.6	0.6	0.08	5.7	0.9
2	13.8	5.8	9.5	0.9	0.10	9.1	1.4
3	20.7	8.7	10.9	1.2	0.11	11.9	1.8
4	27.6	11.6	12.0	1.4	0.12	14.4	2.2
5	34.5	14.4	12.9	1.7	0.13	16.7	2.6
6	41.4	17.3	13.7	1.9	0.14	18.9	2.9
7	48.3	20.2	14.5	2.1	0.14	21.0	3.2
8	55.2	23.1	15.1	2.3	0.15	22.9	3.5
9	62.1	26.0	15.7	2.5	0.16	24.8	3.8
10	68.9	28.9	16.3	2.7	0.16	26.6	4.1

Notice that the yield pressure is only dependent upon the volume fraction of the slurry, the hardness of the pad and Young's modulus of the pad. For the sample calculation performed above where R = 100 nm, v_f = 0.05, E_p = 0.5 GPa, and H_p = 0.05 GPa, the yield pressure is approximately 7.6 kPa (1.1 psi). Therefore, in Table 3.2, only the first row of numbers is truly valid. Once the pressure is greater than 7.6 kPa (1.1 psi), the pad deforms plastically. In Section 3.3.2 it was determined that the Cu coating will start to yield at 1.7 kPa (0.25 psi) whereas the pad will start to yield at 7.6 kPa (1.1 psi). Therefore, scratching will start to occur on the coating surface while the pad is still in the elastic regime. This is interesting because it shows that there exists a range of pressures, such that plastic deformation occurs in the coating, but the pad deforms in the elastic regime. This means that it is possible to remove material, i.e. polish the coating, without wearing out the pad. By polishing in this regime, it would be possible to increase the life expectancy of a pad. A limitation of course is that the material removal rate of the coating will be small due to the low polishing pressure. Eq. (3.22) can also be rewritten in terms of particle size and particle spacing by using Eq. (3.1):

$$p_{Y,p} = \frac{\pi^3}{48} \frac{R^2 H_p^{\;3}}{\lambda_p^{\;2} E_p^{\;2}} \tag{3.23}$$

Eq. (3.22) can substituted into Eq. (3.18) to obtain an expression for the radius of the area of indentation at the yield point:

$$\frac{a_{Y,p}}{R} = \frac{\pi}{4} \frac{H_p}{E_p} \tag{3.24}$$

For the sample calculation, $a_{Y,p}/R$ is approximately 0.08.

Eq. (3.20) can be substituted into Eq. (3.17) to provide an expression for the depth of indentation into the pad at the yield point:

$$\frac{\delta_{Y,p}}{R} = \frac{\pi^2}{16} \frac{H_p^{\;2}}{E_p^{\;2}} \tag{3.25}$$

For the sample calculation, this is about 0.62 nm. Therefore, once the particle has been pushed into the pad 0.62 nm, the pad starts to deform plastically. This is also consistent with Table 3.2, in that the value for δ_p at 6.9 kPa (1 psi) is about 0.6 nm.

3.4.3 Particle-Coating Contact

The coating on the wafer is once again assumed to exhibit rigid-plastic behavior. Therefore, the upper-bound analysis from Chapter 2 is used to model the width and depth of scratches into the surface of the coating. Therefore, Eqs. (3.8) and (3.11) are appropriate for determining the semi-width and depth of particle scratching in the coating. Because these expressions are dependent on the pressure, volume fraction, coating hardness and particle radius, the values for the semi-width and depth of particle scratching will be the same in the smooth, rigid pad analysis and the smooth, elastic pad analysis. The reason for this is that the expressions in Eqs. (3.8) and (3.11) do not depend upon the pad properties at all. Therefore, so far as the smooth pad is not directly touching the coating, it does not matter what type of deformation the pad experiences. For a sample calculation, where R = 100 nm, $v_f = 0.05$, H_c = 1.22 GPa, the table of a_c and δ_c will be the same as Table 3.1. Nevertheless, for completeness, it is presented again. Therefore, Table 3.3 provides the values of a sample calculation for the depth and width of particle scratches on a homogeneous Cu coating for a smooth elastic pad. Note that even though this table only considers particle-coating contact, for all pressures above 7.6 kPa (1.1 psi), the pad will deform in the plastic regime.

As can be seen in Table 3.3, for R = 100 nm, over the range of typical pressures, p = 6.9-69 kPa (1-10 psi), the semi-width of a scratch, a_c, on a Cu coating is of the order of 3 nm. Therefore, the scratches that would be created under the linear-elastic, smooth pad model are not the type of scratches that are problems for the CMP industry. If a 100-nm particle creates a "scratch" that is approximately 6 nm wide, that is not true "scratching." Therefore, the linear-elastic, smooth pad model does not account for scratches that are observed in CMP practice. In addition, the linear-elastic assumption is not valid for pressures above those given by Eq. (3.22), which in this case is about 7.6 kPa (1.1 psi). Accordingly, a rough pad analysis is required.

Table 3.3: Widths and depths of particle penetration into a Cu coating. R = 100 nm, v_f = 0.05, H_c = 1.22 GPa.

p (psi)	p (kPa)	P (nN)	a_c (nm)	δ_c (x10^{-3} nm)	a_c/R (x10^{-3})	δ_c/R (x10^{-6})	δ_c/λ_P (x10^{-6})
1	6.9	2.9	1.2	7.5	12	75	12
2	13.8	5.8	1.7	15.1	17	151	23
3	20.7	8.7	2.1	22.6	21	226	35
4	27.6	11.6	2.5	30.1	25	301	47
5	34.5	14.4	2.7	37.7	27	377	58
6	41.4	17.3	3.0	45.2	30	452	70
7	48.3	20.2	3.2	52.7	32	527	81
8	55.2	23.1	3.5	60.3	35	603	93
9	62.1	26.0	3.7	67.8	37	678	105
10	68.9	28.9	3.9	75.4	39	754	116

3.5 Rough Pad – Hemi-Spherical Asperities

For the rough pad analysis, it is assumed that the pad has asperities and they are hemi-spherical in shape. Figure 3.8 shows a schematic of the rough pad interacting with particles and a coating surface.

For this analysis, it is first assumed that the pad asperities deform elastically and later that the pad asperities deform plastically. Figure 3.9 shows magnified schematics of the two regimes of deformation. Figure 3.9(a) shows a pad asperity deforming elastically and Figure 3.9(b) shows an entire asperity deforming plastically. Section 3.5.2 analyzes the case where the asperity deforms elastically and Section 3.5.5 analyzes the case where the asperity deforms plastically. However, before analyzing the type of asperity deformation, it is first necessary to analyze the particle-asperity spacing.

3.5.1 Load per Particle

The first step in modeling the pad-particle-coating contact with a rough pad is to divide the types of particle-asperity spacing into two separate regimes. As can be seen in Figure 3.10, there are two distinct regimes of particle-asperity spacing. In Regime 1, the distance between each particle, λ_p, is less than the distance between each asperity, λ_a: $\lambda_p < \lambda_a$. In other words, there are more particles than asperities present at the pad-coating interface. In Regime 2, the distance between particles is greater than the distance between asperities: $\lambda_p > \lambda_a$. This means that there are now more asperities present than particles at the pad-coating interface, which implies that some asperities will not trap particles. The appropriate choice of regimes is once again Regime 1, for it is not realistic to have more asperities than particles.

Using Eq. (3.2), even with a relatively small volume fraction of 0.01 and a particle radius of 100 nm, the distance between each particle is about 1.5 μm, whereas on a typical Rohm and Hass IC1000 pad, the asperities are about 100 μm apart. Figures 3.11 and 3.12 show two micrographs of the Rohm and Haas IC1000 pad. These micrographs were obtained using an Olympus LEXT Confocal Microscope. As can be seen in Figure 3.11, the surface of the pad is quite porous. The distance between "peaks" is about 100 μm. In addition, Figure 3.12 shows a profile of the pad surface and from that, the average radius of an asperity is approximately 5 μm. Thus, Regime 1

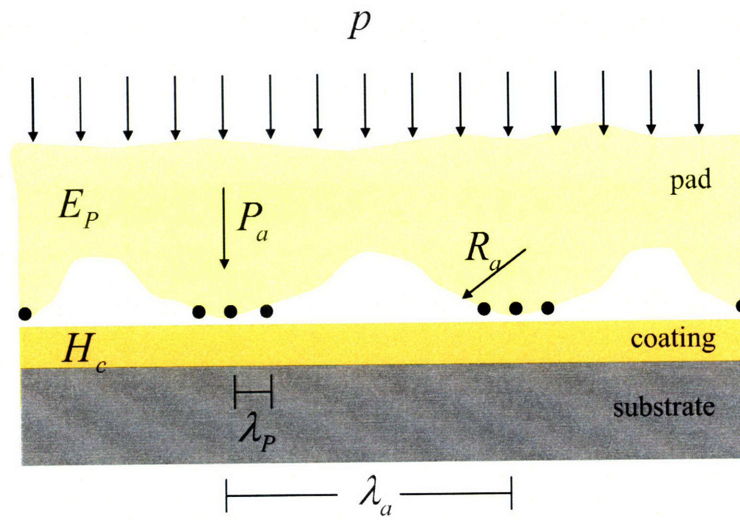

Figure 3.8: Schematic of a rough pad in contact with particles.

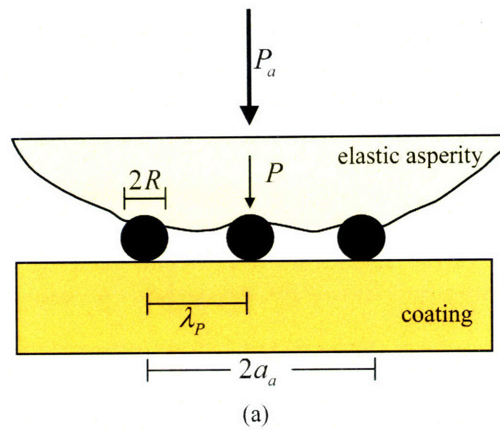

(a)

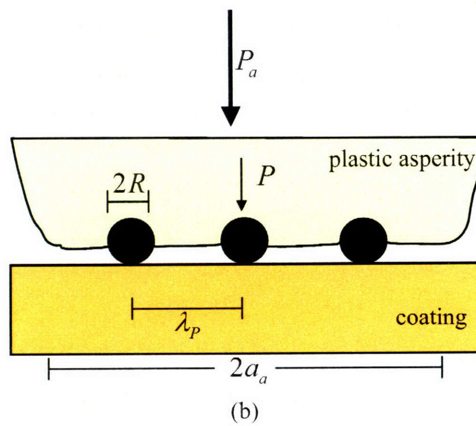

(b)

Figure 3.9: A magnified schematic of an asperity deforming (a) elastically and (b) plastically.

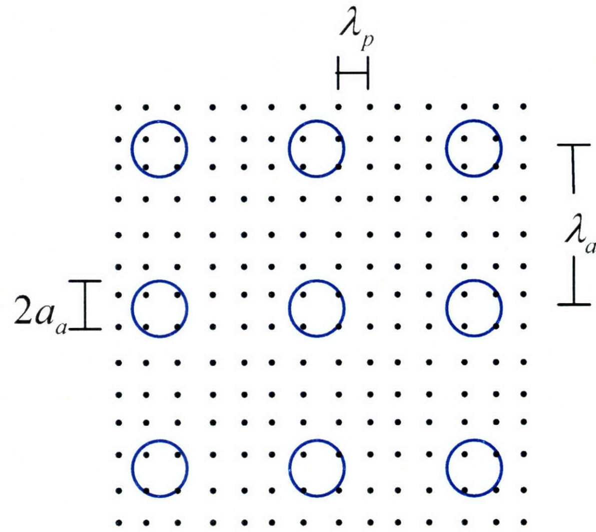

(a)

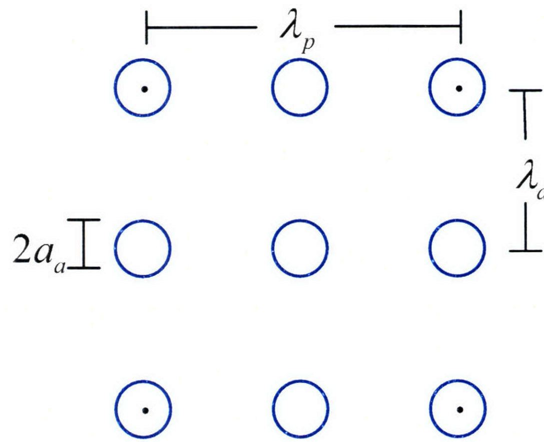

(b)

Figure 3.10: Schematic of particle-asperity spacing: (a) Regime 1, where $\lambda_P < \lambda_a$ and there is at least one particle under each asperity (b) Regime 2, where $\lambda_P > \lambda_a$ and it is not guaranteed that there is at least one particle under each asperity.

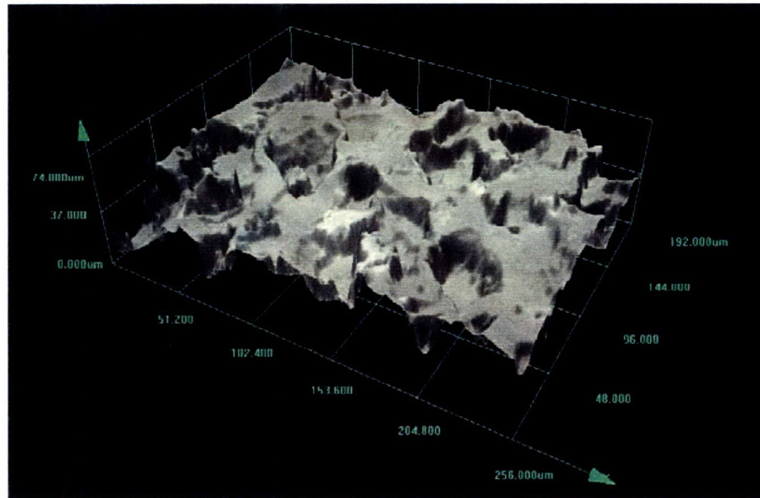

Figure 3.11: 3D image of a Rohm and Haas IC1000 pad obtained with an Olympus LEXT Confocal Microscope.

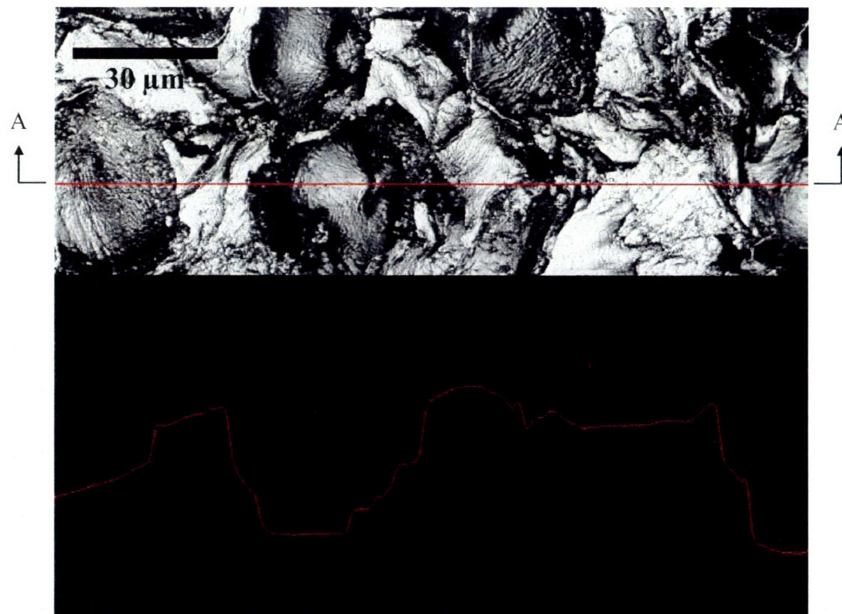

Figure 3.12: Image of a Rohm and Haas IC1000 pad and profile of section A-A obtained with an Olympus LEXT Confocal Microscope.

is the appropriate choice.

The load per particle in Regime 1 is given by:

$$Pn_P = p\lambda_a^2 = P_a \tag{3.26}$$

where n_P is the number of particles underneath one asperity and P_a is the load on an asperity. Eq. (3.26) is derived from a force balance between the load applied to one asperity and the load applied to particles underneath that asperity. An expression for the number of particles underneath one asperity can be given as:

$$n_P = \frac{3}{2}\frac{a_a^2}{R^2}v_f \tag{3.27}$$

where a_a is the radius of the contact area between one asperity and the coating-particle interface as shown in Figure 3.9. Therefore, Eqs. (3.1), (3.26) and (3.27) can be combined to provide a simplified equation for the load per particle:

$$P = \frac{p\lambda_a^2\lambda_P^2}{\pi a_a^2} \tag{3.28}$$

Notice, this is the load per particle and it is written in terms of the pressure, particle spacing, asperity spacing and contact area of the asperity. So far, only geometrical relations have been used. Therefore, this equation is valid even when the asperity is in the elastic or plastic regime. In order to eliminate the radius of the asperity contact area from Eq. (3.28), either elastic or plastic deformation must be analyzed.

3.5.2 Elastic Analysis of an Asperity

Hertzian analysis is used to develop an expression for the contact area of the asperity during elastic deformation. Applying elastic analysis to the asperity, the radius of contact is given as:

$$\frac{a_a^2}{R_a} = \left[\frac{9}{16}\frac{P_a^2}{R_a E_p^2}\right]^{1/3} \tag{3.29}$$

where R_a is the radius of curvature of an asperity [Che *et. al*, 2005]. Eq. (3.26) can be substituted into Eq. (3.29) to give:

$$a_a^2 = \left(\frac{9}{16}\right)^{1/3}\left[\frac{R_a p\lambda_a^2}{E_p}\right]^{2/3} \tag{3.30}$$

The above expression relates the contact area of the asperity to the radius of curvature of the asperity, the pressure, the asperity spacing and the Young's modulus of the pad. This can be substituted into Eq. (3.28) to obtain explicitly the load per particle:

$$P = \frac{1}{\pi}\left(\frac{4}{3}\right)^{2/3}\left(\frac{E_p}{p}\right)^{2/3}\left(\frac{\lambda_a}{R_a}\right)^{2/3} p\lambda_p^{\,2} \tag{3.31}$$

It may be noted that in Eq. (3.31), the load per particle depends on all known, global parameters: the Young's modulus of the pad, the pressure applied to the pad, the spacing between particles, the spacing between asperities and the radius of curvature of the asperities. Another significant observation is that this expression for the load per particle is different from the smooth pad analysis in that this load per particle also depends on the elastic properties and topography of the pad. Eq. (3.31) can be rewritten such that it depends upon the volume fraction and particle radius by substituting Eq. (3.2) in to Eq. (3.31):

$$P = \left(\frac{128}{243}\right)^{1/3}\left(\frac{E_p}{p}\right)^{2/3}\left(\frac{\lambda_a}{R_a}\right)^{2/3}\left(\frac{p}{v_f}\right)R^2 \tag{3.32}$$

This is the load per particle, assuming that the asperity deforms elastically. Therefore, it is necessary to determine the point at which the asperity deformation transitions into the plastic regime. An expression for the yield load of the asperity, $P_{Y,a}$, can be obtained by using Eq. 2.30 in Chapter 2:

$$P_{Y,a} = \frac{\pi^3}{48}\frac{H_p^{\,3}}{E_p^{\,2}}R_a^{\,2} \tag{3.33}$$

Using Eq. (3.26), the yield condition can be written in terms of pressure:

$$p_{Y,a} = \frac{\pi^3}{48}\frac{R_a^{\,2}H_p^{\,3}}{\lambda_a^{\,2}E_p^{\,2}} \tag{3.34}$$

When the pressure is less than that given by Eq. (3.34), the elastic analysis of the asperity is valid. For typical values of: R_a = 5 µm, λ_a = 100 µm, E_p = 0.5 GPa and H_p = 0.05 GPa, the pressure at which the asperity yields is 0.83 kPa (0.12 psi). Therefore, most likely, the asperity deformation will be in the plastic regime. However, it is possible that while polishing some of the asperities are deformed elastically. Therefore, the elastic analysis of pad asperities is carried through.

The radius of the asperity contact area at yield, $a_{Y,a}$, can be obtained from Eq. (2.31) in Chapter 2 to provide:

$$a_{Y,a} = \frac{\pi}{4}\frac{H_p}{E_p}R_a \tag{3.35}$$

The number of particles under an asperity at yield, $n_{Y,P}$, is determined using Eqs. (3.1), (3.27) and (3.35):

$$n_{Y,P} = \frac{\pi^3}{16}\frac{H_p^2}{E_p^2}\frac{R_a^2}{\lambda_P^2} \tag{3.36}$$

3.5.3 Particle-Pad Contact: Elastic Contact

Once an expression for the load per particle has been established in the case of elastic deformation of the asperity, Eq. (3.31), it is necessary to analyze the particle-pad contact. Because it is assumed that the pad deforms elastically, Hertzian, elastic analysis can be used to model the depth and width of penetration of the particle into the pad. The width of particle penetration into the pad and depth of particle penetration into the pad is given by Eq. (3.17) for the smooth, elastic pad analysis in Section 3.4. By substituting the load per particle in Eq. (3.31) into Eq. (3.17), a dimensionless expression for the width of particle penetration into the pad is given as:

$$\frac{a_P}{R} = \left(\frac{3}{4\pi^3}\right)^{1/9}\left(\frac{p}{E_p}\right)^{1/9}\left(\frac{\lambda_P}{R}\right)^{2/3}\left(\frac{\lambda_a}{R_a}\right)^{2/9} \tag{3.37}$$

In addition, a dimensionless expression for the depth of particle penetration into the pad is given as:

$$\frac{\delta_P}{R} = \left(\frac{3}{4\pi^3}\right)^{2/9}\left(\frac{p}{E_p}\right)^{2/9}\left(\frac{\lambda_P}{R}\right)^{4/3}\left(\frac{\lambda_a}{R_a}\right)^{4/9} \tag{3.38}$$

Eq. (3.38) provides an expression for a necessary check on the pad-coating interface. If $\delta_p/R \ll 1$, the pad does not touch the wafer – as in Section 3.4. A sample calculation for R = 100 nm is shown in Table 3.4.

It can be seen that $\delta_p/R \sim 1$, which means that the pad does in fact deform such that it touches the wafer. To a certain extent this should be expected. When the Hertzian analysis is

Table 3.4: Widths and depths of particle penetration into a rough, elastic pad. R = 100 nm, v_f = 0.05, E_p = 0.5 GPa, R_a = 5 μm, λ_a = 100 μm.

p (psi)	p (kPa)	P (μN)	a_p(nm)	δ_p (nm)	a_p/R	δ_p/R	δ_p/λ_P
1	6.9	14.3	129	166	1.29	1.7	0.26
2	13.8	18.0	139	194	1.39	1.9	0.30
3	20.7	20.6	146	212	1.46	2.1	0.33
4	27.6	22.7	150	226	1.50	2.3	0.35
5	34.5	24.4	154	237	1.54	2.4	0.37
6	41.4	25.9	157	247	1.57	2.5	0.38
7	48.3	27.3	160	256	1.60	2.6	0.40
8	55.2	28.5	162	264	1.62	2.6	0.41
9	62.1	29.7	165	271	1.65	2.7	0.42
10	68.9	30.7	166	277	1.66	2.8	0.43

employed to determine the radius of the asperity contact area, the pad is forced to touch the wafer directly and then the particles were superimposed into that same space. Therefore, this theoretical approach forces the pad to touch the coating. It is the worst case scenario that is of interest, when the load is completely supported by the particles. Table 3.4 shows that under a rough, hemi-spherical pad, some of the load may in fact be supported by the coating directly. This means that in reality, the load per particle is less than what is estimated here. Therefore, from a theoretical stand point the upper-bound is calculated here, which is appropriate. Last, this model was developed assuming that only one particle is being pushed into the pad. In reality, there are numerous particles being pushed into the pad. When the contribution of the pad displacement of the other particles is considered, it only makes it more difficult for the pad to touch the wafer. And, because $\delta_p / R \sim 1$, it is almost exactly at the transition point of the pad where it just slightly starts to touch the wafer. When the effect of the other particles is taken into account, it is even less likely that the pad touches the wafer directly.

It should be noted that the values calculated in Table 3.4, assume that the asperity deformation occurs in the elastic regime. Therefore, the values in Table 3.4 are only valid for pressures less than the yield pressure given by Eq. (3.34), about 0.83 kPa (0.12 psi).

3.5.4 Particle-Coating Contact: Plastic Contact

It is assumed that the wafer coating exhibits rigid-plastic behavior. Therefore, the upper-bound analysis from Chapter 2 is used to model the width and depth of scratches in the surface of the coating and Eqs. (3.7) and (3.10) are appropriate. When Eq. (3.32) is substituted into Eqs. (3.7) and (3.10), the semi-width and depth of a scratch, in dimensionless form, is respectively given as:

$$\frac{a_c}{R} = \frac{2}{\sqrt{3\pi}} \left(\frac{4}{3}\right)^{1/3} \left(\frac{E_p}{p}\right)^{1/3} \left(\frac{p}{H_c}\right)^{1/2} \left(\frac{\lambda_a}{R_a}\right)^{1/3} \left(\frac{1}{v_f}\right)^{1/2} \tag{3.39}$$

$$\frac{\delta_c}{R} = \frac{2}{3\pi} \left(\frac{16}{9}\right)^{1/3} \left(\frac{E_p}{p}\right)^{2/3} \left(\frac{p}{H_c}\right) \left(\frac{\lambda_a}{R_a}\right)^{2/3} \left(\frac{1}{v_f}\right) \tag{3.40}$$

Eqs. (3.39) and (3.40) provide crucial expressions for the semi-width and depth of scratching. It is important to note the parameter sensitivity of the above equations. Specifically, in Eq. (3.39), the semi-width of a scratch is most strongly dependent on the radius of the slurry particles. As

the size of the slurry particles increases, the width of the scratches increase linearly. The next strongest dependence is on the volume fraction and the hardness of the coating. As the volume fraction increases, the scratch width decreases, as does material removal [Luo and Dornfeld, 2003]. The width of a scratch is inversely proportional to these and varies as the one-half power. The Young's modulus of the pad, the spacing between asperities, and the radius of curvature of the asperities have the next strongest dependence and vary as the one-third power. Interestingly, the parameter with the weakest dependence on the width of a scratch is the global polishing pressure, p, with a one-sixth power dependence. Therefore, it is evident that scratching does not have as strong a correlation with pressure as compared with particle size.

Eq. (3.39) also provides important qualitative information. It can be seen that in order to reduce the width of scratches, it is necessary to decrease the average particle radius, increase the volume fraction of solids in the slurry, increase the hardness of the coating, decrease the Young's modulus of the pad, decrease the spacing between asperities, increase the radius of curvature of the asperities and decrease the global polishing pressure.

If $\delta_c/R \sim 1$ or $a_c/R \sim 1$, then scratches will appear on the surface of the coating. A sample calculation for scratching on a homogenous Cu coating by particles with a radius of 100 nm is shown in Table 3.5. It can be seen that both δ_c/R and a_c/R are approximately 1, which means that for these general, industrial values for polishing, scratching is expected to occur. It is important to remember that the values in Table 3.5 assume that the asperity deforms elastically. However, this is only the case for small pressures below those determined by Eq. (3.34). Therefore, the next step in the modeling process is to see what happens when the asperity deforms plastically, which is a much more realistic case.

3.5.5 Plastic Analysis of Pad Asperities

Eq. (3.34) provides an expression for the pressure at which the global asperity deformation transitions from the elastic to plastic regime. For the previously used sample calculation values, the transition pressure is approximately 0.83 kPa (0.12 psi). This transition pressures is relatively low compared with the typical pressures used in CMP practice. Therefore, most of the asperities on the pad are expected to deform plastically [Luo and Dornfeld, 2003].

In that case, the upper-bound analysis developed in Chapter 2 can be used to analyze both the

Table 3.5: Widths and depths of particle penetration into a Cu coating using a rough, elastic pad. R = 100 nm, v_f = 0.05, H_c = 1.22 GPa, E_p = 0.5 GPa, R_a = 5 μm, λ_a = 100 μm.

p (psi)	p (kPa)	P (uN)	a_c (nm)	δ_c(nm)	a_c/R	δ_c/R	δ_c/λ_P
1	6.9	14.3	86.3	37.2	0.86	0.37	0.058
2	13.8	18.0	96.9	46.9	0.97	0.47	0.072
3	20.7	20.6	103.6	53.7	1.04	0.54	0.083
4	27.6	22.7	108.7	59.1	1.09	0.59	0.091
5	34.5	24.4	112.8	63.7	1.13	0.64	0.098
6	41.4	25.9	116.3	67.7	1.16	0.68	0.105
7	48.3	27.3	119.3	71.2	1.19	0.71	0.110
8	55.2	28.5	122.0	74.5	1.22	0.74	0.115
9	62.1	29.7	124.5	77.4	1.24	0.77	0.120
10	68.9	30.7	126.7	80.2	1.27	0.80	0.124

pad and coating. As shown in Figure 3.13, the load on the particle is equal in magnitude on the both the particle-pad interface and the particle-coating interface. Therefore, using the upper-bound analysis,

$$P = \pi a_p^2 H_p = \pi a_c^2 H_c \tag{3.41}$$

Eq. (3.41) can be simplified to relate the scratch width, a_c, to the width of particle penetration in the pad, a_p:

$$a_c = \sqrt{\frac{H_p}{H_c}} a_p \tag{3.42}$$

Normalizing Eq. (3.41) provides:

$$\frac{a_c}{R} = \sqrt{\frac{H_p}{H_c}} \frac{a_p}{R} \tag{3.43}$$

Similarly, the scratch depth, δ_c, can be related to the depth of particle penetration in the pad, δ_p by using Eqs. (3.10) and (3.41):

$$\frac{\delta_c}{R} = \frac{H_p}{H_c} \frac{\delta_p}{R} \tag{3.44}$$

3.6 A Criterion for Scratching

The most interesting conclusion of this analysis is that there is an upper-limit to a_p and it is R. Once the pad engulfs half of the particle, Figure 3.13(b), the next increment of pressure will in effect "collapse" the system, meaning that the pad will collapse immediately around the rest of the particle, Figure 3.13(c). After the local collapse of the pad, the pad is in direct contact with the coating and the load is no longer supported by only the particles. Therefore, even if the pressure were increased further the load per particle will not be greater than $\pi R^2 H_p$ (i.e., this maximum load occurs when $a_p = R$) according to the upper-bound analysis. This means that the scratch width is restricted to:

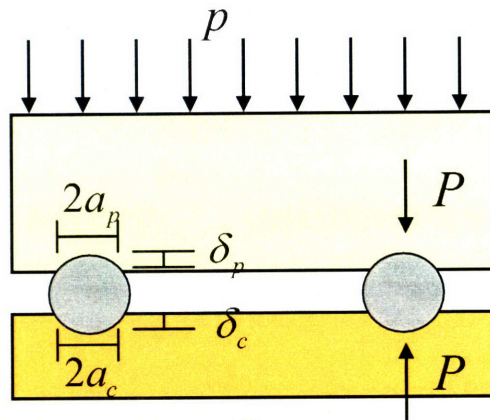

(a)

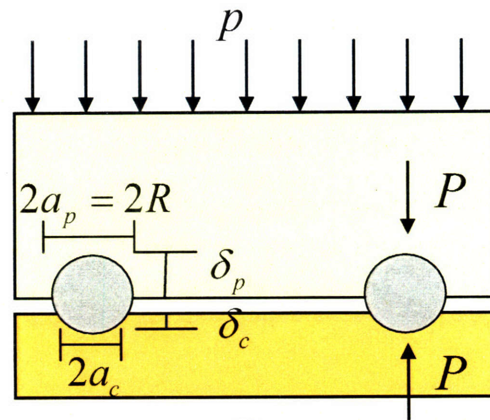

(b)

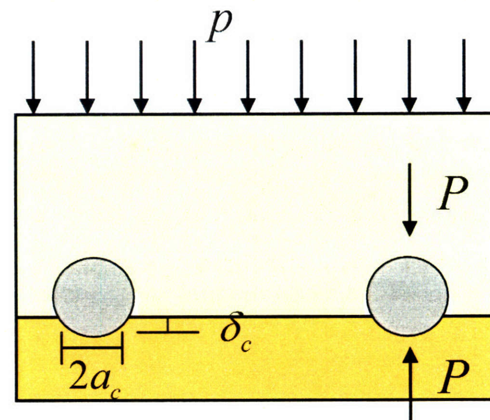

(c)

Figure 3.13: Schematic of the pad asperity and the coating deforming plastically: (a) $a_p < R$, (b) $a_p = R$, and (c) asperity collapse after $a_p = R$.

$$a_c \le \sqrt{\frac{H_p}{H_c}} R \tag{3.45}$$

In addition, when the limiting case of $a_p = R$ is reached, $\delta_p = R$. Using this limit and Eq. (3.44) the scratch depth is bounded by:

$$\delta_c \le \frac{H_p}{H_c} R \tag{3.46}$$

The bounds given by Eqs. (3.45) and (3.46) are critical because they are absolute bounds. The analysis that led to these bounds was based entirely on plastic behavior, which occurs only after the pressure is large enough to transition out of the elastic regime and into the plastic regime. Table 3.6 provides a summary of the equations for the rough pad analysis.

The first row, the elastic contact row, presents the appropriate equations when the pad asperities deform in the elastic regime. The coating-particle column has two different sets of equations because it is possible for the coating to deform elastically or plastically while the pad deforms elastically, as shown by Eq. (3.21). The transitional pressure from elastic to plastic contact for the coating is also listed. The second row presents the equations at the yield point, i.e. the transition from elastic to plastic deformation, as well as the pressure at which the transition occurs. The final row of Table 3.6 represents the limiting cases for both the pad and coating. This means that the particle cannot penetrate the pad or coating beyond the limiting case. The equations in the final row of Table 3.6 illustrate a very important point. The limiting cases for pad and coating deformation are independent of the topography of the pad. This is important because for almost all of the practical polishing pressures used during CMP, a large majority of the asperities and the coating will deform plastically. This means that the topography of the pad can be modeled as any type (or not modeled at all) because it does not affect the largest width of the scratches on the coating. Furthermore, it shows that the pad topography also does not affect plastic deformation of the pad. Therefore, if it is desired to create a pad that does not deform plastically (thereby increasing the life of the pad), changing the geometry of the pad is not going to be very effective. Eq. (3.45) suggests that the most effective way to reduce scratch size on a particular coating is to decrease the hardness of the polishing pad as well as to decrease the size of slurry particles. There is virtually nothing else that could change to decrease the severity of scratching.

Table 3.6: Summary of rough pad equations for a pad with hemi-spherical asperities.

	Pad-Particle	Coating-Particle
1. Elastic Contact	$\frac{a_p}{R}=\left(\frac{3}{4\pi^3}\right)^{1/9}\left(\frac{p}{E_p}\right)^{1/9}\left(\frac{\lambda_P}{R}\right)^{2/3}\left(\frac{\lambda_a}{R_a}\right)^{2/9}$ $\frac{\delta_p}{R}=\left(\frac{3}{4\pi^3}\right)^{2/9}\left(\frac{p}{E_p}\right)^{2/9}\left(\frac{\lambda_P}{R}\right)^{4/3}\left(\frac{\lambda_a}{R_a}\right)^{4/9}$	Coating elastic: $\frac{a_c}{R}=\left(\frac{3}{4\pi^3}\right)^{1/9}\left(\frac{E_p}{p}\right)^{2/9}\left(\frac{p}{E_c}\right)^{1/3}\left(\frac{\lambda_a}{R_a}\right)^{2/9}\left(\frac{\lambda_P}{R}\right)^{2/3}$ $\frac{\delta_c}{R}=\left(\frac{3}{4\pi^3}\right)^{2/9}\left(\frac{E_p}{p}\right)^{4/9}\left(\frac{p}{E_c}\right)^{2/3}\left(\frac{\lambda_a}{R_a}\right)^{4/9}\left(\frac{\lambda_P}{R}\right)^{4/3}$ Transition pressure: $p_{Y,c}=\frac{\pi^{12}}{3\cdot 2^{16}}\left(\frac{R}{\lambda_P}\right)^6\left(\frac{R_a}{\lambda_a}\right)^2\frac{H_c^{\,9}}{E_c^{\,6}E_p^{\,2}}$ Coating plastic: $\frac{a_c}{R}=\frac{\sqrt{2}}{\pi}\left(\frac{4}{3}\right)^{1/3}\left(\frac{E_p}{p}\right)^{1/3}\left(\frac{p}{H_c}\right)^{1/2}\left(\frac{\lambda_P}{R}\right)\left(\frac{\lambda_a}{R_a}\right)^{1/3}$ $\frac{\delta_c}{R}=\frac{1}{\pi^2}\left(\frac{16}{9}\right)^{1/3}\left(\frac{E_p}{p}\right)^{2/3}\left(\frac{p}{H_c}\right)\left(\frac{\lambda_P}{R}\right)^2\left(\frac{\lambda_a}{R_a}\right)^{2/3}$
2. Onset of Yielding	$\frac{a_{Y,a}}{R}=\frac{\pi}{4}\frac{R_a H_p}{RE_p}$ $\frac{\delta_{Y,a}}{R}=\frac{\pi^2}{16}\frac{R_a H_p^{\,2}}{RE_p^{\,2}}$ $p_{Y,a}=\frac{\pi^3}{48}\frac{R_a^{\,2}H_p^{\,3}}{\lambda_a^{\,2}E_p^{\,2}}$	$\frac{a_{Y,c}}{R}=\frac{\pi}{4}\frac{H_c}{E_c}$ $\frac{\delta_{Y,c}}{R}=\frac{\pi^2}{16}\frac{H_c^{\,2}}{E_c^{\,2}}$ $p_{Y,c}=\frac{\pi^{12}}{3\cdot 2^{16}}\left(\frac{R}{\lambda_P}\right)^6\left(\frac{R_a}{\lambda_a}\right)^2\frac{H_c^{\,9}}{E_c^{\,6}E_p^{\,2}}$
3. Limiting Case	$\frac{a_p}{R}=1$ $\frac{\delta_p}{R}=1$	$\frac{a_c}{R}=\sqrt{\frac{H_p}{H_c}}$ $\frac{\delta_c}{R}=\frac{H_p}{H_c}$

Figure 3.14 shows the values of a_c/R and a_p/R over a range of polishing pressures for a pad and a homogenous Cu coating. The hardness of the Cu coating is assumed to be: H_c = 1.22 GPa. The red line along the horizontal axis corresponds to a very elastic pad with a very low Young's modulus. In this case, the pad is so compliant that there will not be any scratching on the coating surface because the particle will only deform the pad. It is unlikely that the pad deforms elastically, given the typical polishing pressures during CMP. The straight lines in the middle of the graph correspond to the case where both the pad and the coating deform plastically. This will be the usual case, because the pressures required for the pad to deform elastically are very low (less than 0.83 kPa). The red line on the vertical axis corresponds to the case where the pad has an infinite hardness, in which case the particle will not penetrate the pad at all, but will instead only penetrate the coating. The three different lines correspond to three different pad hardnesses: 0.01, 0.05 and 0.10 GPa. This is an appropriate range for the hardness of typical CMP pads (e.g., a Rohm and Haas IC1000 pad). The normalized version of Eq. (3.42) is used to calculate the slope of the straight lines when both the pad and the coating deform plastically. For a given value of a_p/R, as the hardness of the pad increases, the penetration of the particle into the coating increases, and therefore the semi-width of a scratch increases. The limiting value for scratch semi-width, given by Eq. (3.45), is the value of a_c/R when the line intercepts the right side of the graph.

Figure 3.15 shows a schematic of particle-coating interaction versus particle-pad interaction. Specifically, the normalized semi-width of a scratch, a_c/R, is plotted versus the normalized semi-width of particle penetration into the pad, a_p/R. As can be seen in the graph, there are four regions in each of the four corners. In the lower-left corner, the pad and the coating both deform elastically. In this region, the relation between to the variables is linear and can be obtained from Eq. (3.17):

$$\frac{a_c}{R} = \left(\frac{E_p}{E_c}\right)^{1/3} \frac{a_p}{R} \tag{3.47}$$

In the upper-left corner, the pad deforms elastically, but the coating deforms plastically because

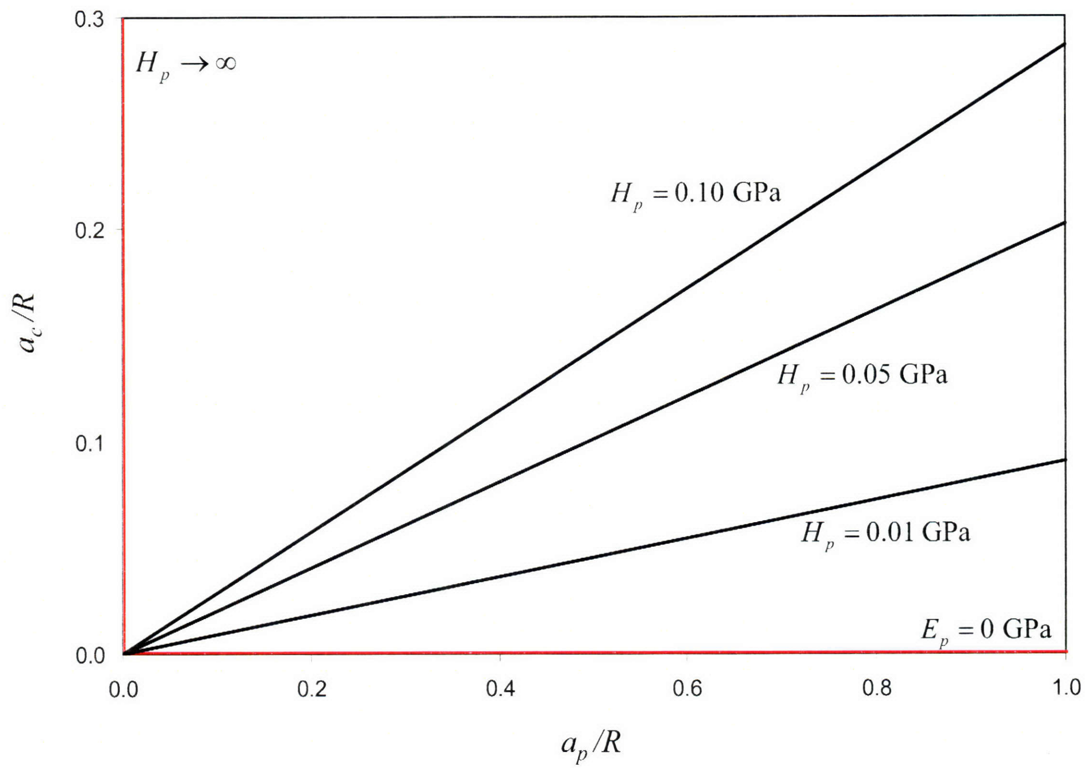

Figure 3.14: Normalized particle penetration into a plastic pad and Cu coating. H_c = 1.22 GPa.

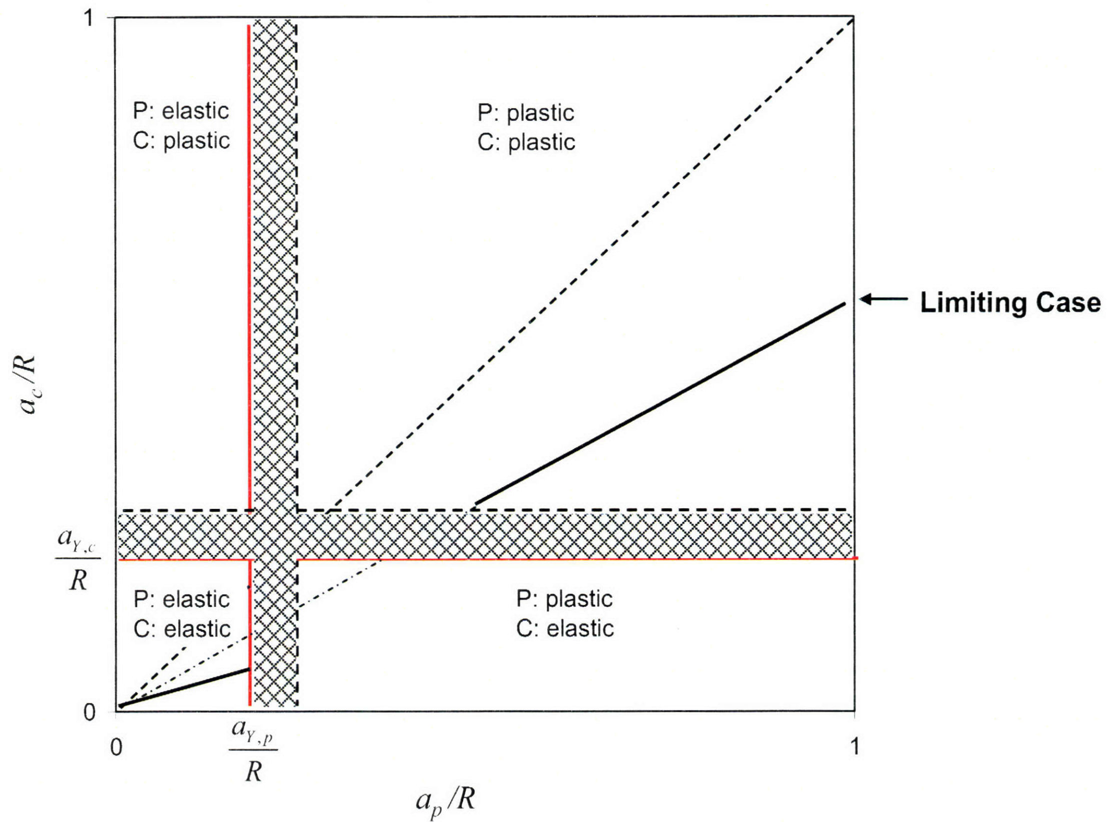

Figure 3.15: Normalized particle penetration into a coating and pad. The shaded region represents elastic-plastic transition. The four regions represent different combinations of the pad or coating deforming elastically or plastically.

the semi-scratch width is larger than $a_{Y,c}$. The shaded regions correspond to elastic-plastic transition regions. In the lower-right corner, the pad deforms plastically and the coating deforms elastically, hence there will be no scratching. Finally, in the upper-right corner, both the pad and coating deform plastically. This is the most important corner because this is the corner where scratching during CMP is present. It is in this corner that Eq. (3.43) is valid. As seen in the graph, this relation is linear and the maximum limiting value of a_c/R is given by Eq. (3.45). The dashed line represents the particle penetrating the pad and the coating the same amount for a given pressure. This would only be valid if the pad and the coating had equivalent values for hardness. However, because the pad has a lower value of hardness than any typical CMP coating, the slope of the solid line in the upper-right corner will always be less than the slope of the dashed line. This also implies that the limiting maximum scratch width will always be less than the particle radius (i.e. $a_c < R$).

If no scratching at all is desired, then in Figure 3.15, the lower-right region is the region of interest. In this region, the coating will remain elastic while the pad will be rigid-plastic. If zero scratching is desired, then the following condition must be met: at $a_p/R = 1$, $a_c/R \leq a_{Y,c}/R$. Eqs. (3.13) and (3.41) can be combined to provide:

$$\left(\frac{E_c}{H_c}\right)^2 \left(\frac{H_p}{H_c}\right) \leq 0.21 \tag{3.48}$$

Therefore, in order for zero scratching to occur, the material properties of the coating and pad must be such that the inequality in Eq. (3.48) is satisfied.

Figure 3.16 shows the normalized semi-width of a scratch on a coating, a_c/R, versus the normalized semi-width of particle indentation into the pad, a_p/R, for the case where the pad is assumed to deform plastically and for four different coatings: low-k dielectrics A and B, SiO_2 and Cu. It is assumed for this graph that the hardness of the pad is 0.05 GPa. The solid lines represent the case where the coatings deform plastically. Because both the pad and the coatings deform plastically, Eq. (3.42) is used. The horizontal dotted, red lines represent the value of a_c/R where the coatings transition from the elastic to the plastic regime, i.e., the semi-width of the scratch at yield: $a_{Y,c}/R$. Eq. 2.31 in Chapter 2 is used to obtain $a_{Y,c}/R$. The vertical dotted, red line represents the value of $a_{Y,p}/R$, where the pad transitions from elastic to plastic

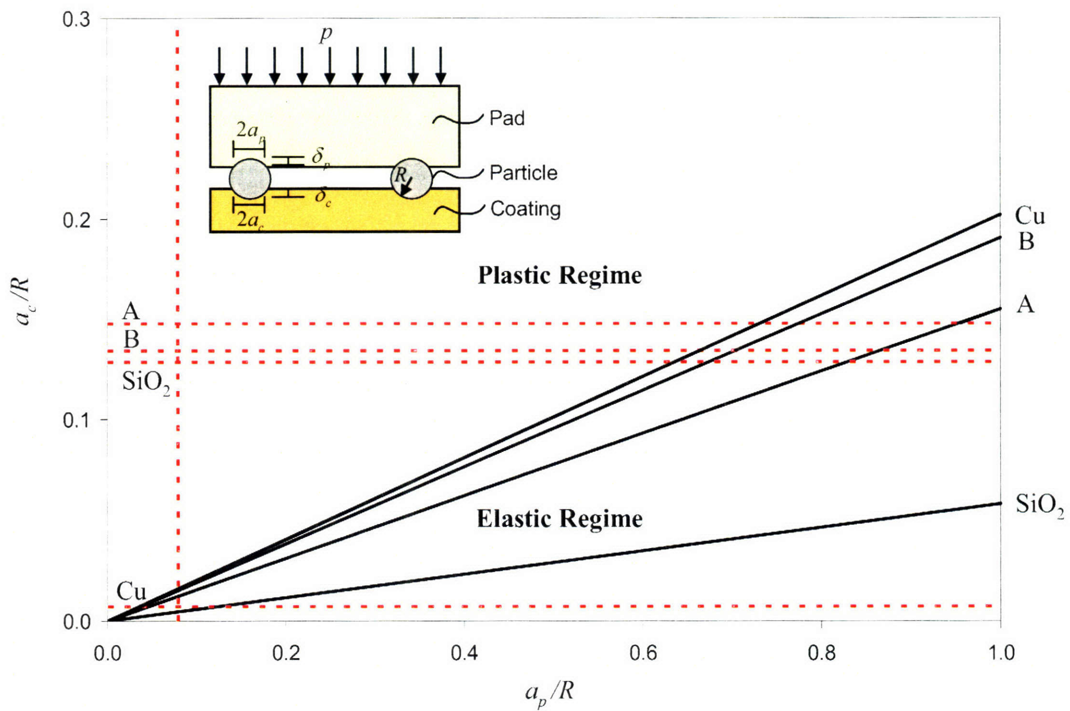

Figure 3.16: A plastic pad in contact with rigid particles, which in turn are in contact with four different coatings: low-k dielectrics A and B, SiO_2 and Cu. The solid lines represent the coatings deforming plastically and the dotted, red lines represent the transition from elastic to plastic deformation in the coatings and pad.

deformation. For a typical CMP pad, this is about 0.079.

Therefore, if $a_c/R < a_{Y,c}/R$ for a given coating, then the coating deforms elastically and scratching will not occur. For a given coating, this corresponds to the region of the graph that is below the dotted, red line. In this region, the coating does not deform plastically, and the solid line is meaningless – it is only an extrapolation of the plastic case.

If $a_c/R \sim a_{Y,c}/R$, then the coating deforms elastic-plastically and scratching may start to occur. For a given coating, this corresponds to the region of the graph slightly above the dotted, red line.

Finally, if $a_c/R \gg a_{Y,c}/R$, then the coating will deform plastically and scratching will occur. For a given coating, this corresponds to the region of the graph above the dotted, red line. In this region, the solid line appropriately represents the expected scratch semi-widths.

The following is an example of how to interpret Figure 3.16. The solid line that is labeled SiO_2 has a maximum value for a_c/R of 0.06. Therefore, if the coating is assumed to deform plastically, this is the largest dimensionless scratch size that will be present. However, the dotted, red line that is labeled SiO_2 has a value for $a_{Y,c}/R$ of 0.13. This marks the transition of the SiO_2 coating from elastic to plastic deformation. Since the solid line never crosses the dotted line, SiO_2 will never experience any scratching – all of the coating deformation will take place in the elastic regime.

The Cu coating, however, is almost the exact opposite of the previous example. The solid line that is labeled Cu has a maximum value for a_c/R of 0.20. The dotted, red line that is labeled Cu has a value for $a_{Y,c}/R$ of 0.007. The solid line crosses the dotted line at a very small value of a_c/R. Therefore, scratching on Cu is likely to occur. Scratching will occur for all values of a_c/R > 0.007. Scratches on Cu of various sizes will occur within the following bounds: $0.007 < a_c/R < 0.20$.

Similar results are obtained for the low-k dielectrics. For example, the semi-widths of scratches on a low-k dielectric B coating are bounded as: $0.13 < a_c/R < 0.19$. Similarly, the bounds for the semi-widths of scratches on low-k dielectric A can be obtained.

3.7 Summary

In this chapter, multi-particle interactions are modeled. First, the size and spacing between particles is related to the volume fraction of abrasives in the slurry. This is necessary because the spacing between particles is used to determine the load per particle and it is therefore required to relate the spacing to controllable parameters, such as particle radius and slurry volume fraction. It is first assumed that the pad is smooth and rigid. In this case, the load per particle is related to the global pressure and from that the width and depth of a scratch are related to controllable, CMP process parameters. The pressure at which yielding initiates in a Cu coating is estimated to be 1.72 kPa (0.25 psi), implying that for all practical polishing pressures the Cu coating will yield. For the rigid pad case, deformation takes place only in the coating – the pad does not deform. In order to calculate the width and depth of particle penetration into the pad, a smooth, elastic pad is modeled. This model is identical to the smooth, rigid pad case from the viewpoint of the particle-coating interactions. The smooth pad models do not adequately account for the typical size of scratches observed in CMP. Specifically, the smooth pad model predicts scratches that are very small – on the order of nanometers. As a result, a rough pad with hemi-spherical asperities is modeled. The widths and depths of scratches, assuming the pad deforms elastically, are calculated as well as the widths and depths of scratches assuming the pad deforms plastically. The transition pressure of the pad from elastic to plastic deformation is estimated to be as low as 0.83 kPa (0.12 psi), and therefore it is likely that both the pad and coating deform plastically. In the case where both the pad and coating are rigid-plastic, lower- and upper-limits on the depths and widths of scratches are defined. Finally, a criterion for scratching in CMP is established in terms of only the elastic and plastic properties of the pad and the coating, and the particle radius.

Nomenclature

a_a = radius of asperity contact area (m)
a_c = scratch semi-width in a coating (m)
a_p = radius of particle indentation into a pad (m)
$a_{Y,a}$ = radius of asperity contact area at pad yield (m)
$a_{Y,c}$ = scratch semi-width in a coating at yield (m)
$a_{Y,p}$ = radius of particle indentation into a pad at yield (m)
E_c = Young's modulus of a coating (N/m^2)
E_p = Young's modulus of a pad (N/m^2)
H_c = hardness of a coating (N/m^2)
H_p = hardness of a pad (N/m^2)
N_A = number of particle per unit area (1/m^2)
n_P = number of particle under one asperity
$n_{Y,P}$ = number of particle under one asperity at pad yield
P = normal load per particle (N)
$P_{Y,a}$ = load per particle for an asperity at yield(N)
$P_{Y,c}$ = load per particle for a coating at yield (N)
$P_{Y,p}$ = load per particle for a pad at yield (N)
P_a = normal load per asperity (N)
p = pressure (N/m^2)
$p_{Y,a}$ = yield pressure for a pad asperity (N/m^2)
$p_{Y,c}$ = yield pressure for a coating (N/m^2)
$p_{Y,a}$ = yield pressure for a pad (N/m^2)
R = radius of a particle (m)
R_a = radius of curvature of an asperity (m)
v_f = volume fraction of particles in the slurry
δ_c = depth of a scratch in a coating (m)
δ_p = depth of indentation into a pad (m)
$\delta_{Y,c}$ = depth of a scratch in a coating at yield (m)
$\delta_{Y,p}$ = depth of indentation into a pad at yield (m)
λ_a = spacing between asperities (m)
λ_P = spacing between particles (m)

CHAPTER 4

EXPERIMENTAL VALIDATION OF THE SCRATCHING MODELS

4.1 Introduction

In Chapter 2, single-particle models are developed. These models are validated by indentation and scratching experiments using a Hysitron TriboIndenter. In Chapter 3, multi-particle models are developed, which are validated by polishing experiments using a CMP tool.

4.2 Apparatus

To validate the single-particle contact models, a Hysitron TriboIndenter was used and controlled indentation and scratching tests have been conducted. The TriboIndenter is a variant of an atomic force microscope (AFM) that is capable of applying forces large enough to cause plastic deformation, as opposed to a typical AFM imaging probe, which uses relatively light forces in a tapping mode to characterize a surface. Figure 4.1 is a photograph of the outside of the TriboIndenter. The white casing surrounding the instrumentation serves to minimize acoustic interference.

Figure 4.2 is a photograph of the instrumentation located inside the casing. As shown in Figure 4.2, there are three different instruments located on the "head" of the TriboIndenter, all located above a magnetic, moving stage. The instrument in the middle is the transducer tip, where the indenting/scratching tip is located. This instrument controls the depth of indentation or scratching. The instrument located to the right is an optical sensor used to locate the region of the sample where testing is conducted. The instrument to the left is an AFM tip used for characterizing the surface of a sample after it has been indented or scratched. The instruments are fixed in the horizontal plane and thus the stage controls lateral movement. Vertical motion (in the z -direction) is controlled by the instrument head.

The coating samples were prepared by cleaving 10 mm x 10 mm squares out of 300-mm

Figure 4.1: Hysitron TriboIndenter (Source: Hysitron Inc.).

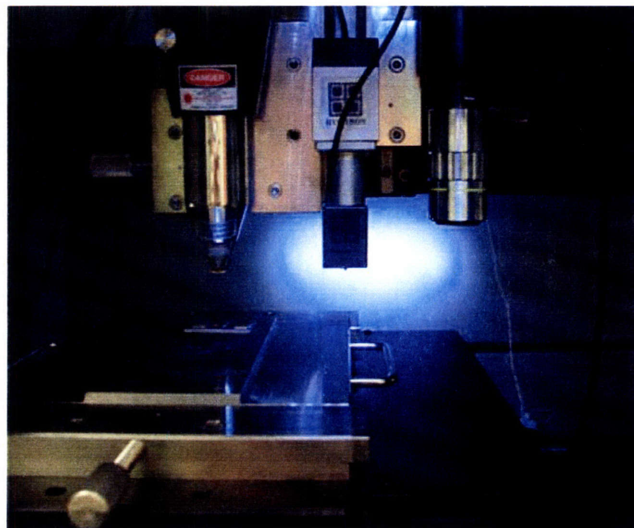

Figure 4.2: Interior view of the Hysitron TriboIndenter. The three heads from left to right are: the AFM imaging tool, the scratching/indenting instrument, and the optical head. A sample is located on the magnetic stage directly underneath the AFM imaging head.

wafers. Each sample was then glued to a 20 mm x 20 mm square piece of 1-mm thick magnetic stainless steel. The magnetic stainless steel is necessary because the samples are held in place on the stage by means of a magnetic chuck. A photograph of three different samples can be seen in Figure 4.3. The sample on the left consists of low-k dielectric B, the sample in the middle consists of Cu and the sample on the right consists of composite Cu/low-k dielectric B.

Two different types of tests were performed on the TriboIndenter: indentation tests and scratching tests. For the indentation tests, a one-dimensional transducer AFM head was used to indent and to measure the depth and force during indentation. For these tests, a Berkovich tip, composed of natural diamond, was used. The purpose of the indentation tests was to measure the hardness of the thin films and the pads. The Berkovich tip is a standard for measuring the hardnesses of bulk materials and thin films by means of nanoindentation. Figure 4.4(a) is a photograph of the Berkovich tip.

For the scratching tests, the one-dimensional transducer AFM head was removed and replaced with a two-dimensional transducer AFM instrument. The 2D transducer allows the normal load and depth to be measured and controlled, as well as the lateral load and displacement, while scratching the coating surface. The purpose of these tests was to simulate scratching by a hard, spherical particle on a coating in a controlled environment. For these tests, a cono-spherical tip, composed of natural diamond with a radius of curvature of 800 nm, was used. The cono-spherical tip was chosen over other geometrical tips (e.g., Berkovich, Vickers, cube corner, etc.) for two reasons. First, the spherical tip is a more accurate representation because the theory is based on spherical particles. Second, the cono-spherical tip is axisymmetric. This is important when scratching because it guarantees that the projected area of the tip is constant. For any other tip, the horizontal projected area can be different depending upon whether an edge of a face is facing forward while scratching. In addition, the lateral forces acting on another tip may be different depending upon whether or not a face or edge is plowing forward. Figure 4.4(b) is a photograph of the cono-spherical tip.

4.3 Indentation Experiments

The purpose of the indentation tests was to measure the hardnesses of the coatings and pad materials. The coatings tested for hardness consisted of: Cu, low-k dielectric A and low-k

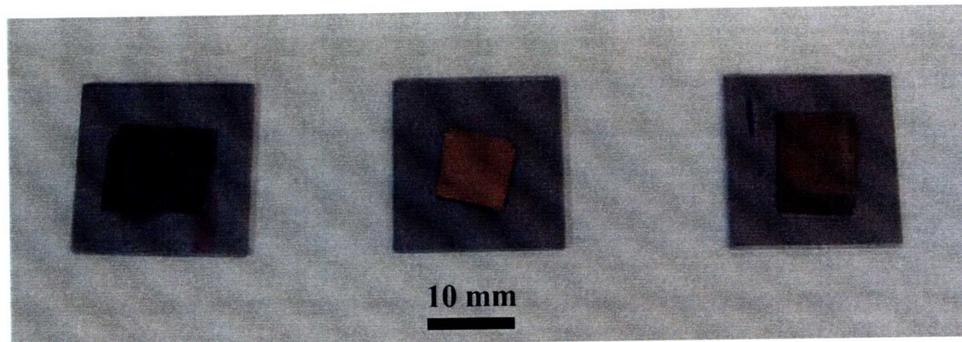

Figure 4.3: Three different samples used in the Hysitron TriboIndenter. From left to right: low-k dielectric B, Cu and composite Cu/low-k dielectric B.

(a)

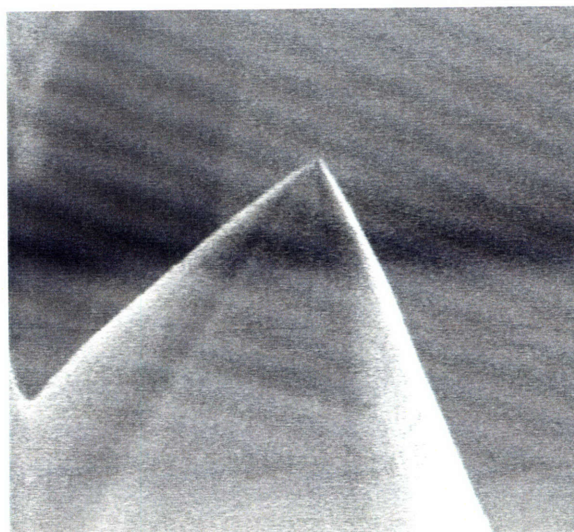

(b)

Figure 4.4: (a) Berkovich tip and (b) Cono-spherical tip (Source: Hysitron Inc.).

dielectric B. In addition, two pads were tested: the Rohm and Haas IC1000 pad and the Thomas West TWI817 pad. Furthermore, Cu samples that had been submerged in a 3% H_2O_2 aqueous solution for three different durations, 30, 60 and 300 s, were tested to observe the effect of H_2O_2 on the hardness of the Cu coating. Additionally, samples of the Rohm and Hass IC1000 and Thomas West TWI817 pads that had been immersed in water for 300 seconds were tested to measure the effect on material properties.

The low-k dielectric films were the thinnest of all the coatings, at 1 μm. Therefore, in order to observe the standard hardness testing rule of not indenting beyond 10% of the total film thickness, the TriboIndenter was set to use depth control. Specifically, each sample was indented to a maximum depth of 90 nm. Figure 4.5 shows a graph of the normal load versus normal displacement of an indentation experiment for the Cu coating.

The loading-unloading cycle seen in Figure 4.5 took 70 seconds to complete. In addition, when the maximum load was reached, the indenting tip remained at the maximum depth for 5 seconds to account for time-dependent effects, if any. This is a fairly typical elastic-plastic, loading-unloading curve. The elastic and plastic behavior can be clearly seen from the unloading portion of the curve. From Figure 4.5, most of the deformation experienced by the Cu coating was in the plastic regime, since there is very little elastic strain recovery.

Figure 4.6 shows a graph of the normal load versus normal displacement of an indentation test on the low-k dielectric A coating. Unlike the predominantly plastic behavior displayed by the Cu coating, in Figure 4.5, the low-k dielectric coating experiences almost perfectly elastic loading and unloading. There is no observable plastic deformation, for the unloading curve follows the loading curve almost exactly. Therefore, it appears that the low-k dielectrics do not experience plastic behavior for this range of indentation depths, 0-90 nm. For this reason, the hardness value given for the compliant low-k dielectrics may reflect the measurement technique more than the actual mechanical properties of the coating.

From the unloading portion of the indentation curves, the hardness and Young's modulus of each coating and pad were calculated using the Oliver-Pharr method [Oliver and Pharr, 1992]. For each sample, 36 separate indentations were made. Table 4.1 summarizes the average Young's modulus and hardness for each of the coatings and pad materials. As noted, the hardness values quoted for the low-k dielectrics may be a reflection of the Oliver-Pharr algorithm which provides hardness measurements despite the apparent lack of plastic

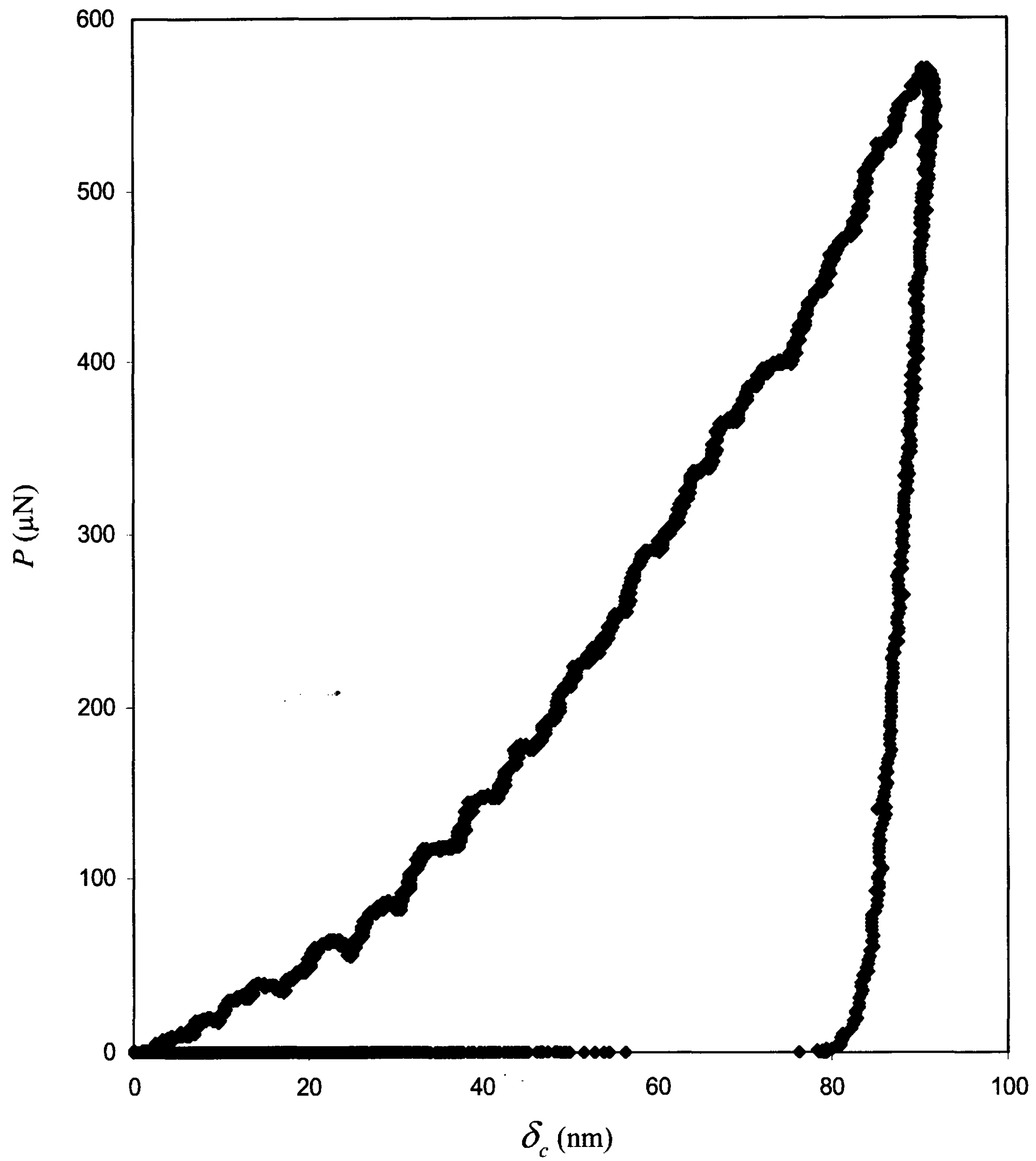

Figure 4.5: Indentation data for a Cu coating.

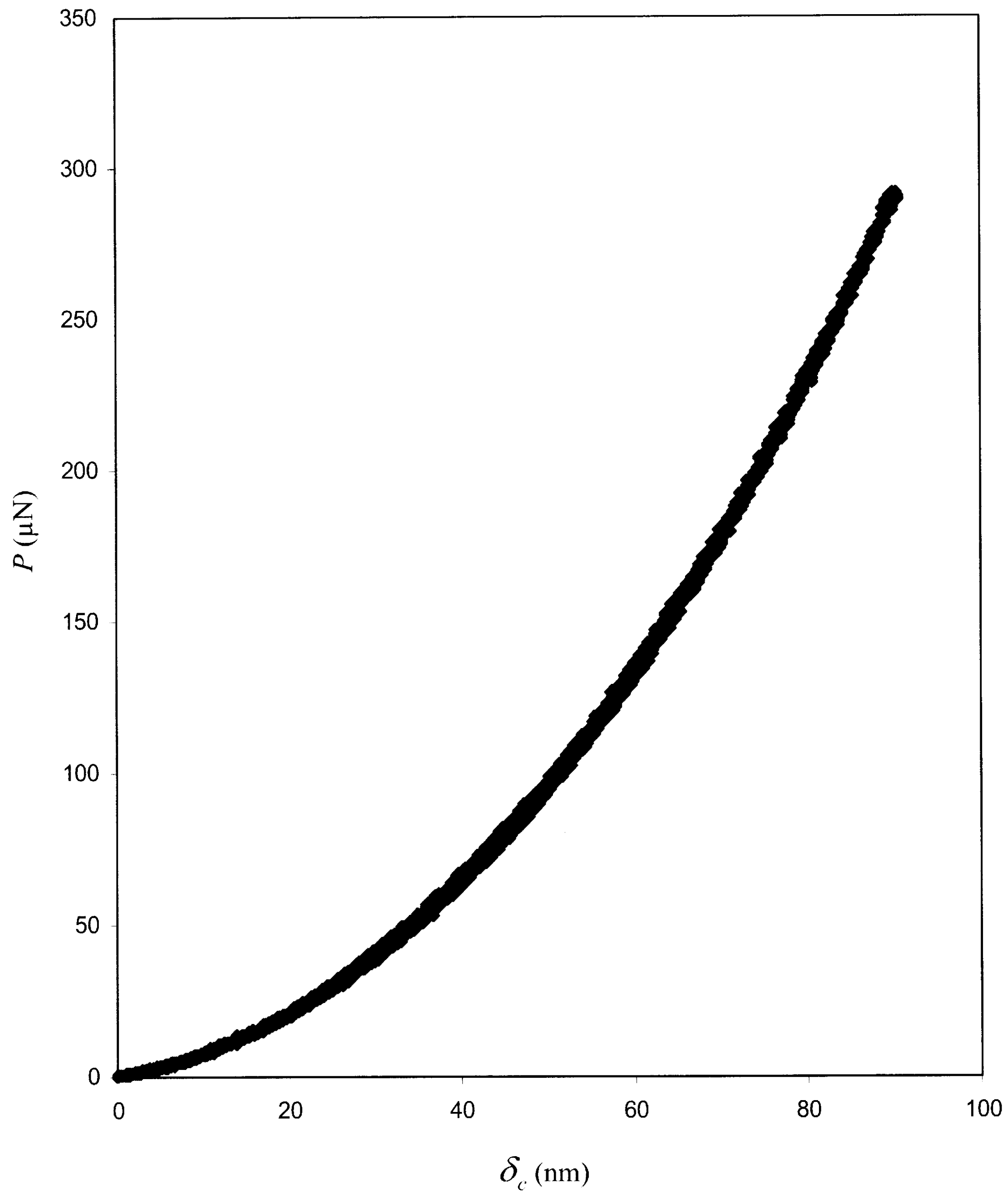

Figure 4.6: Indentation data for a low-k dielectric A coating.

Table 4.1: Young's modulus and hardness of coatings and pad materials.

Material	E (GPa)		H (GPa)	
	Avg.	Std. Dev.	Avg.	Std. Dev.
low-k A	13.20	0.15	1.81	0.04
low-k B	8.91	0.13	1.27	0.04
Cu	144.01	10.61	1.57	0.15
Cu (30 s in 3% H_2O_2)	141.92	28.66	1.91	0.51
Cu (60 s in 3% H_2O_2)	4.58	1.28	0.15	0.06
Cu (300 s in 3% H_2O_2)	6.26	3.80	0.12	0.05
Rohm and Haas pad (dry)	1.12	0.82	0.10	0.06
Rohm and Haas pad (300 s in H_2O)	0.53	0.61	0.05	0.06
Thomas West pad (dry)	0.26	0.15	0.04	0.03
Thomas West pad (300 s in H_2O)	0.30	0.16	0.06	0.05

deformation during the indentation tests.

From Table 4.1, the Young's modulus of the low-k dielectrics is an order of magnitude smaller than the modulus of Cu. However, hardnesses of the low-k dielectrics and Cu are very similar. Therefore, it is apparent that a composite coating consisting of Cu and a low-k dielectric will not have the same resistance to scratching as a composite coating that consists of Cu and silicon dioxide. In addition, the measured Young's modulus and hardness of Cu and the low-k dielectrics are very similar to the nominal values listed in Table 1.1. It can also be seen in Table 4.1, when Cu is exposed to a 3% H_2O_2 aqueous solution for 60 seconds, both its modulus and hardness drop by an order of magnitude. It appears that this "softening" of the Cu coating does not continue to decrease with time after 60 seconds. Therefore, the properties of Cu reach a steady state value at about 60 seconds of exposure to H_2O_2 solution. It may be noted that after only 30 seconds of exposure to H_2O_2, the Cu coating's properties were not significantly affected.

Another point of interest in Table 4.1 is that the Rohm and Haas IC1000 pad is approximately twice as hard as the Thomas West TWI817 pad. In addition, the Thomas West pad is more compliant than the Rohm and Haas pad, as shown by the difference in their Young's moduli. Furthermore, it appears that after being immersed in water for 300 seconds, the properties of the Thomas West pad are not significantly affected. However, after the Rohm and Haas pad was immersed in water for 300 seconds, both its hardness and Young's modulus decreased by a factor of two. It may be noted that the standard deviations of the mechanical property measurements for the pads are large in comparison to the average values. There was a large spread in the measured values of modulus and hardness for the pads because their mechanical properties substantially change at the local level. Appendix B shows the indentation data for the dry Rohm and Haas pad.

4.4 Single-Particle Contact Models: Scratching Experiments

The purpose of the scratching tests was to validate the single-particle contact models. The TriboIndenter measures the applied normal load versus the indentation depth in real-time while a scratch is being created. This is one method of verifying the lower- and upper-bound analysis of single-particle contact. It is expected that the observed experimental loads are greater than the predicted lower-bound loads and smaller than the predicted upper-bound loads. The coatings

tested include: Cu, low-k dielectric A, low-k dielectric B, SiO_2, composite Cu/low-k A and composite Cu/low-k B. In each case the scratch was 10 μm long. In addition, all the scratching tests were performed dry, i.e., there was no lubrication or liquids of any form present during scratching. For the scratch tests, load control was used as opposed to the hardness testing, where depth control was used. This means that the normal load was forced to be held constant during scratching: the normal displacement, δ_c, was varied as necessary to ensure that the normal load remained unchanged. While scratching, the depth of the scratch, δ_c, and the lateral force, F, were measured continuously. Figure 4.7 shows a typical graph of the normal load and the normal displacement as a function of time for a test on a Cu coating.

As seen in Figure 4.7, the normal load for this experiment was held constant at 400 μN as the cono-spherical tip moved laterally along the surface. The normal load does not reach the desired 400 μN value until 10 seconds into the test. In addition, at 40 seconds into the test, the 400-μN load is removed. The reason for this is that the AFM tip moves laterally along the surface of the coating only from the 10 second mark to the 40 second mark. Because the length of every scratch was fixed to be 10 μm, the velocity of this specific test was 0.33 μm/s.

For all the coatings, four different normal loads, P, were used to measure the effect on normal displacement (i.e. scratch depth). In addition, three different scratch velocities were used: 0.1 μm/s, 0.33 μm/s and 1.0 μm/s. For each set of test conditions, a minimum of 25 scratches were made. In addition, for all of the scratch tests, the radius of curvature of the cono-spherical indenter was 800 nm. Figure 4.8 shows representative SEM micrographs of controlled scratches made on the Cu coating. Figure 4.9 shows representative AFM images of controlled scratches made on the Cu coating.

Figure 4.10 shows representative scratches made on composite Cu/low-k dielectric A coating. Figure 4.11 is the AFM image of a controlled scratch made on the composite Cu/low-k dielectric B coating. Table 4.2 summarizes the experimental data on six different coatings: four homogenous coatings and two composite coatings. An important point to note from the table is that the depth of the scratch, δ_c, is not significantly dependent on the scratch velocity, v. In other words, the plastic deformation of the coatings is not rate-dependent in the velocity range used in the tests. Additionally, for some of the data in Table 4.2, the deformation is elastic and the upper-bound analysis is not compared with these points.

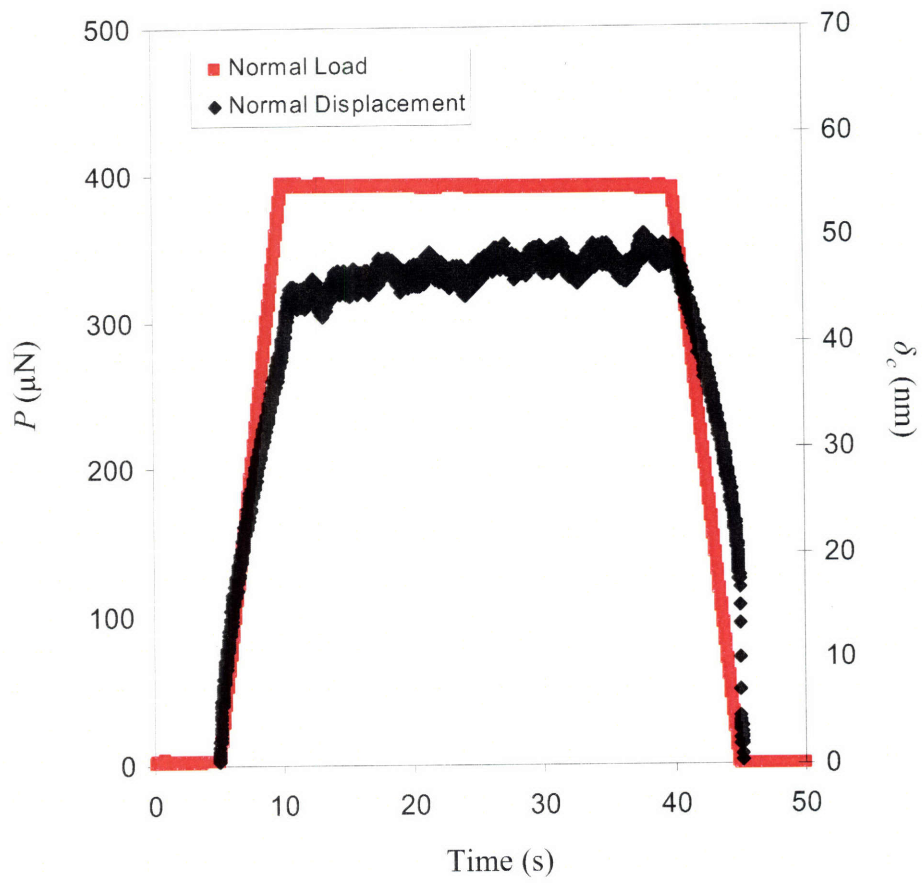

Figure 4.7: Normal load and normal displacement during a scratch test on Cu.

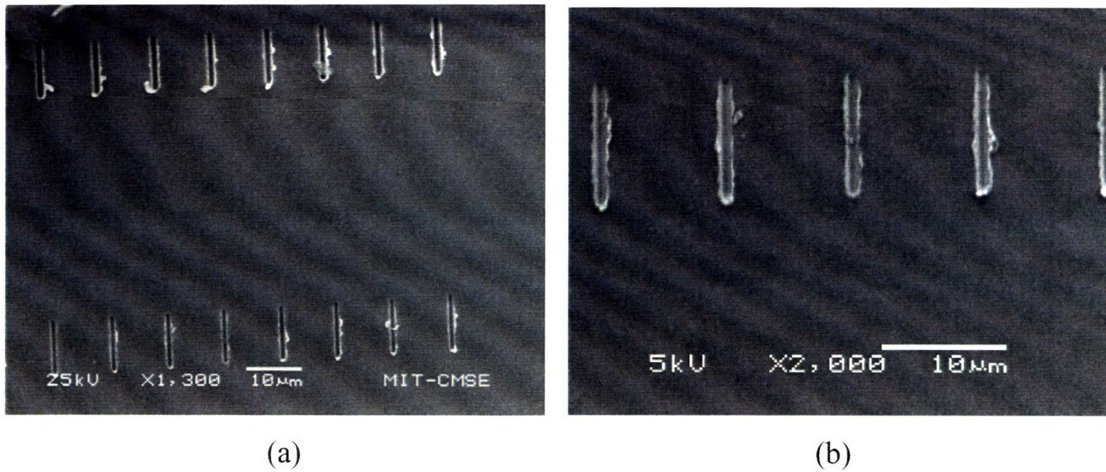

(a) (b)

Figure 4.8: SEM micrographs of scratches made on a Cu coating at (a) P = 392 µN (top row) and P = 277 µN (bottom row), and v = 0.33 µm/s, (b) P = 277 µN and v = 0.33 µm/s (magnified).

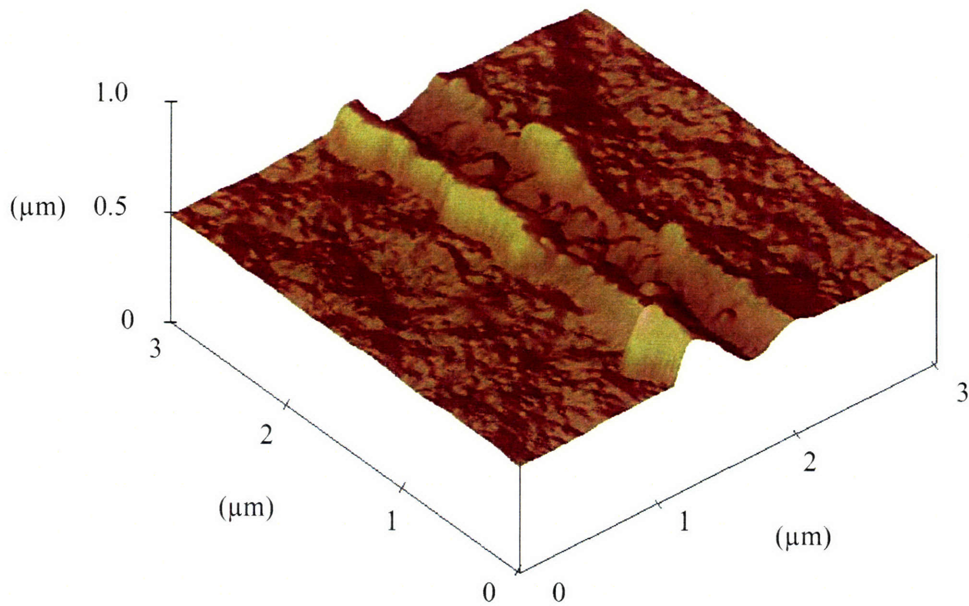

Figure 4.9: AFM image of a scratch made on a Cu coating at P = 277 µN and v = 0.33 µm/s.

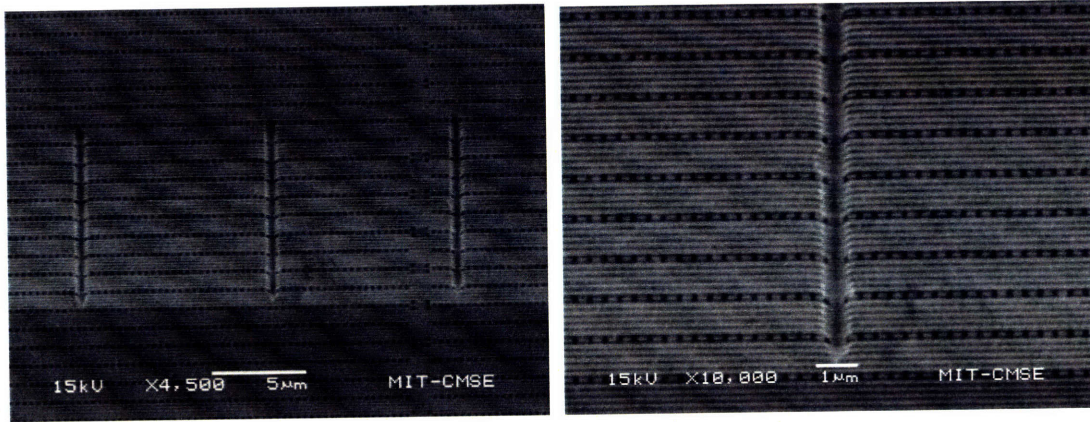

Figure 4.10: SEM micrographs of scratches made on a composite Cu/low-k dielectric A coating at P = 180 μN and v = 0.33 μm/s.

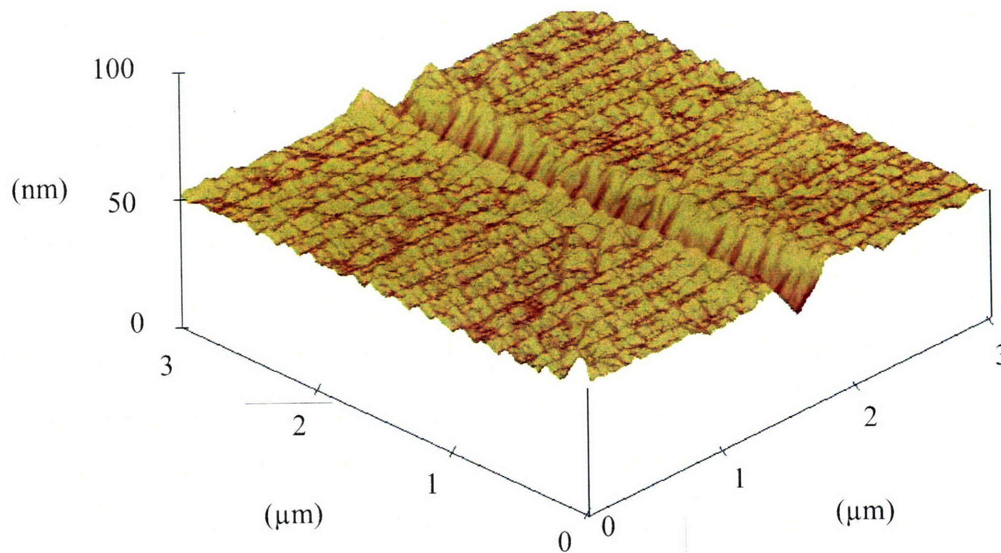

Figure 4.11: AFM image of a scratch made on a composite Cu/low-k dielectric B coating at P = 43 μN and v = 0.33 μm/s.

Table 4.2: Data from TriboIndenter scratch experiments on six different coatings: Cu, low-k dielectric A, low-k dielectric B, SiO_2, composite Cu/low-k dielectric A and composite Cu/low-k dielectric B. E = elastic and P = plastic deformation.

Material	P (μN)	v (μm/s)	δ_c (nm)	δ_c/R	a_c (nm)	a_c/R	E/P	F (μN)	μ_p
Cu	45	0.10	38	0.05	247	0.31	P	16	0.36
	45	0.33	27	0.03	208	0.26	P	15	0.33
	45	1.00	26	0.03	204	0.25	P	16	0.36
	90	0.10	48	0.06	277	0.35	P	36	0.40
	90	0.33	45	0.06	268	0.34	P	35	0.39
	90	1.00	45	0.06	268	0.34	P	32	0.36
	185	0.10	84	0.11	367	0.46	P	112	0.61
	185	0.33	73	0.09	342	0.43	P	106	0.57
	185	1.00	77	0.10	351	0.44	P	105	0.57
	275	0.33	140	0.18	473	0.59	P	185	0.67
low-k A	40	0.10	46	0.06	271	0.34	E	8	0.20
	40	0.33	43	0.05	262	0.33	E	9	0.23
	40	1.00	43	0.05	262	0.33	E	10	0.25
	85	0.10	53	0.07	291	0.36	P	11	0.13
	85	0.33	61	0.08	312	0.39	P	12	0.14
	85	1.00	52	0.07	288	0.36	P	12	0.14
	180	0.10	82	0.10	362	0.45	P	19	0.11
	180	0.33	84	0.11	367	0.46	P	19	0.11
	180	1.00	81	0.10	360	0.45	P	19	0.11
	283	0.33	88	0.11	375	0.47	P	33	0.12
low-k B	40	0.10	51	0.06	286	0.36	P	9	0.23
	40	0.33	46	0.06	271	0.34	P	9	0.23
	40	1.00	45	0.06	268	0.34	P	10	0.25
	85	0.10	66	0.08	325	0.41	P	13	0.15
	85	0.33	70	0.09	335	0.42	P	12	0.14
	85	1.00	67	0.08	327	0.41	P	14	0.16
	177	0.10	106	0.13	412	0.51	P	22	0.12
	177	0.33	110	0.14	420	0.52	P	20	0.11
	177	1.00	108	0.14	416	0.52	P	19	0.11
	277	0.33	124	0.16	445	0.56	P	47	0.17

Material	P (μN)	v (μm/s)	δ_c (nm)	δ_c/R	a_c (nm)	a_c/R	E/P	F (μN)	μ_p
SiO_2	48	0.10	6	0.01	98	0.12	E	9	0.19
	48	0.33	7	0.01	106	0.13	E	9	0.19
	48	1.00	6	0.01	98	0.12	E	11	0.23
	98	0.10	11	0.01	133	0.17	E	11	0.11
	98	0.33	8	0.01	113	0.14	E	11	0.11
	98	1.00	9	0.01	120	0.15	E	13	0.13
	195	0.10	18	0.02	170	0.21	P	19	0.10
	195	0.33	17	0.02	165	0.21	P	19	0.10
	195	1.00	17	0.02	165	0.21	P	20	0.10
Cu/low-k A	42	0.10	43	0.05	262	0.33	P	11	0.26
	42	0.33	36	0.05	240	0.30	P	12	0.29
	42	1.00	27	0.03	208	0.26	P	14	0.33
	90	0.10	48	0.06	277	0.35	P	23	0.26
	90	0.33	52	0.07	288	0.36	P	22	0.24
	90	1.00	45	0.06	268	0.34	P	23	0.26
	185	0.10	75	0.09	346	0.43	P	44	0.24
	185	0.33	81	0.10	360	0.45	P	42	0.23
	185	1.00	75	0.09	346	0.43	P	41	0.22
	277	0.33	115	0.14	429	0.54	P	74	0.27
Cu/low-k B	43	0.10	23	0.03	192	0.24	P	12	0.28
	43	0.33	19	0.02	174	0.22	P	13	0.30
	43	1.00	18	0.02	170	0.21	P	14	0.33
	90	0.10	40	0.05	253	0.32	P	20	0.22
	90	0.33	35	0.04	237	0.30	P	20	0.22
	90	1.00	35	0.04	237	0.30	P	21	0.23
	185	0.10	56	0.07	299	0.37	P	37	0.20
	185	0.33	56	0.07	299	0.37	P	37	0.20
	185	1.00	53	0.07	291	0.36	P	36	0.19
	283	0.33	75	0.09	346	0.43	P	60	0.21

Figure 4.12 shows a graph of the theoretical upper-bound loads, P_{UB}, versus the experimentally measured normal loads, P. The theoretical upper-bound loads were calculated using the experimentally measured depths of the scratches and Eq. (2.39) or Eq. (2.56) depending upon whether the coating was homogenous or composite in structure. Therefore, the points on the graph show the upper-bound, theoretical normal loads and the experimentally measured normal loads for a scratch with a given depth, δ_c. The solid line on the graph represents the boundary where the measured load equals the theoretically calculated upper-bound load. Therefore, all the points on the graph should fall above that line if the theoretical upper-bound actually provides a true upper-bound to the actual loads. As can be seen in Figure 4.12, almost all the points are above the solid line. Therefore, the upper-bound is validated. Thus, if a scratch is detected on a wafer surface, the width and depth of the scratch can be measured and then the theoretical upper-bound loads given by Eq. (2.39) and Eq. (2.56) can be used to predict what the load per particle was for that scratch to have been created. Figure 4.12 suggests that the calculated upper-bound load does predict the "worst-case" normal load. In other words, the true load per particle that made the scratch will be equal to or less than the calculated value.

Figure 4.13 is a graph of the normalized theoretical upper-bound normal loads versus the normalized measured normal loads. In both graphs it can be seen that the low-k dielectrics are furthest away from the solid line. This means that the predicted upper-bound load over-estimates the actual load more than for any of the other coatings. One reason for this is that the low-k dielectrics are so compliant due to their small Young's moduli that they do not exhibit the assumed fully-plastic behavior. If the low-k dielectrics experience a large degree of elastic spring-back, which was observed in the indentation tests, then the upper-bound theory will greatly over-estimate the actual load. The reason for this is that the depth of the scratch was measured while loaded. Therefore, the upper-bound load calculates what the normal load will be assuming a permanent, unloaded scratch depth of δ_c. If the low-k dielectrics stay mostly in the elastic regime, then the measured δ_c is not the true depth that should be used in the theory – the true depth will be less than this measured depth due to elastic spring-back. Therefore, using the measured depth as the permanent deformation over-estimates the actual normal load. Regardless, the predicted load will still provide an upper-bound.

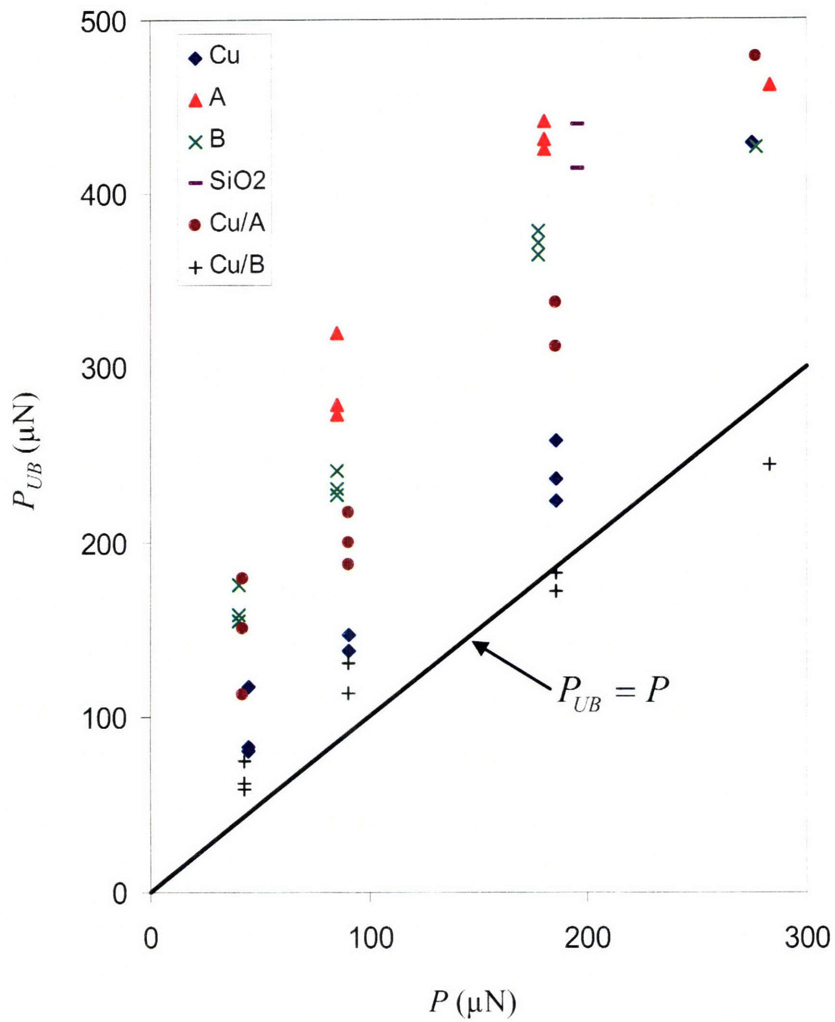

Figure 4.12: Comparison of the upper-bound load, P_{UB}, with the experimentally measured normal load, P.

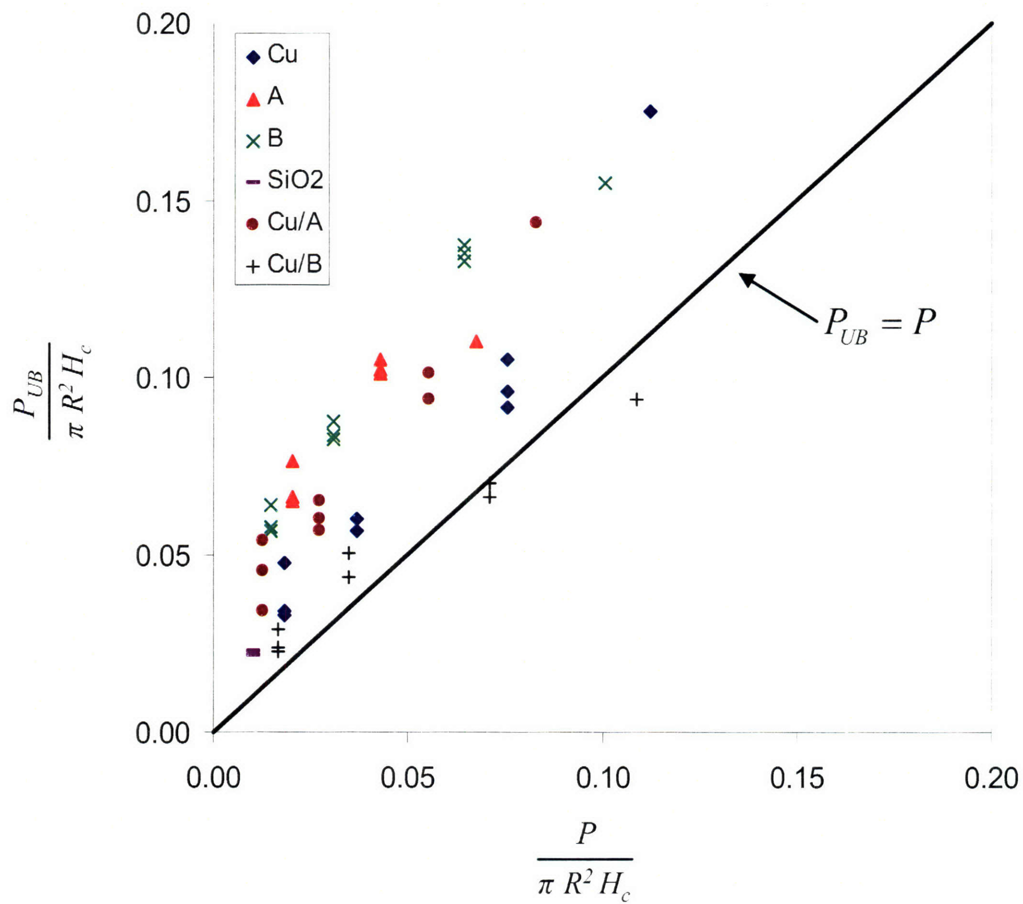

Figure 4.13: Comparison of the normalized upper-bound load with the normalized experimentally measured normal load.

Figure 4.14 shows the coefficient of friction versus the depth of the scratch normalized by the particle radius. The line represents the theoretical coefficient of friction given by Eqs. (2.57) and (2.66) where it was assumed that for all of the coatings $\mu_{ad} = 0.16$. As can be seen in Figure 4.14, there is relatively large scatter in the data. This is to be expected because it is very difficult to repeatedly and consistently measure the coefficient of friction for thin film coatings. In addition, the data points shown in Figure 4.14 include the coefficient of friction from all scratching tests, which were conducted at varying loads and varying depths of penetration. Hence, a large spread in the data is not surprising. It should be noted that determining the coefficient of friction of thin film coatings is not the major emphasis of this thesis, but a useful byproduct.

Finally, Table 4.3 shows the experimental and theoretical values for the Preston constant of Cu, low-k dielectric A and low-k dielectric B. Both the average values and the standard deviations are presented. The theoretical values were calculated based upon the data obtained from the controlled scratching experiments and Eq. (2.75). The experimental values were obtained by polishing 100-mm blanket wafers on a standard CMP tool with Cabot Microelectronics iCue 5001 slurry with 3% H_2O_2.

Not surprisingly, the theoretical Preston constants are two orders of magnitude larger than the experimental Preston constants. One explanation for this is that under experimental conditions, the slurry particles are not continuously loaded nor in continuous contact with the coating. Additionally, part of the load is supported by the pad contacting the coating directly, thereby decreasing the load per particle. Therefore, the theoretical values are in a way, the "best case" Preston constant values in terms of the material removal rate. In addition, it was expected that the experimental and theoretical values would not be equal because the particle sizes and velocities were not the same in the theoretical and experimental tests. Furthermore, the scratching tests were conducted in a dry environment, whereas the blanket wafers were polished with particles and 3% H_2O_2 in an aqueous solution.

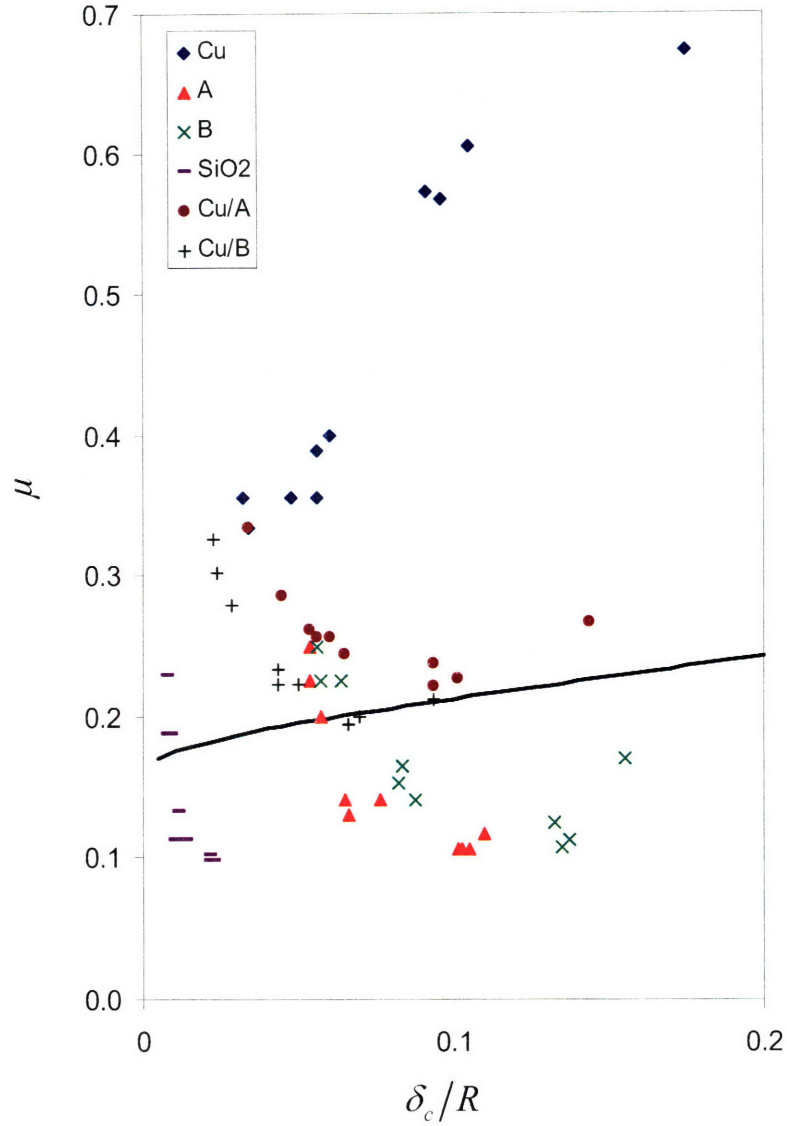

Figure 4.14: Coefficient of friction (tip radius 800 nm).

Table 4.3: Theoretical and experimental values of the Preston constant of Cu, low-k dielectric A and low-k dielectric B.

Material	$k_{p,th}$ (10^{-13} m^2/N)		$k_{p,exp}$ (10^{-13} m^2/N)	
	Avg.	Std. Dev.	Avg.	Std. Dev.
Cu	356	118	1.60	0.50
low-k A	217	37	1.01	0.30
low-k B	377	87	1.20	0.31

4.5 Multi-Particle Contact Models: Polishing Experiments

The experimental validation of the multi-particle contact models involved the use of an adapted, experimental face-up CMP tool. The face-up CMP tool is shown in Figure 4.15. The clear box in the middle of the photograph houses the polishing head. The surrounding equipment consists of speed controllers for the pad and wafer motors, a high-pressure air supply to apply normal pressure to the pad and a pump to deliver slurry into the polishing region.

Figure 4.16(a) shows a close-up view of the polishing apparatus and Figure 4.16(b) shows the Cu sample being polished. The rubber chuck is capable of holding wafers that range from any size or shaped piece of a wafer to a circular wafer 300 mm in diameter. As can be seen in Figure 4.16, a pad that is approximately 70 mm in diameter is used to concentrically polish a square piece of a Cu wafer that is 75 mm x 75 mm. The reason for polishing a square sample is that it is easier to cleave square samples rather than circular samples from 300-mm wafers supplied by Intel. A Rohm and Haas IC1000 CMP pad was used for all the polishing experiments.

For the first round of experiments, the pad was rotated at 125 rpm for 30 s with a pressure of 10.3 kPa (1.5 psi). This, however, led to a very badly scratched surface with long, concentric scratches. In addition, the scratches were so clustered that it was difficult to distinguish one scratch from another. The slurry used for these experiments was the Cabot Microelectronics iCue 5001 Cu CMP slurry. The nominal particle size is 3 μm and the factory measured particle size is 2.97 μm. The suggested addition of 3% H_2O_2 was not incorporated into the slurry because only the mechanical effects of the slurry particles were desired.

During the second round of tests, the pad was rotated manually only a fraction of a revolution (approximately 45 degrees) so that discrete scratches were formed. A pressure of 8.3 kPa (1.2 psi) was applied to the back of the pad. The Cabot Microelectronics iCue 5001 Cu CMP slurry with a nominal particle size of 3 μm was used. For these CMP scratching experiments, a Cu coating as well as a low-k dielectric B coating were tested. Representative SEM micrographs of the Cu and low-k dielectric B coating are shown in Figure 4.17(a) and 4.17(b), respectively.

As can be seen in Figure 4.17, the scratches resulting from the experiment on both Cu and the low-k dielectric B coating are aligned such that they run from the upper-left to the lower-

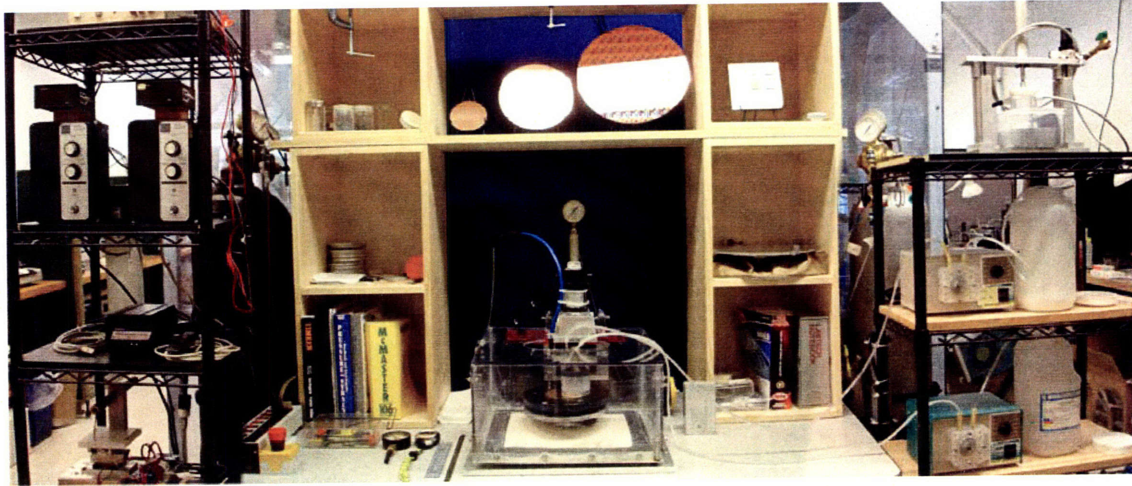

Figure 4.15: The face-up CMP tool.

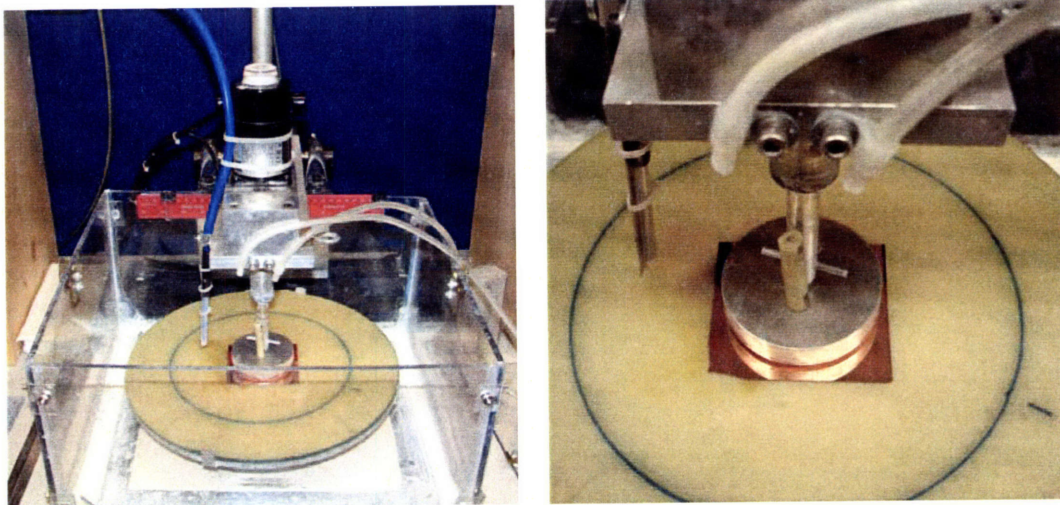

(a) (b)

Figure 4.16: (a) An overview of the polishing head and (b) a close up of a Cu sample during a test.

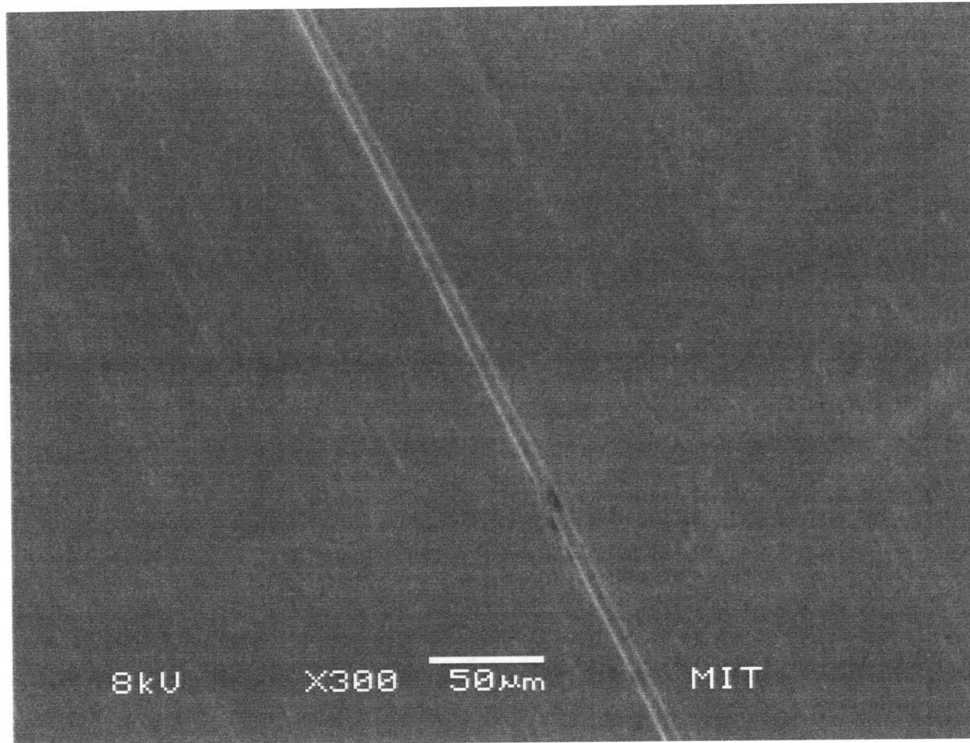

(a)

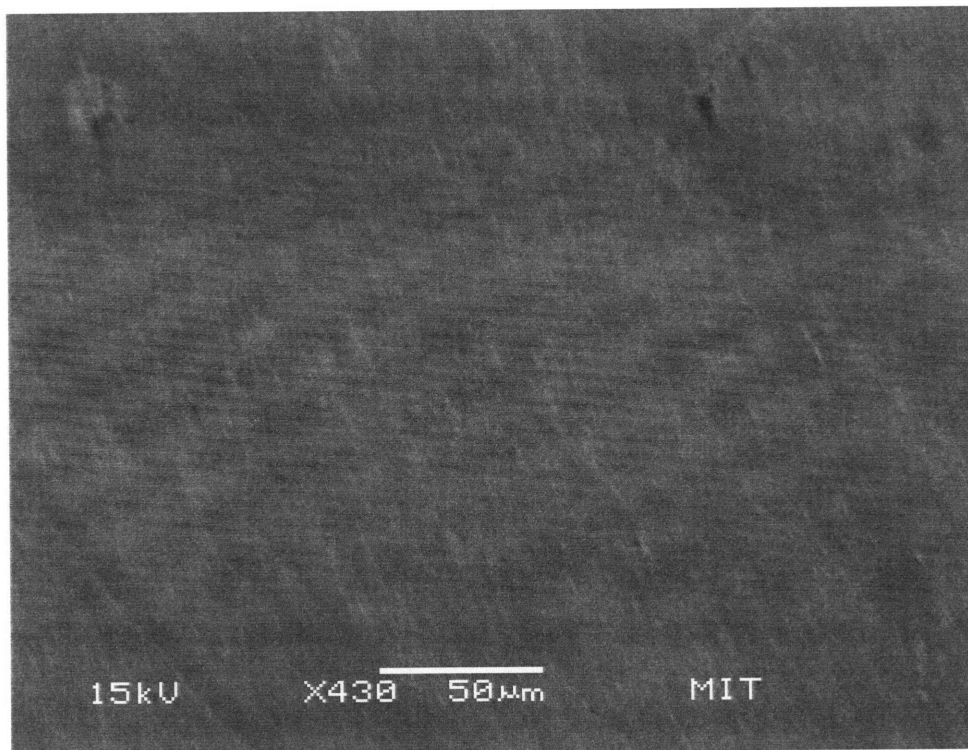

(b)

Figure 4.17: Scratches formed during a CMP experiment, using particles 3 μm in size, on: (a) a Cu coating and (b) a low-k dielectric B coating.

right corners of the micrographs. Any scratches or blemishes seen that do not travel in this direction are a result from secondary handling - not from CMP. The prominent scratch seen on the Cu coating in Figure 4.17(a) is approximately 15 μm wide. This scratch can serve as a reference to compare the widths of the narrower scratches to the right and left of this scratch. There are many scratches parallel to the prominent scratch consisting of varying widths from less than 1 μm to 15 μm. This is consistent with Figure 3.16, which predicts that the normalized scratch semi-widths on a Cu coating range from close to 0 to 0.2. Figure 4.17(a) shows that the variation in the width of scratches is well distributed. In Figure 4.17(b), the width of observed scratches is approximately 5-15 μm. Therefore, for the same slurry, the observed scratch widths on the low-k dielectric B coating are not as small as the observed scratch widths on the Cu coating. This is also consistent with Figure 3.16 which predicts that for the low-k dielectric B, the normalized scratch semi-widths range from 0.13 to 0.19. Therefore, it is expected that the size of scratches present on the low-k B coating are not as small as the scratches present on the Cu coating.

A third round of polishing experiments, using smaller particles, was conducted on Cu, low-k dielectric B and SiO_2. Similar to previous tests, the pad was rotated by hand a fraction of a revolution. For these tests, a pressure of 12.4 kPa (1.8 psi) was applied to the back of the pad. Furthermore, the Cabot Microelectronics C7092 Cu CMP slurry was used. This slurry has a nominal particle size of 90 nm and a factory measured size of 91 nm. Representative SEM micrographs of the Cu, low-k dielectric B and SiO_2 coatings are shown in Figure 4.18(a), 4.18(b) and 4.18(c), respectively.

Figure 4.18(a) shows a scratch 300 nm wide created by a particle 350 nm wide. This is the order of magnitude of the problem scratch sizes present in industrial CMP. This is also consistent with Figure 3.16 in that scratches on Cu are easily produced. It may be noted that the particle shown in Figure 4.18(a) is not spherical; it has an elliptically-shaped bottom. Figure 4.18(b) shows particles sitting on the surface of a low-k dielectric B coating. No scratches can be seen around the particles. Therefore, this is consistent with the low-k dielectric B line plotted in Figure 3.16 which shows a limited range of possible scratch widths, and only at high pressure. Figure 4.18(c) shows particles sitting on SiO_2. Similar to the low-k dielectric B, no scratches are present. This is consistent with the theory presented in Chapter 3, which predicts scratching will not occur on SiO_2.

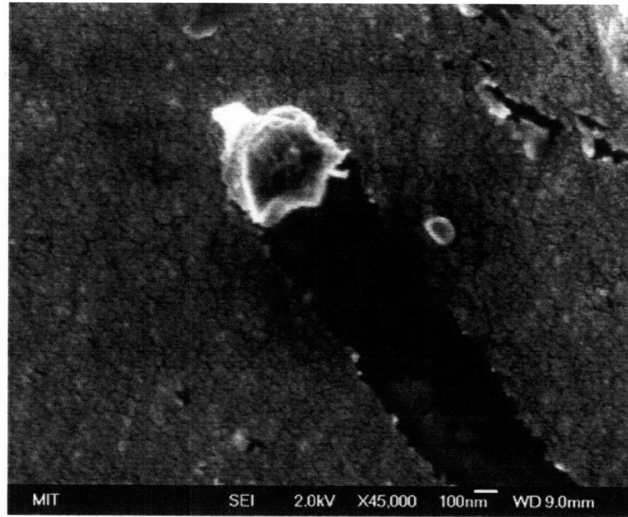

(a)

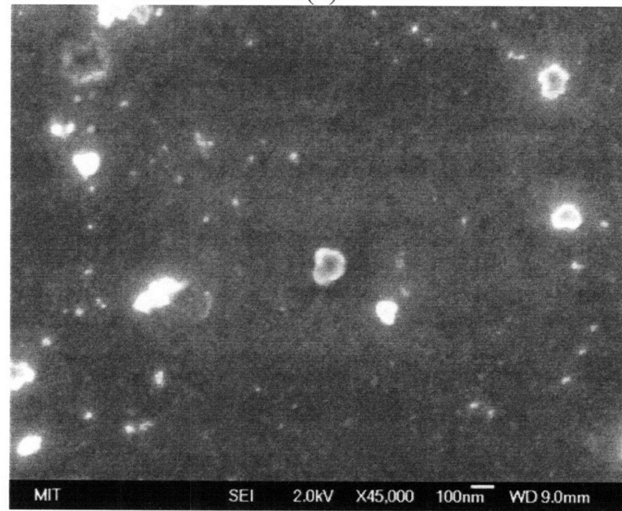

(b)

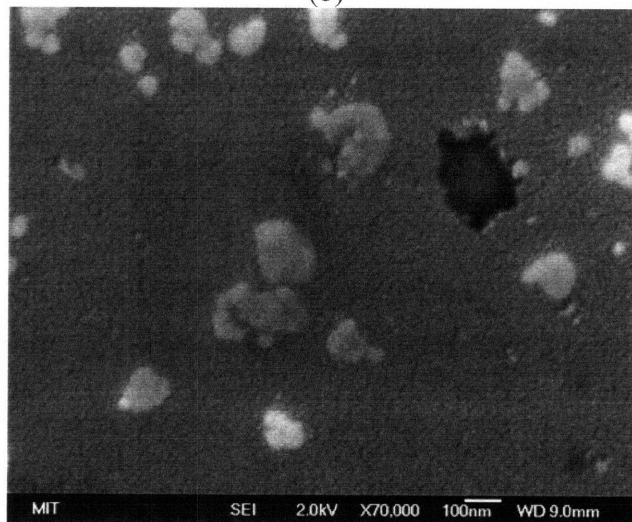

(c)

Figure 4.18: Micrographs following a CMP experiment, using particles 90 nm in size, on: (a) Cu, (b) low-k dielectric B and (c) SiO_2.

It is difficult to determine what the expected upper-limit of scratch width should be in these CMP experiments because the particle size and shape are not uniform, key assumptions in the model. Furthermore, the particle size distribution is not very tight – agglomeration has created a large variation in particle sizes. Therefore, a different upper-limit is appropriate for every different particle size. It is difficult to discern whether a very large, agglomerated particle created some of the scratches seen in Figure 4.17, in which case the scratches are well below the upper-limit, or if smaller particles of varying sizes made these scratches, in which case the observed scratch widths could be equal to the respective upper-limits for each of the particle sizes. Nevertheless, the point that Figure 3.16 captures is validated by Figures 4.17 and 4.18. Specifically, it shows that the range of scratch widths expected on a Cu coating is much larger than the range of scratch widths expected on a low-k dielectric or SiO_2 coating.

Figure 4.19 shows an SEM micrograph of the surface of low-k dielectric B with slurry particles, nominally 3 μm in size. As can be seen, the effective slurry particles are not of uniform size and the average particle radius is greater than 3 μm. Therefore, agglomeration very likely had occurred and the average effective particle radius is 10-20 μm. To validate the upper-limit for scratch width, the appropriate average particle size must be used for the normalization. If the particles present are larger than the value used to normalize, then the upper-limit can be exceeded because the true "effective" particle radius was not used. Figure 4.19 also shows larger scratches were present on the coatings. The reason for that is that the pad asperities themselves can scratch the coatings. In addition, very large, agglomerated particles can create very wide scratches on the order of 50 μm. However, only the scratches at the smallest scale are analyzed - the realistic size of scratches usually present after CMP in a clean room.

4.6 Summary

Indentation experiments were conducted to verify the moduli and hardnesses of the coating materials and the pads. The scratching experiments were conducted to verify the presented single-particle models. The upper-bound load was validated by the Hysitron TriboIndenter scratching experiments. Polishing experiments, using a CMP tool, were performed on Cu, low-k dielectric and SiO_2 coatings to validate the lower and upper-limits of predicted scratch widths. The experiments qualitatively validate the range of the lower and upper-limits.

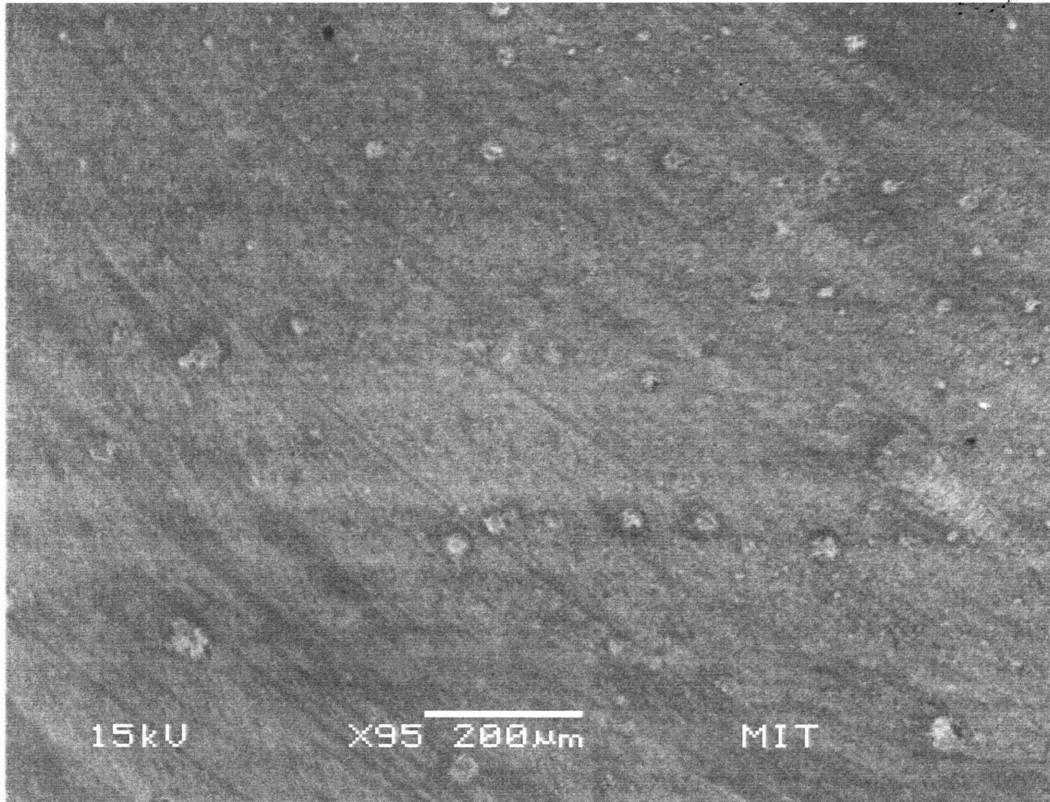

Figure 4.19: Agglomerated particles, nominally 3 μm in size, on the surface of the low-k dielectric B coating.

CHAPTER 5

CONCLUSIONS

5.1 Summary

In this thesis, scratching models based on the pad-particle-coating contact mechanics during CMP have been developed. Upper-limits for the width and depth of a scratch in a coating were defined, and on the basis of these limits solutions to mitigate scratching have been suggested.

Chapter 2 introduced single-particle contact models of various homogenous and composite coatings. First, the coatings were assumed to deform elastically. From the elastic analysis, the yield load at the onset of plastic flow, the radius of contact area, and the depth of particle penetration into the coating were determined. Second, the coatings were assumed to deform rigid-plastically. From the rigid-plastic analysis, an upper-bound load, which relates the load per particle to the width and depth of a scratch in the coating, was obtained.

Chapter 3 presented multi-particle contact models and the combined pad-particle-coating interaction was modeled. The widths and depths of scratches were related to the controllable process parameters, such as the polishing pressure, particle radius, slurry volume fraction and the mechanical and geometric properties of the pad and coating. First, a smooth pad was analyzed to relate the load per particle to the applied polishing pressure. With this relation in place, the scratch width and depth as a function of the process parameters were obtained. The smooth pad model predicts scratch sizes that are too small to be considered the dominant scratches in industrial CMP practice. Second, a rough pad was analyzed. The widths and depths of scratches were determined based on the elastic and plastic deformation of the pad. The transition pressure from elastic-to-plastic deformation of the pad was calculated to be 830 Pa (0.12 psi). This is a relatively low pressure compared with typical CMP pressures. Therefore, it was concluded that a majority of the pad asperities deform plastically. Assuming that both the pad and coating deform plastically, lower and upper-limits were defined for the width and depth of scratches in a coating. These limits depend only on the mechanical properties of the pad and the coating, and the particle radius. Therefore, changing the geometry of the pad asperities may not affect scratching.

In Chapter 4 experimental validation of the scratching models was presented. The upper-bound analysis of Chapter 2 was validated by controlled scratching experiments on a Hysitron TriboIndenter. The depths of the controlled scratches were measured, and the predicted upper-bound loads compared with the experimentally measured loads. For almost all the coatings, the upper-bound load was above or close to the experimental load, which shows that the load per particle could be related to the width and depth of a scratch fairly well. Furthermore, polishing experiments using a CMP tool were conducted on homogenous Cu and low-k dielectric coatings to qualitatively validate the lower- and upper-limits of scratching presented in Chapter 3. For the Cu coating, the broad range of observed scratch widths is consistent with the wide range predicted by the theory. In addition, the narrower range of scratch widths observed on the low-k dielectric coating is also consistent with the multi-particle analysis.

Based on the developed scratching models, as well as the experiments, the following recommendations are made for mitigating scratching in CMP:

(a) Use pads with low hardness (i.e., soft pads),

(b) Increase the hardness of the coating,

(c) Decrease the radius of the slurry particles,

(d) Use a large slurry volume fraction, and

(e) Use low polishing pressures.

5.2 Suggestions for Future Work

Based on the scratching models and the experiments presented in this thesis, further research in the following areas is recommended to reduce scratching during the CMP process: composite coatings, pad mechanical properties, and particle agglomeration.

Composite Coatings: In this thesis, the CMP experiments have been performed only on homogenous Cu and low-k dielectric coatings. In industrial practice, however, scratching is of the composite Cu/low-k dielectric coating is of major concern. Although the developed theory is very similar for homogenous and composite coatings, experiments should be conducted on composite coatings to further validate the defined upper-limits on scratching. Furthermore, experiments should be conducted on 300-mm wafers on industrial CMP tools.

Pad Material Properties: Measurement of the mechanical properties of the pads revealed a large variation in local modulus and hardness (Appendix B). In order to keep scratch width at a minimum, the variation of mechanical properties of the pad material at a local scale should be minimized. In addition, it was observed that the pad asperities themselves could scratch the coatings. Although this appears to be most serious for Cu coatings and of minimal concern for a composite coating, analyzing and eliminating this type of scratching must be addressed.

Particle Agglomeration: Above all, in order to fully benefit from the upper-limits defined for scratching, slurries with uniform particle size, or at least with a tight distribution of particle size, should be used for polishing. This implies that particle agglomeration needs to be analyzed and minimized. Agglomeration may be reduced by charging the abrasive particles in the slurry.

APPENDIX A

ROUGH PAD – SINUSOIDAL ASPERITIES

Modeling the pad surface as sinusoidal is a more realistic approach than the hemi-spherical assumption presented in Chapter 3. The reason for this is that any pad surface topography can be expressed as a summation of sinusoidal functions. In addition, by modeling the pad as a sinusoidal curve, the roughness can be expressed as a function of the asperity spacing and the radius of curvature of an asperity. The usefulness of this approach is that the roughness of a pad can be relatively easily obtained from a topographical scan of the pad surface. Figure A.1 shows a 2D image of the surface of a Rohm and Haas IC1000 pad. An Olympus LEXT Confocal Microscope analyzed a plane on the surface of the pad and from that calculated the root-mean-square roughness, R_q. The measured root-mean-square roughness was 25.3 μm.

If the topography of the pad is assumed to be sinusoidal, similar to the one shown in Figure A.2, then the function that describes the pad texture is:

$$z = z_o \sin\left(\frac{2\pi}{\lambda_a}x\right) \tag{A.1}$$

where z_o is the amplitude. The first and second derivatives of Eq. (A.1), respectively, are:

$$\frac{dz}{dx} = z_o\left(\frac{2\pi}{\lambda_a}\right)\cos\left(\frac{2\pi}{\lambda_a}x\right) \tag{A.2}$$

$$\frac{d^2z}{dx^2} = -z_o\left(\frac{2\pi}{\lambda_a}\right)^2 \sin\left(\frac{2\pi}{\lambda_a}x\right) \tag{A.3}$$

The second derivative, given in Eq. (A.3), is the curvature of an asperity.

$$\left.\left(\frac{d^2z}{dx^2}\right)\right|_{x=\frac{3}{4}\lambda_a} = \frac{1}{R_a} \tag{A.4}$$

An explicit relation for R_a can be obtained as:

$$R_a = \frac{\lambda_a^2}{4\pi^2 z_o} \tag{A.5}$$

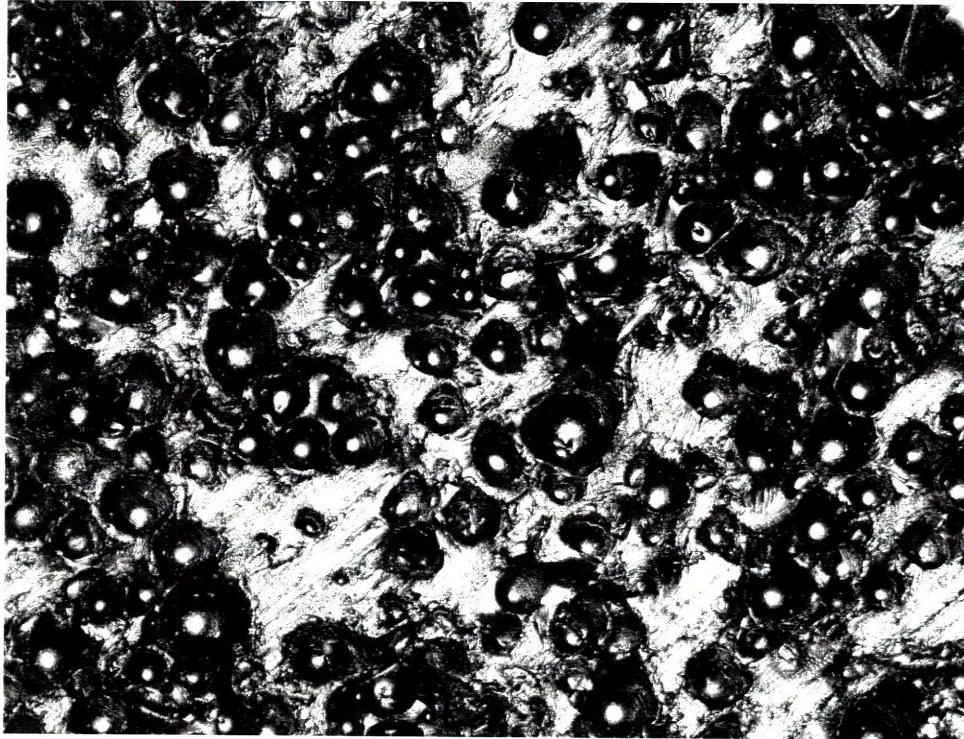

Figure A.1: Topography of a Rohm and Haas IC1000 pad. Image taken with an Olympus LEXT Confocal Microscope. $R_q = 25.3$ µm.

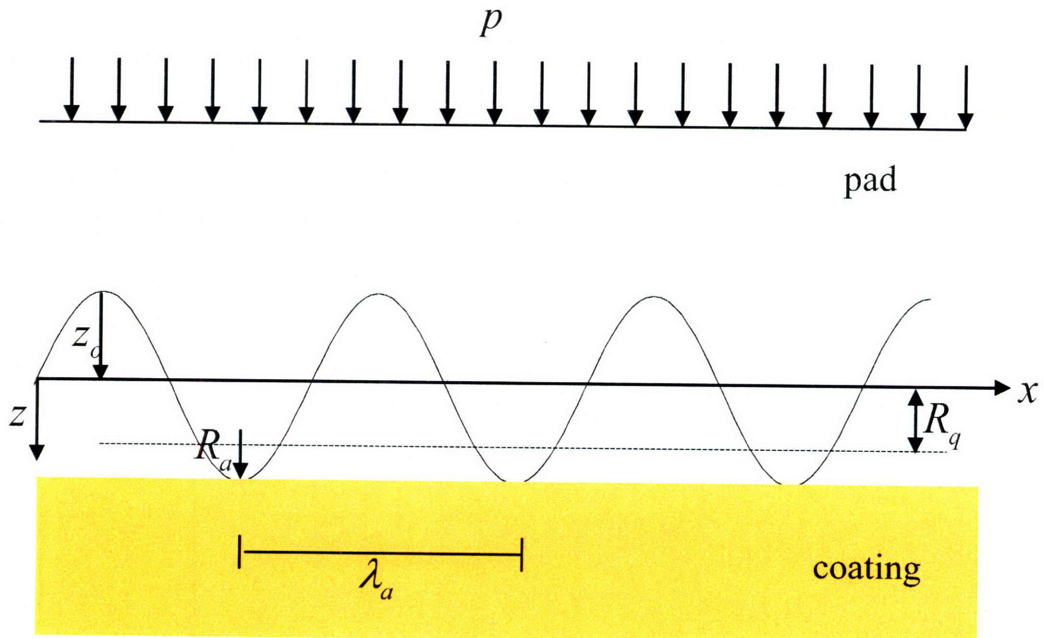

Figure A.2: Schematic of a rough pad with sinusoidal asperities.

The root-mean-square (rms) roughness of the sinusoidal function given in Eq. (A.1) is defined as:

$$R_q = \frac{z_o}{\sqrt{2}} \tag{A.6}$$

Therefore, the radius of curvature of an asperity can be explicitly solved for by substituting Eq. (A.6) into Eq. (A.5):

$$R_a = \frac{1}{\pi^2 \sqrt{32}} \frac{\lambda_a^2}{R_q} \tag{A.7}$$

Eq. (A.7) provides a useful expression to relate the radius of curvature of an asperity, a difficult quantity to measure directly, to the asperity spacing and root-mean-square roughness of the pad, which can be relatively easily measured using a profilometer. In this respect, this relation is similar to Eq. (3.2) which provides an expression that relates the spacing between particles, a typically unknown parameter, to the volume fraction of the slurry and particle radius, two known quantities. Therefore, all of the summary equations in Table 3.6 can be rewritten to eliminate R_a. Table A.1 shows the summary equations for a pad with sinusoidal asperities. It may be noted that the limiting equations are unaffected by whether or not the pad asperities are modeled as hemi-spherical or sinusoidal in shape. The reason for this is that the limiting equations, which govern the maximum scratch size, are only a function of the pad and coating mechanical properties.

Table A.1: Summary of rough pad equations for a pad with sinusoidal asperities.

	Pad-Particle	Coating-Particle
1. Elastic Contact	$\frac{a_p}{R} = (24\pi)^{1/9} \left(\frac{p}{E_p}\right)^{1/9} \left(\frac{\lambda_p}{R}\right)^{2/3} \left(\frac{R_q}{\lambda_a}\right)^{2/9}$ $\frac{\delta_p}{R} = (24\pi)^{2/9} \left(\frac{p}{E_p}\right)^{2/9} \left(\frac{\lambda_p}{R}\right)^{4/3} \left(\frac{R_q}{\lambda_a}\right)^{4/9}$	Coating elastic: $\frac{a_c}{R} = (24\pi)^{1/9} \left(\frac{E_p}{p}\right)^{2/9} \left(\frac{p}{E_c}\right)^{1/3} \left(\frac{R_q}{\lambda_a}\right)^{2/9} \left(\frac{\lambda_p}{R}\right)^{2/3}$ $\frac{\delta_c}{R} = (24\pi)^{2/9} \left(\frac{E_p}{p}\right)^{4/9} \left(\frac{p}{E_c}\right)^{2/3} \left(\frac{R_q}{\lambda_a}\right)^{4/9} \left(\frac{\lambda_p}{R}\right)^{4/3}$ Transition pressure: $p_{Y,c} = \frac{\pi^8}{3 \cdot 2^{21}} \left(\frac{R}{\lambda_p}\right)^6 \left(\frac{\lambda_a}{R_q}\right)^2 \frac{H_c^9}{E_c^6 E_p^2}$ Coating plastic: $\frac{a_c}{R} = \left(\frac{2^6}{3\pi}\right)^{1/3} \left(\frac{E_p}{p}\right)^{1/3} \left(\frac{p}{H_c}\right)^{1/2} \left(\frac{\lambda_p}{R}\right) \left(\frac{R_q}{\lambda_a}\right)^{1/3}$ $\frac{\delta_c}{R} = \left(\frac{2^9}{3^2 \pi^2}\right)^{1/3} \left(\frac{E_p}{p}\right)^{2/3} \left(\frac{p}{H_c}\right) \left(\frac{\lambda_p}{R}\right)^2 \left(\frac{R_q}{\lambda_a}\right)^{2/3}$
2. Onset of Yielding	$\frac{a_{Y,a}}{R} = \frac{1}{2^4 \sqrt{2}\pi} \frac{\lambda_a^2 H_p}{R_q R E_p}$ $\frac{\delta_{Y,a}}{R} = \frac{1}{2^6 \sqrt{2}} \frac{\lambda_a^2 H_p^2}{R_q R E_p^2}$ $p_{Y,a} = \frac{1}{3 \cdot 2^9 \pi} \frac{\lambda_a^2 H_p^3}{R_q^2 E_p^2}$	$\frac{a_{Y,c}}{R} = \frac{\pi}{4} \frac{H_c}{E_c}$ $\frac{\delta_{Y,c}}{R} = \frac{\pi^2}{16} \frac{H_c^2}{E_c^2}$ $p_{Y,c} = \frac{\pi^8}{3 \cdot 2^{21}} \left(\frac{R}{\lambda_p}\right)^6 \left(\frac{\lambda_a}{R_q}\right)^2 \frac{H_c^9}{E_c^6 E_p^2}$
3. Limiting Case	$\frac{a_p}{R} = 1$ $\frac{\delta_p}{R} = 1$	$\frac{a_c}{R} = \sqrt{\frac{H_p}{H_c}}$ $\frac{\delta_c}{R} = \frac{H_p}{H_c}$

Nomenclature

a_a = radius of asperity contact area (m)

a_c = scratch semi-width in a coating (m)

a_p = radius of particle indentation into a pad (m)

$a_{Y,a}$ = radius of asperity contact area at pad yield (m)

$a_{Y,c}$ = scratch semi-width in a coating at yield (m)

$a_{Y,p}$ = radius of particle indentation into a pad at yield (m)

E_c = Young's modulus of a coating (N/m^2)

E_p = Young's modulus of a pad (N/m^2)

H_c = hardness of a coating (N/m^2)

H_p = hardness of a pad (N/m^2)

p = pressure (N/m^2)

$p_{Y,a}$ = yield pressure for a pad asperity (N/m^2)

$p_{Y,c}$ = yield pressure for a coating (N/m^2)

$p_{Y,a}$ = yield pressure for a pad (N/m^2)

R = radius of a particle (m)

R_a = radius of curvature of an asperity (m)

R_q = root-mean-square roughness (m)

z_o = amplitude of sinusoidal pad topography (m)

δ_c = depth of a scratch in a coating (m)

δ_p = depth of indentation into a pad (m)

$\delta_{Y,c}$ = depth of a scratch in a coating at yield (m)

$\delta_{Y,p}$ = depth of indentation into a pad at yield (m)

λ_a = spacing between asperities (m)

λ_P = spacing between particles (m)

APPENDIX B

PAD INDENTATION DATA

The indentation data for a dry Rohm and Haas IC1000 pad are listed in Table B.1. The modulus and hardness data are shown as histograms in Figure B.1 and Figure B.2.

Table B.1: Modulus and hardness of a dry Rohm and Haas IC 1000 pad.

Test Number	E_p (GPa)	H_p (GPa)
1	1.25	0.12
2	2.16	0.11
3	1.07	0.09
4	1.37	0.10
5	0.87	0.10
6	0.88	0.12
7	0.08	0.03
8	1.29	0.11
9	1.25	0.12
10	1.11	0.18
11	0.14	0.02
12	0.14	0.03
13	0.07	0.03
14	1.16	0.10
15	1.37	0.12
16	0.17	0.04
17	0.18	0.05
18	0.16	0.04
19	0.10	0.01
20	0.13	0.02
21	1.73	0.14
22	1.49	0.13
23	1.17	0.05
24	1.86	0.15
25	0.51	0.03
26	0.79	0.04
27	1.33	0.10
28	1.33	0.11
29	2.56	0.31
30	2.79	0.15
31	0.47	0.03
32	1.06	0.08
33	1.26	0.12
34	1.38	0.12
35	2.08	0.23
36	3.42	0.20
Avg.	1.12	0.10
Std. Dev.	0.82	0.06

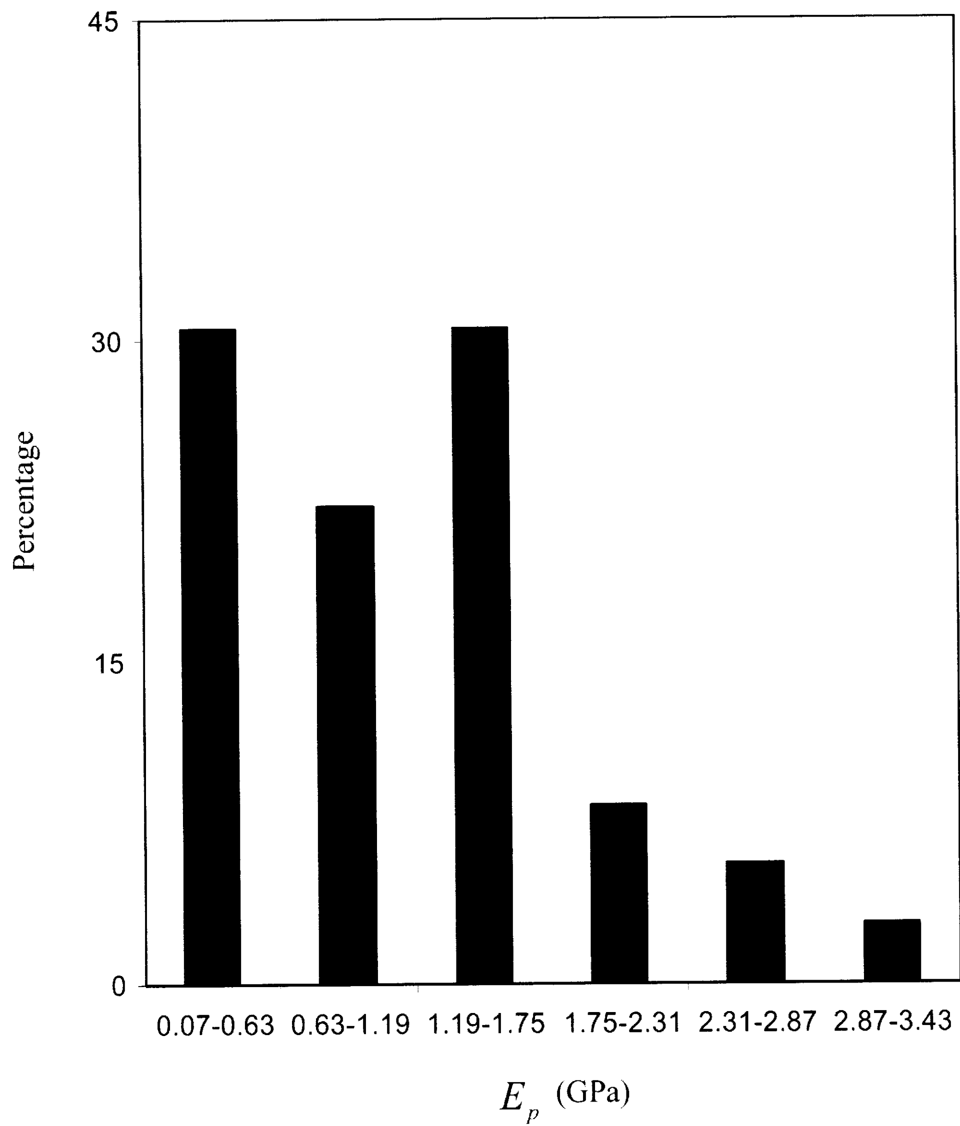

Figure B.1: Variation of pad modulus for a Rohm and Haas IC1000 pad (dry).

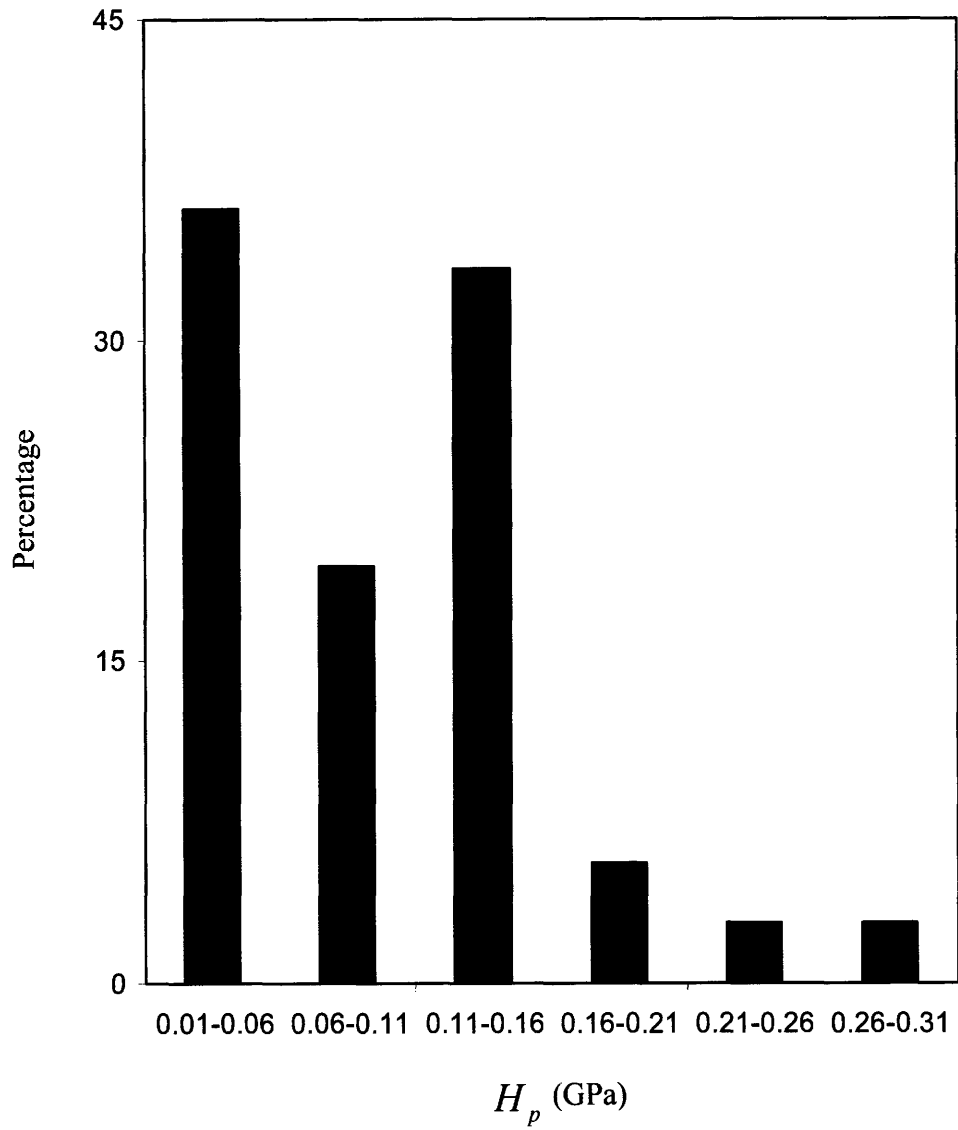

Figure B.2: Variation of pad hardness for a Rohm and Haas IC1000 pad (dry).

REFERENCES

Borst, C.L., Gill, W.N. and Gutmann, R.J., 2002, **Chemical-Mechanical Polishing of Low Dielectric Constant Polymers and Organosilicate Glasses**, Kluwer Academic, Boston, MA.

Chang, C.Y. and Sze, S.M., 1996, **ULSI Technology**, McGraw-Hill, New York.

Che, W., Guo, Y., Chandra, A. and Bastawros, A., 2005, "A Scratch Intersection Model of Material Removal During Chemical Mechanical Planarization (CMP)," *Journal of Manufacturing Science and Engineering*, vol. 127, pp. 545-554.

Che, W., Guo, Y., Chandra, A. and Bastawros, A.-F., 2003, "Mechanistic Understanding of Material Detachment During Micro-Scale Polishing," *Journal of Manufacturing Science and Engineering*, vol. 125, pp. 731-735.

Chen, W.-C., Lin, S.-C., Dai, B.-T. and Tsai, M.-S., 1999, "Chemical Mechanical Polishing of Low-Dielectric-Constant Polymers: Hydrogen Silsesquioxane and Methyl Silsesquioxane," *Journal of The Electrochemical Society*, vol. 146, pp. 3004-3008.

Cook, L.M., 1990, "Chemical Processes in Glass Polishing," *Journal of Non-Crystalline Solids*, vol. 120, pp. 152-171.

Dejule, R., 1998, "CMP Grows in Sophistication," *Semiconductor International*, vol. 21, pp. 56-62.

Fu, G., Chandra, A., Guha, S. and Subhash, G., 2001, "A Plasticity-Based Model of Material Removal in Chemical-Mechanical Polishing (CMP)," *IEEE Transactions on Semiconductor Manufacturing*, vol. 14, pp. 406-417.

Gutmann, R.J., Steigerwald, J.M., You, L., Price, D.T., Neirynck, J. Duquette, D.J. and Murarka, S.P., 1995, "Chemical-Mechanical Polishing of Copper with Oxide and Polymer Interlevel Dielectrics," *Thin Solid Films*, vol. 270, pp. 596-600.

International Technology Roadmap for Semiconductors (ITRS) – Reports, Interconnect [Online] http://www.itrs.net.

Johnson, K.L., 1985, **Contact Mechanics**, Cambridge University Press, U.K.

Kaufman, F.B., Thompson, D.B., Broadie, R.E., Jaso, M.A., Guthrie, W.L., Pearson, D.J. and Small, M.B., 1991, "Chemical-Mechanical Polishing for Fabricating Patterned W Metal Features as Chip Interconnects," *Journal of The Electrochemical Society*, vol. 138, pp. 3460-3465.

Lai, J.-Y., Saka, N. and Chun, J.-H., 2002, "Evolution of Copper-Oxide Damascene Structures in Chemical Mechanical Polishing," *Journal of The Electrochemical Society*, vol. 149, pp. G31-G40.

Luo, J. and Dornfeld, D. A., 2001, "Material Removal Mechanism in Chemical Mechanical Polishing: Theory and Modeling," *IEEE Transactions on Semiconductor Manufacturing*, vol. 14, pp. 112-133.

Luo, J. and Dornfeld, D. A., 2003, "Effects of Abrasive Size Distribution in Chemical Mechanical Planarization: Modeling and Verification," *IEEE Transactions on Semiconductor Manufacturing*, vol. 16, pp. 469-476.

Luo, J. and Dornfeld, D. A., 2003, "Material Removal Regions in Chemical Mechanical Planarization for Submicron Integrated Circuit Fabrication: Coupling Effects of Slurry Chemicals, Abrasive Size Distribution, and Wafer-Pad Contact Area," *IEEE Transactions on Semiconductor Manufacturing*, vol. 16, pp. 45-56.

Ma, Y., Yang, H., Guo, J., Sathe, C., Agui, A. and Nordgren, J., 1998, "Structural and Electronic Properties of Low Dielectric Constant Fluorinated Amorphous Carbon Films," *Applied Physics Letters*, vol. 72, pp. 3353-3355.

Maex, K., Baklanov, M.R., Shamiryan, D., Iacopi, F., Brongersma, S.H. and Yanovitskaya, Z.S., 2003, "Low Dielectric Constant Materials for Microelectronics," *Journal of Applied Physics*, vol. 93, pp. 8793-8841.

Maier, G., 2001, "Low Dielectric Constant Polymers for Microelectronics," *Progress in Polymer Science*, vol. 26, pp. 3-65.

Martin, S.J., Godschalx, J.P., Mills, M.E., Shaffer, E.O. II and Townsend, P.H., 2000, "Development of a Low-Dielectric-Constant Polymer for the Fabrication of Integrated Circuit Interconnect," *Advanced Materials*, vol. 12, pp. 1769-1778.

Miyoshi, A., Nakagawa, H. and Matsukawa, K., 2005, "Simulation on Chemical Mechanical Polishing Using Atomic Force Microscope," *Microsystems Technology*, vol. 11, pp. 1102-1106.

Moore, G., 1965, "Cramming More Components onto Integrated Circuits," *Electronics*, vol. 38, pp. 114-117.

Morgen, M., Ryan, E.T., Zhao, J.-H., Hu, C., Cho, T. and Ho, P.S., 2000, "Low Dielectric Constant Materials for ULSI Interconnects," *Annual Review of Material Science*, vol. 30, pp. 645-680.

Neirynck, J.M., Yang, G.-R., Murarka, S.P. and Gutmann, R.J., 1996, "The Addition of Surfactant to Slurry for Polymer CMP: Effects on Polymer Surface, Removal Rate and Underlying Cu," *Thin Solid Films*, vol. 290, pp. 447-452.

Noh, K., 2005, "Modeling of Dielectric Erosion and Copper Dishing in Copper Chemical-Mechanical Polishing," Ph.D. thesis, Department of Mechanical Engineering, MIT, Cambridge, MA.

Oliver, W.C. and Pharr, G.M., 1992, "An Improved Technique for Determining Hardness and Elastic Modulus Using Load and Displacement Sensing Indentation Experiments," *Journal of Materials Research*, vol. 7, pp. 1564-1583.

Preston, F. W., 1927, "The Theory and Design of Plate Glass Polishing Machines," *Journal of the Society of Glass Technology*, vol. 11, pp. 214-256.

Qin, K., Moudgil, B. and Park, C.-W., 2004, "A Chemical Mechanical Polishing Model Incorporating Both the Chemical and the Mechanical Effects," *Thin Solid Films*, vol. 446, pp. 277-286.

Ring, T.A., Feeney, P., Boldridge, D., Kasthurirangan, J., Li, S. and Dirksen, J.A., 2007, "Brittle and Ductile Fracture Mechanics Analysis of Surface Damage Caused During CMP," *Journal of The Electrochemical Society*, vol. 154, pp. H239-H248.

Runnels, S.R. and Eyman, L.M., 1994, "Tribology Analysis of Chemical-Mechanical Polishing," *Journal of The Electrochemical Society*, vol. 141, pp. 1698-1701.

Singh, R.K. and Bajaj, R., 2002, "Advances in Chemical-Mechanical Planarization," *MRS Bulletin*, vol. 27, pp. 743-751.

Steigerwald, J.M., Murarka, S.P. and Gutmann, R.J., 1997, **Chemical Mechanical Planarization of Microelectronic Materials**, John Wiley & Sons, Inc., New York.

Steigerwald, J.M., Murarka, S.P., Gutmann, R.J. and Duquette, D.J., 1995, "Chemical Processes in the Chemical Mechanical Polishing of Copper," *Materials Chemistry and Physics*, vol. 41, pp. 217-228.

Suh, N.P., 1986, **Tribophysics**, Prentice-Hall, Inc., Englewood Cliffs, NJ.

Teo, T.Y., Goh, W.L., Lim, V.S.K., Leong, L.S., Tse, T.Y and Chan, L., 2004, "Characterization of Scratches Generated by a Multiplaten Copper Chemical-Mechanical Polishing Process," *Journal of Vacuum Science and Technology B: Microelectronics and Nanometer Structures*, vol. 22, pp. 65-69.

Wrschka, P., Hernandez, J., Oehrlein, G.S. and King, J., 2000, "Chemical Mechanical Planarization of Copper Damascene Structures," *Journal of The Electrochemical Society*, vol. 147, pp. 706-712.

Yi, J., 2005, "On the Wafer/Pad Friction of Chemical-Mechanical Planarization (CMP) Processes - Part I: Modeling and Analysis," *IEEE Transactions on Semiconductor Manufacturing*, vol. 18, pp. 359-370.

Zhong, L., Yang, J., Holland, K., Grillaert, J., Devriend, K., Heylen, N and Meuris, M., 1999, "A Static Model for Scratches Generated during Aluminum Chemical-Mechanical Polishing Process: Orbital Technology," *Japanese Journal of Applied Physics*, vol. 38, pp. 1932-1938.